8-2011

EFFECTS OF SURFACE STATES, DEFECTS AND DOPANTS ON THE OPTICAL AND MAGNETIC PROPERTIES OF LOW-DIMENSIONAL MATERIALS

Ramakrishna Podila
Clemson University, rpodila@g.clemson.edu

Recommended Citation

Podila, Ramakrishna, "EFFECTS OF SURFACE STATES, DEFECTS AND DOPANTS ON THE OPTICAL AND MAGNETIC PROPERTIES OF LOW-DIMENSIONAL MATERIALS" (2011). *All Dissertations*. 813.
https://tigerprints.clemson.edu/all_dissertations/813

EFFECTS OF SURFACE STATES, DEFECTS AND DOPANTS ON THE OPTICAL AND MAGNETIC PROPERTIES OF LOW-DIMENSIONAL MATERIALS

A Dissertation
Presented to
the Graduate School of
Clemson University

In Partial Fulfillment
of the Requirements for the Degree
Doctor of Philosophy
Physics

---

by
Ramakrishna Podila
August 2011

Accepted by:
Dr. Apparao M. Rao, Committee Chair
Dr. Malcolm J. Skove
Dr. Shiou-Jyh Hwu
Dr. Jian He

Abstract

Nanomaterials have attracted the attention of researchers from various fields due to their unique features (that are otherwise absent in the bulk) such as quantum confinement, high surface to volume ratio, ability for surface modification etc. Since the discovery of fullerenes and carbon nanotubes, several synthesis techniques have been developed for nanomaterial growth. However, different control parameters in different synthesis techniques often result in nanostructures with varying defects that may alter their fundamental behavior. Such defects or disorder in the crystal lattice can lead to the disruption of lattice symmetry. The defect-induced symmetry lowering (or breaking) effects play a vital role in the determination of fundamental material characteristics. Thus, it is very important to characterize the defects in order to understand their effects on the nanomaterial properties. This thesis describes the role of disorder and defects in low-dimesional systems such as ZnO nanowires, graphene and carbon nanotubes.

Firstly, it describes the synthesis and characterization of ZnO nanostructures and discusses the effects of surface states, defects and dopants on the optical and magnetic properties of ZnO. An unexpected presence of ferromagnetic (FM) ordering in nanostructured nonmagnetic metal oxides has been reported previously. Though this property was attributed to the presence of defects, systematic experimental and theoretical studies to pinpoint its origin and mechanism were lacking. While it is widely believed that oxygen vacancies are responsible for FM ordering, surprisingly annealing as-prepared ZnO samples at low temperature (high temperature) in flowing oxygen actually enhances (diminishes) the FM ordering. For these reasons, we have prepared,

annealed in different environments, and measured the ensuing magnetization in micrometer and nanoscale ZnO with varying crystallinity. We further find from our magnetization measurements and *ab-initio* calculations that a range of magnetic properties in ZnO can result, depending on the sample preparation and annealing conditions. For example, within the same ZnO sample we have observed ferro- to para- and diamagnetic responses depending on the annealing conditions. We also explored the effects of surface states on the magnetic behavior of nanoscale ZnO through non-linear optical spectroscopy and detailed *ab-initio* calculations.

In the case of graphene, we have observed *new* combination modes in the range from 1650 to 2300 cm^{-1} in single-(SLG), bi-, few-layer and incommensurate bilayer graphene (IBLG) on silicon dioxide substrates. A peak at ~1860 cm^{-1} (iTALO^{-}) is observed due to a combination of the in-plane transverse acoustic (iTA) and the longitudinal optical (LO) phonons. The intensity of this peak decreases with increasing number of layers and this peak is absent for bulk graphite. The overtone of the out-of-plane transverse optical (oTO) phonon at ~1750 cm^{-1}, also called the M band, is suppressed for both SLG and IBLG. In addition, two previously unidentified modes at ~2200 and ~1880 cm^{-1} are observed in SLG. The 2220 cm^{-1} (1880 cm^{-1}) mode is tentatively assigned to the combination mode of in-plane transverse optical (iTO) and TA phonons (oTO+LO phonons) around the K point in the graphene Brillouin zone. Finally, the peak frequency of the 1880 (2220) cm^{-1} mode is observed to increase (decrease) linearly with increasing graphene layers.

Finally, we find that the high curvature in sub-nm SWCNTs leads to (i) an unusual S-like dispersion of the G-band frequency due to perturbations caused by the strong electron–phonon coupling, (ii) an activation of diameter-selective intermediate frequency modes that are as intense as the radial breathing modes (RBMs), and (iii) a clear observation of the IR modes.

Dedication

To my family, without whose support, love and encouragement this task would have been impossible.

Acknowledgements

I would like to thank my advisor, Prof. Apparao M. Rao for his endless support and guidance. His confidence and vision have helped me become a better researcher. I have learnt a lot from him and he continues to inspire me to do better in my work. Some of the work done in this thesis would not have been possible without the insights of Dr. Skove and Dr. Jian He. I have learnt several new things during the discussions with them. I would also like to thank Dr. S.-J. Hwu (Clemson University), Dr. Gustavo Dalpian, (UFABC, Brazil) and Dr. Amar Nath (UNC Asheville) for their help with the ZnO project. I also would like to thank Dr. S. J. Stuart for helping me with the molecular dynamic simulations. I am thankful to Dr. Rahul Rao, WPAFB, Ohio for giving me an opportunity to work on the grapheme samples. I have learnt some graphene and nanotube physics during our discussions. It was a pleasure to work with the Parthi group and Dr. Reji Philip’s group for NLO measurements. It brought back several fond memories. I enjoyed my summer stay at Raman Research Institute during summer of 2010.

I thank all my good friends who have accompanied me on the road to a doctoral degree, and whose friendship will be treasured. And finally, thanks to all the present and past Rao group members for their support.

Table of Contents

Page

Table of Contents (Continued)

Page

List of Tables

List of Figures

Figure Page

List of Figures (Continued)

Figure Page

List of Figures (Continued)

Figure Page

List of Figures (Continued)

Figure Page

List of Figures (Continued)

Figure Page

List of Figures (Continued)

Figure Page

List of Figures (Continued)

Figure Page

Chapter 1

Defects in Nanostructured Materials

1. Introduction

Nanomaterials have attracted the attention of researchers from various fields due to their unique features (that are otherwise absent in the bulk) such as quantum confinement, high surface to volume ratio, ability for surface modification etc. Since the discovery of fullerenes and carbon nanotubes, several synthesis techniques have been developed for nanomaterial growth. However, different control parameters in different synthesis techniques often result in nanostructures with varying defects that may alter their fundamental behavior. Such defects or disorder in the crystal lattice can lead to the disruption of lattice symmetry. The defect-induced symmetry lowering (or breaking) effects play a vital role in the determination of fundamental material characteristics. Thus, it is very important to characterize the defects in order to understand their effects on the nanomaterial properties. This chapter briefly describes the defects in low-dimensional materials with specific reference to graphene and ZnO nanostructures.

1.1 Graphene

Graphene is a two-dimensional sheet of sp^2 bonded carbon atoms arranged in a hexagonal lattice (Fig. 1.1.1). Figure 1.1.1 shows two different triangular sub-lattice structures A and B that combine into a honeycomb lattice. Thus, one may understand the honeycomb lattice as a triangular Bravais lattice with a two-atom basis (A and B). The distance between nearest neighbor carbon atoms is $a_{c\text{-}c}$ = 0.142 nm, which is the average of the single (C-C) and double (C=C) bond.

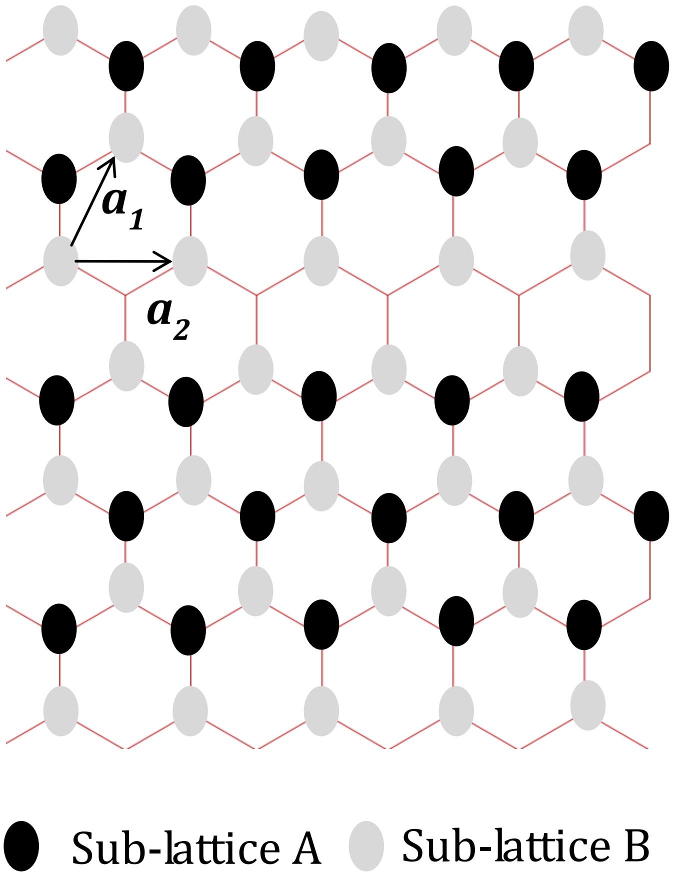

Figure 1.1.1: The graphene honey-comb lattice showing A and B sub-lattices and the graphene lattice vectors.

Fig.1.1.2 shows the first Brillouin zone (BZ; shown in red) for the honey comb lattice. The long wavelength excitations are situated in the vicinity of the Γ point at the center of the BZ. Two *inequivalent* points K and K' are located at the corners of the BZ as shown in the Fig.1.1.2. The four remaining corners (shown in gray in Fig. 1.1.2) may be connected to one of these points (K or K') via a translation by a reciprocal lattice vector.

These crystallographic points play an essential role in the electronic properties of graphene because the low-energy excitations occur near the two points *K* and *K′*.

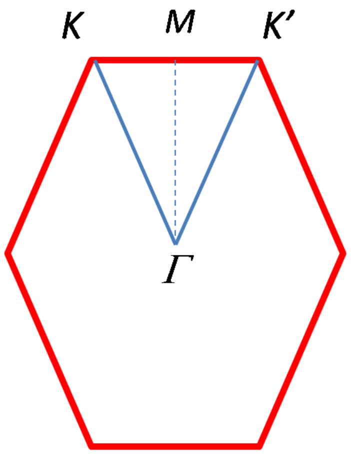

Figure 1.1.2: The first Brillioun Zone of graphene showing various symmetry points.

1.1.1 Stacking Faults

Graphite consists of stacked graphene layers. To illustrate the ordering of graphene layers in crystal graphite, we first consider bilayer graphene (or BLG). The distance between layers is $d \approx 0.34$ nm. The layers are translated with respect to each other, and one may distinguish two different patterns, as shown in Fig.1.1.3. The translation amplitude is given by $\pm\delta_i$. For the choice + δ_i , one obtains a configuration where the *A'* atoms of the upper layer (shown as solid circles) are on top of the *B* atoms of the lower one (open triangles) and for a translation of $-\delta_i$, the *B'* (solid triangles) atoms in the upper layer are on top of *A* atoms (open circles) in the lower one. Notice that any of the two configurations contain four atoms (*A, B, A'*, and *B*') per unit cell.

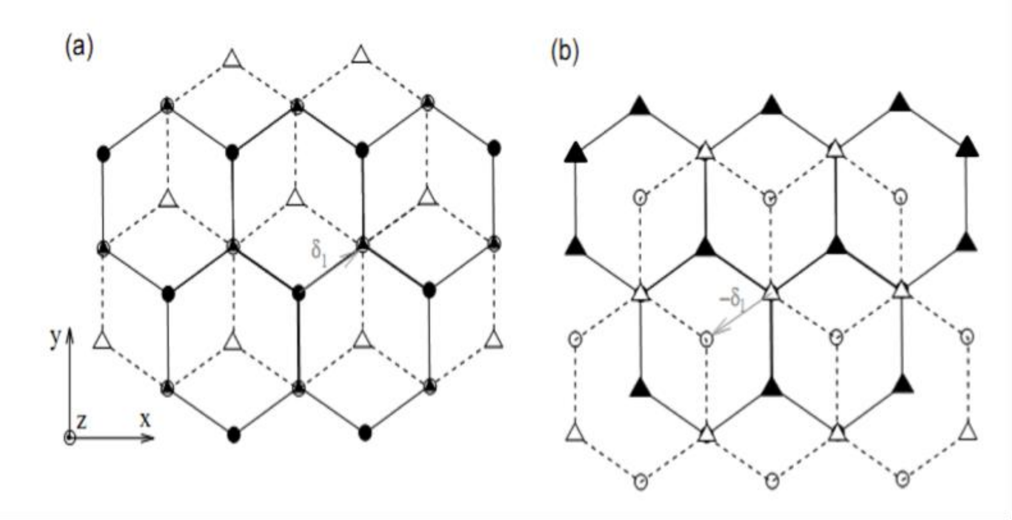

Figure 1.1.3: Stacking in Bilayer graphene.

1.1.2 Bernal, Rhombohedral and Turbostratic Stacking:

Let us consider the situation where the second layer is translated with respect to the first by δ_i. The third layer may then be translated with respect to the second by $\pm\delta_i$. We may categorize graphite into two types depending upon how the third layer is stacked: *a)* if the sign of the translation alternates i.e., $\delta_i, -\delta_i, \delta_i, -\delta_i$, ..., when stacking the graphene layers, we obtain a hexagonal (or AB, Bernal) stacking. Here, there are 4 atoms per unit cell and this is called *α-graphite; b)* if all the layers are translated with respect to their lower neighbor by δ_i then one obtains a rhombohedral stacking (which is also called ***ABC*** stacking) since three layers or 6 atoms per unit cell are necessary to construct the lattice. This form of graphite is called β-graphite,

It is possible to have some randomness in the stacking, *i.e.*, a few *ABC* layers may randomly substitute for *AB* layers in α-graphite. However, crystalline AB stacking occurs most often in natural graphite, with about 30% of ABC-stacking. The presence of such phases was recently found to be useful for characterizing folded graphene (SLG) [1]

In the case of turbostratic graphite, one may distinguish translational disorder from rotational disorder in the stacking. Generally, the graphene layers are relatively weakly bound in turbostratic graphite compared to crystalline graphite. This results in several discernible changes in its electronic and vibrational properties. As an example of rotational disorder, we consider two graphene layers which are rotated by an angle φ that is not a multiple of 30° with respect to each other. Such rotation results in a so-called Moire pattern, with a larger unit cell (see Fig. 1.1.4). The Moire pattern reproduces a (larger) hexagonal lattice.

Rotational and translational stacking faults in graphene constitute the disorder along the *z*-direction. In addition, there are also several other kinds of disorder and defects in the plane of graphene sheet. For example, the finite size of graphene sheet leads to truncation of translational symmetry due to the presence of dangling bonds at the edges. Several researchers have also found ripples and folds that lower the overall symmetry of graphene. Raman spectroscopy has been widely used to characterize the disorder in graphene systems [2, 3]. The following section discusses the use of Raman spectroscopy as a tool for defect characterization in graphene and other carbon nanostructures.

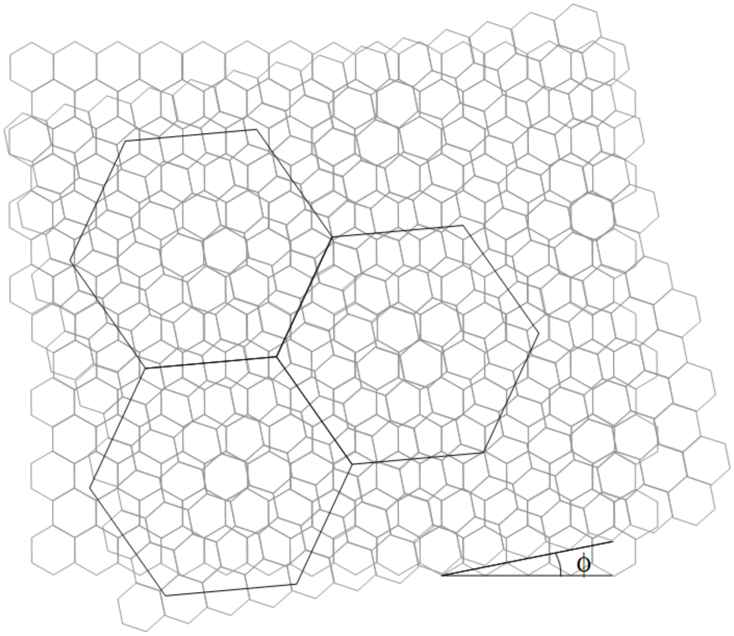

Figure 1.1.4: Moire patterns with larger hexagonal unit cells in turbostratic graphene.

1.2 Raman spectroscopy for defect characterization

As discussed in Fig.1.1.1, single layer graphene (SLG) has two atoms in the unit cell. Therefore it possesses *6* phonon branches: three acoustic and three optical branches (Fig. 1.2.1). One of these optical branches, with out-of-plane tangential optical phonons (oTO), gives rise to an infra-red active mode at the Γ point, while the other branches (iTO and LO) are degenerate at the Γ point ($q=0$) and are Raman active. However, the electronic structure of graphene generates special electron-phonon induced resonance conditions with non-zone center modes ($q \neq= 0$), known in the literature as the double-resonance Raman scattering process [4,5].

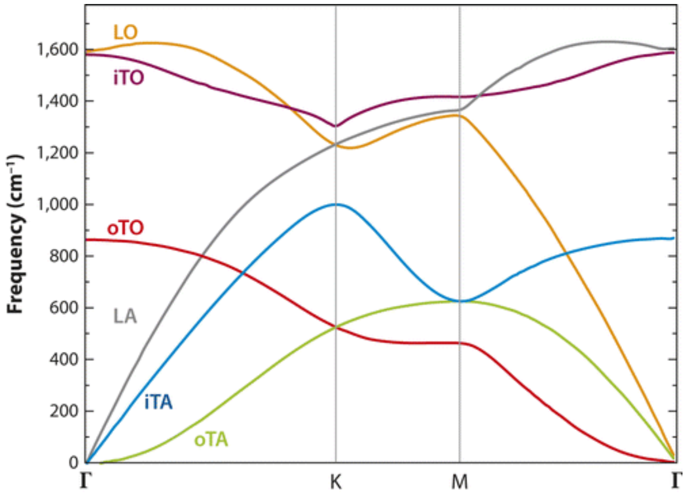

Figure 1.2.1: The phonon dispersion relations for freestanding single layer graphene.

The main features in the Raman spectra of graphene result from the phonon branch related to the zone-center Raman-active mode, i.e. to the optical phonon branch related to in-plane stretching of the C-C bonds. The strongest Raman peaks in crystalline graphene are the well studied *G* (~1584 cm^{-1}) and *G′* (~2400-2800 cm^{-1}) bands. The G-band is the only first-order Raman-allowed mode at the *Γ* point. The G’-band is a second-order Raman-allowed mode near the *K* point and is activated by a double-resonance process. Importantly, the presence of disorder in the crystalline lattice causes changes in the graphene Raman spectra and leads to the appearance of *D* (~1200-1400 cm^{-1}) and *D′* (1600-1630 cm^{-1}) bands. The *D* band comes from the iTO phonon near the *K* point, while the *D′* band comes from the LO phonon near the Γ point due to a double resonance process. The double resonance process can be very easily understood in terms of Feynman diagrams. A simple description of the Feynman diagrams is given below [6,7].

1. Excitations such as photon, phonon, and electron-hole pairs in Raman scattering are represented by the *‘propagators’* shown in Fig.1.2.2. In general, these events are labeled with their corresponding wave vectors, frequencies and polarizations.
2. A vertex (the intersection of any two propagators) represents the interaction between two (or more) excitations. They are usually represented either by solid circles (for electron-photon interaction) or open squares (for electron-phonon interaction).
3. The arrows on the propagators indicate creation and annihilation of corresponding excitations. Arrows pointing away (towards) from a vertex represent creation of quasi-particles (annihilation).
4. The chronological order of the events in a Feynman diagram is from the left to right.
5. Different time orders may be generated by simply permuting the order of vertices in the diagram.

A Feynman diagram can be readily translated into Raman scattering matrix elements (see chapter 2 for a detailed discussion). In Fig.1.2.3, the first vertex introduces a term of the form shown in Eq. 1.2.1 into the scattering probability.

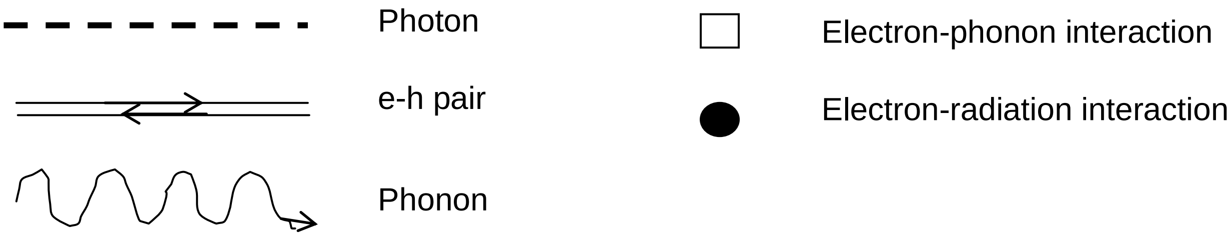

Figure 1.2.2: Symbols used in drawing the Feynman diagrams to represent Raman scattering.

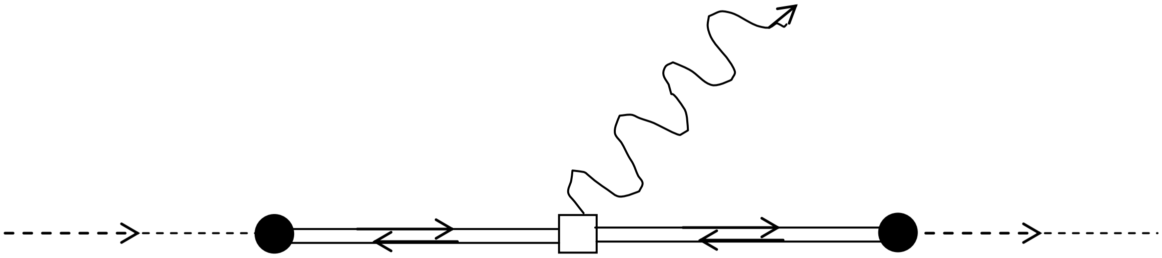

Figure 1.2.3: Feynman diagram for a process that contributes to 1-phonon Raman scattering.

$$\sum_{i} \frac{<n|H|i>}{h\omega-(E_n-E_i)} \tag{1.2.1}$$

In Eq. 1.2.1, |*i*> is taken to be the initial electronic state, H_{er} is the electron-photon interaction, |*n*> denotes any intermediate electronic state with energy E_n. The sign of $h\omega$ in the energy denominator depends upon the arrow described in step 3. Positive sign indicates absorption while the negative sign indicates emission. Since the intermediate state can be any real state, there is a summation over all the available |*n*>. When there is a second vertex, then Eq. 1.2.1 is simply multiplied by a term similar to itself.

$$\sum_{nn'} \frac{< n | H_{el-ph} | n' >< n' | H_{er} | i >}{| h\omega - (E_n - E_i) || h\omega - (E_{n'} - E_i) || h\omega_{ph} - (E_{n'} - E_n) |} \qquad (1.2.2)$$

In Eq. 1.2.2, |*n'*> is another intermediate state. The sign of $h\omega_{ph}$ in the denominator is negative because a quasi-particle (a phonon in this case) is emitted. Each vertex adds a matrix element of the interaction Hamiltonian to the numerator and an energy term to the denominator. The term in Eq. 1.2.2 is the Raman scattering matrix element.

In double resonant Raman scattering, there are two real intermediate electronic states. An appreciation for double resonance Raman is necessary to understand the origin of the D-band and the G'-band in the Raman signature of nano-carbon systems. For this purpose, consider the K point in the BZ of graphene (Figs. 1.1.2 and 1.2.4). The solid line from *a* to *b* in Fig.1.2.4 shows only the resonant contribution involving a phonon that scatters the electron from electronic eigenstate *a* to another eigenstate *b*. Phonon emission conserves quasi-momentum and the change in momentum (*k* values) of electronic eigenstates *a* and *b* is compensated via the phonon momentum (*q*). Similarly, the energy difference between the two eigenstates is again compensated by the phonon.

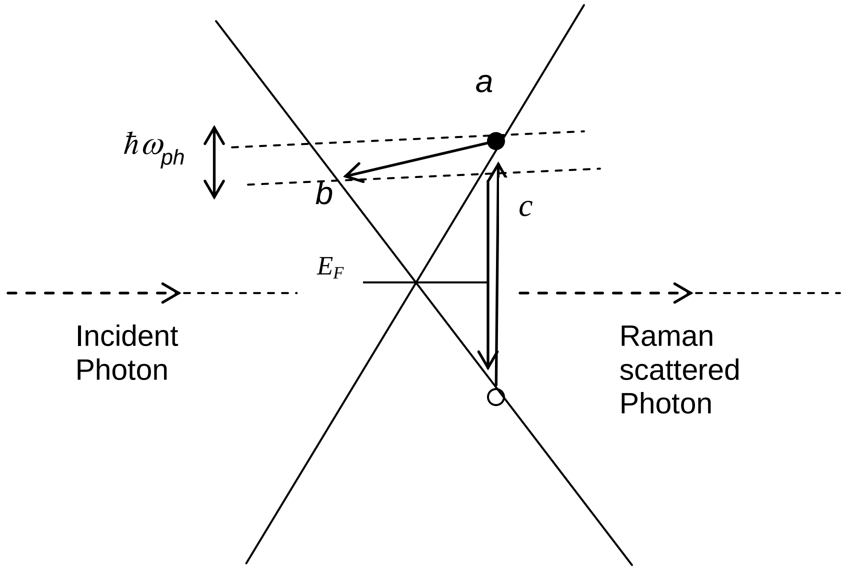

Figure 1.2.4: A schematic for the double resonance process near the K-point

The quasi-linear variation of the electronic energy near the *K*-point results in resonance condition for any of the incoming visible excitation wavelengths. A second resonance transition occurs between *a* and *b* with the emission of a phonon. The third transition from *b* to *c* occurs due to an elastic defect or surface scattering. However, this cannot be resonant as the electronic eigenstate *c* is virtual. Once the electronic eigenstate *c* is reached the electron simply recombines with a hole. The elastic scattering by a defect leads to the Raman active phonon ~ 1380 cm-^{1} (D-band). There is a second possibility for inelastic scattering from eigenstate *b* with another phonon. This leads to a Raman signal at (nearly) twice the phonon energy and does not require a defect to conserve momentum. The Raman matrix elements for these processes may be obtained by drawing the corresponding Feynmann diagrams. Fig. 1.2.5 depicts first and second *time* order process for the D-band.

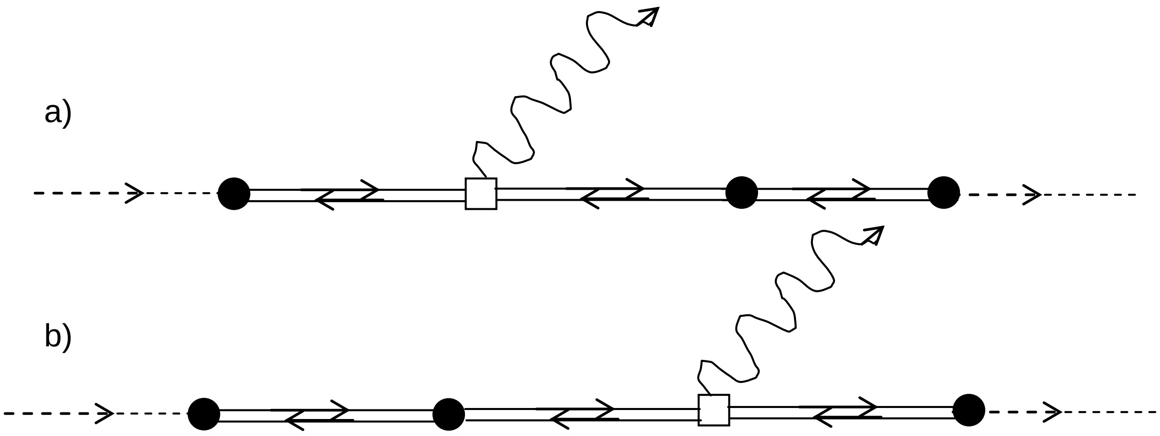

Figure 1.2.5: a) First time order (phonon first, defect second) Feynman diagram, b) Second time order (defect first, phonon second) Feynman diagram.

Thus, the Raman scattering matrix element can be written as

$$\sum_{abc} \frac{M_{eR} M_{e-defect} M_{el-ph} M_{eR}}{(E_1 - E_a - i\gamma)(E_1 - h\omega_{ph} - E_b - i\gamma)(E_1 - h\omega_{ph} - E_c - i\gamma)} \tag{1.2.3}$$

Finally, we use the double resonance picture to understand the experimentally observed dispersion of the phonon frequency with respect to laser energy. A change in the incoming photon energy leads to an excitation with a different momentum. In order to fulfill the second resonant transition, a phonon with different quasi-momentum is required and in particular, a larger incoming photon energy requires a larger phonon wave vector. A larger phonon wave vector will result in shifts in the D-band depending upon the phonon dispersion. Thus, scanning the incident photon energy corresponds to scanning the phonon energy in momentum space.

The ratio of the intensity of the D-band to that of the G-band (denoted as I_D/I_G) has been widely used for the quantification of defects. Many Raman studies in graphite and other carbon systems have been devoted to develop disorder-quantification [8-10]. The most advanced protocols have been developed for the edge-defects in nano-graphite. As shown in Eq. 1.2.4, the in-plane crystallite dimensions (L_a) can be obtained by measuring I_D/I_G [8].

$$L_a\,(\mathrm{nm}) = (2.4 \times 10^{-10}\ \mathrm{nm}^{-3})\lambda^4_{laser}\,(nm^4)\,(I_D/I_G)^{-1}. \qquad (1.2.4)$$

It has also been shown that the D band intensity depends on the atomic structure of graphene at the edges. It was found to be absent in graphite edges when the atomic structure exhibits the zigzag arrangement [11]. On the contrary, the armchair edges lead to a strong D-band. A perfect zigzag edge structure would be evidenced by the observation of a D' band (~1620 cm^{-1}) in the Raman spectra with a complete absence of the D band [11].

In summary, carbon nanostructures can exhibit in-plane defects and rotational stacking faults. These defects can be observed experimentally in the Raman spectrum due to a double resonance process. Further, the ratio of I_D/I_G can be used to effectively determine the average crystallite size in carbon systems.

1.3 Defects in ZnO

ZnO naturally crystallizes in the hexagonal wurtzite-type structure shown in Fig.1.3.1. It has a polar hexagonal axis, the *c-axis*, chosen to be parallel to *z*. The primitive translation vectors ***a*** and ***b*** are in the *x–y* plane. One Zn^{2+} ion is tetrahedrally surrounded by four O^{2-} ions and vice versa. The primitive unit cell contains two units of ZnO (or 4 atoms per unit cell) in total. Thus, ZnO has 12 phonon branches. 9 of these 12 branches are optical while 3 are acoustic. ZnO wurtzite structure belongs to the C_{6v} point group. It is a direct gap semiconductor (band gap ~ 3.37 eV at 300 K) with the upmost valence and the lowest conduction bands (VB and CB, respectively) at the Γ-point. The lowest CB is formed by the empty 4s states of Zn^{2+} or the anti-bonding sp^3 hybrid states while the O^{2-} *p*-orbitals form the VB.

The defects in the ZnO crystal lattice can be of several kinds such as O/Zn vacancies, O/Zn/H_2 interstitials or O/Zn anti-sites. The defects in ZnO nanostructures vary depending upon the synthesis method.

The following discussion briefly describes some of the common defects in ZnO, which profoundly alter their magnetic and optical properties. Fig.1.3.2 shows the energy diagram depicting defect energies in ZnO nanostructures.

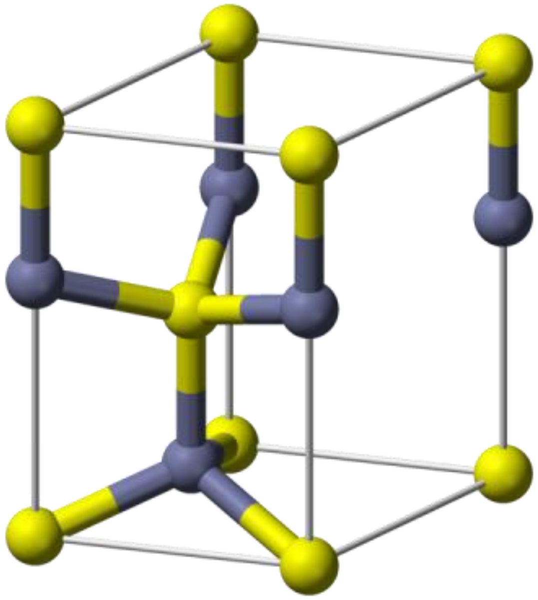

Figure 1.3.1 : Unit cell for wurtzite-type ZnO

1.3.1 O-Vacancies:

Defects such as O-vacancies (V_o) have low formation energy in *p*-type ZnO nanostructures. V_o is a deep donor, while Zn interstitials (Zn_i) are unstable at room temperature. Zn vacancies (V_{Zn}) are present as compensating acceptors in *n*-type ZnO. Other native defects, such as Zn antisites, O antisites, and O interstitials, have high formation energies. Experimentally, they have not been observed in appreciable concentrations.

The green luminescence band centered around 2.4 eV (~510 nm) in the photoluminescence (PL) spectra of ZnO nanostructures has been attributed to O vacancies due to an excited-to-ground state transition [12,13]. Annealing in O_2 (Zn) vapor results in PL lines at 2.35 (2.53) eV while annealing in ZnO powder removes both these lines. Such observations suggested that the 2.35 eV emission is due to V_{Zn} and the 2.53 eV emission is due to V_O [14]. It is important to note that numerous defects have been linked to the green luminescence [15]. Electron irradiation, which produces V_O and other defects, leads to a *reduction* in green luminescence and an increase in PL bands near 600 and 700 nm [16,17]. Thus, it cannot be generalized that V_O cause green luminescence

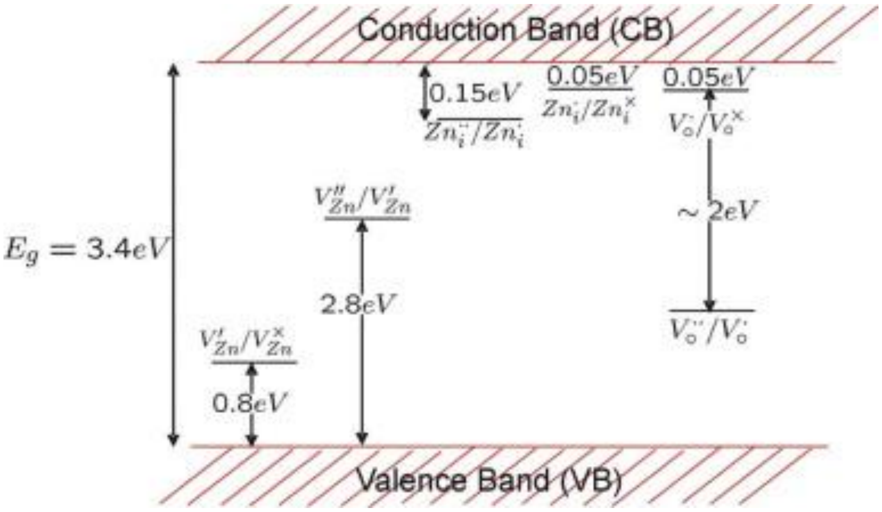

Figure 1.3.2: A schematic for defect energy levels in wurtzite-type ZnO nanostructures.

1.3.2 Zn vacancies

V_{Zn} are double acceptors. First-principles calculations find their acceptor levels to be ~0.1-1.2 eV above the maximum of VB. Under illumination at low temperatures, V_{Zn} vacancies can be transformed to the 1^- or neutral charge state, both of which are EPR active. In the 1^- charge state, the defect has a spin $S = ½$, while in the neutral charge state, two holes are trapped on different non-axial (non- parallel) O sites, resulting in a spin $S = 1$. From the wavelength of light required to pump Zn vacancies from the 1^{-} to the neutral charge state, Evans *et al.* [18] estimated that the ground state for the 1^{-} charge state lies ~0.9 eV above the valence band. V_{Zn} energy levels situated ~ 0.9-1.2 eV above VB have an absorption ~2.1-2.4 eV and may also account for the green luminescence in some ZnO nanostructured samples.

1.3.3 H-Interstitials:

Fig.1.3.3 shows two possible configurations for interstitial H donors. In the first configuaration, H is in the *antibonding* ($AB_{\perp}$) orientation, attached to a host O atom and pointing away from the Zn–O bond. Another model is the *bond-centered* ($BC_{\parallel}$) configuration, where H is located between Zn and O atoms. By measuring the pressure and polarization dependence of the O–H vibrational modes, Jokela and McCluskey [19] attributed an IR peak at 3326 cm^{-1} (at 10 K) to H donors in the $AB_{\perp}$ configuration. It was also observed that these IR peaks ~3326 and 3611 cm^{-1} are unstable and decay at room temperature over several weeks [19]. They form a species of *“hidden hydrogen”* that remains in the crystal. Shi *et al.* [20] proposed that the H donors combine to form H_2 molecules, which are electrically neutral and nearly invisible to IR.

When the crystal is reheated, the H_2 molecules dissociate and form H donors again. Experimental verification for H_2 molecules in ZnO was achieved using low-temperature Raman spectroscopy [21].

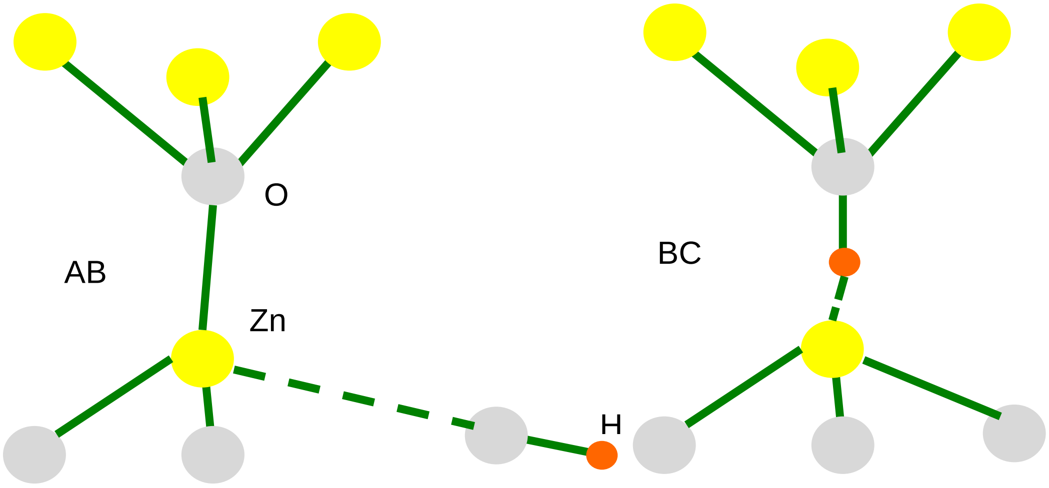

Figure 1.3.3: Anti-bonding (left panel) and bond centered (right panel) H-interstitial in ZnO

In this dissertation, we will discuss the role of defects in determination determining of the optical and magnetic properties of ZnO nanostructures. An unexpected presence of ferromagnetic (FM) ordering in nanostructured nonmagnetic metal oxides has been reported by many researchers. It was widely believed that oxygen vacancies are responsible for FM ordering. As it will be discussed in chapter 3, we find that annealing as-prepared ZnO nanostructured samples at low temperature (high temperature) in flowing oxygen enhances (diminishes) the FM ordering. For these reasons, we prepared, annealed in different environments, and measured the ensuing magnetization in micrometer and nanoscale ZnO with varying crystallinity. We further find from our magnetization measurements and *ab-initio* calculations that a range of magnetic properties in ZnO can result, depending on the sample preparation and annealing conditions. For example, within the same ZnO sample we have observed ferro- to para- and diamagnetic responses depending on the annealing conditions. We will also discuss the effects of surface states on the magnetic behavior of nanoscale ZnO through detailed calculations and non-linear optical studies (NLO) in chapter 3.

A brief overview of the rest of this dissertation is as follows. Chapter 2 outlines the quantum mechanical description of the Raman effect and the Z-scan method used for measuring NLO properties. Chapter 3 describes the synthesis and characterization of ZnO nanostructures and discusses the effects of surface states, defects and dopants on their optical and magnetic properties. Chapter 4 elucidates on the effects of curvature and defect induced symmetry lowering on the optical, and vibrational properties of sub-nanometer single-wall carbon nanotubes and graphene. Finally, at the end of this dissertation, a glossary of abbreviated terms used throughout the manuscript has been compiled in the appendix.

Chapter 2

Characterization Techniques

2.1 Introduction – Raman Spectroscopy

Raman spectroscopy has been widely used in physics for investigating the vibrational structure of materials. In 1928, Sir C.V. Raman made the first experimental observation of inelastic scattering process under very crude conditions. The development of lasers in the 1960's helped Raman spectroscopy to flourish and become a mainstream technique for measuring the vibrational structure in materials apart from infra-red spectroscopy. Raman spectroscopy has evolved into an indispensable technique in science today and has become an excellent complementary tool to IR spectroscopy for investigating the vibrational structure of materials as well as aiding in the identification of the crystal structure of materials. Raman spectroscopy has also been used to investigate temperature, magnetically/electrically induced, and many other changes in materials. A simple description of the Raman scattering process involves three basic steps: i) a photon is absorbed by an electron exciting it to a higher energy state, ii) this excited electron undergoes an inelastic scattering event with a lattice vibration, or phonon, resulting in an increase or decrease in the electron's energy and iii) the electron relaxes back to a lower energy state by emission of a photon whose energy is different fthan that of the incoming photon. However, the probability for Raman scattering is considerably than for Rayleigh scattering. Thus, the intensities of the Raman peaks are considerably weaker than the Rayleigh scattered light. It is important to mention that the

Raman intensity can vary depending on resonance conditions, but is usually on the order of several magnitudes (factors of 100-1000) lower than the Rayleigh scattered light.

2.2 Classical Derivation of Raman Spectroscopy

The classical derivation of Raman spectroscopy is based on the bond polarizability model. Figure 2.2.1 shows a simple schematic of the 3 steps of the process described above. The Raman scattered light may be higher (or lower) in energy depending upon the emission (or absorption) of a phonon. The emission (absorption) spectra are known as the ‘stokes’ (anti-stokes). Since the probability for the availability of a particular phonon for absorption is considerably lower than the probability for emission, the stokes spectra are often stronger.

In Figure 2.2.1, ω is the frequency of the incoming photon and ω' is the frequency of the scattered photon. The labels ν refer to the vibrational energy bands in the material. It should be noted that the vibrational energy levels are much smaller that the electronic energy levels. The center peak (often referred to as the laser line) is the elastically scattered, or Rayleigh scattered peak. In this process, the photon is absorbed and excites the electron to an excited state. The electron then emits a photon of the same wavelength and returns to its initial electronic and vibrational state. This is the most common process in a light scattering process and results in a very intense peak in the spectrum.

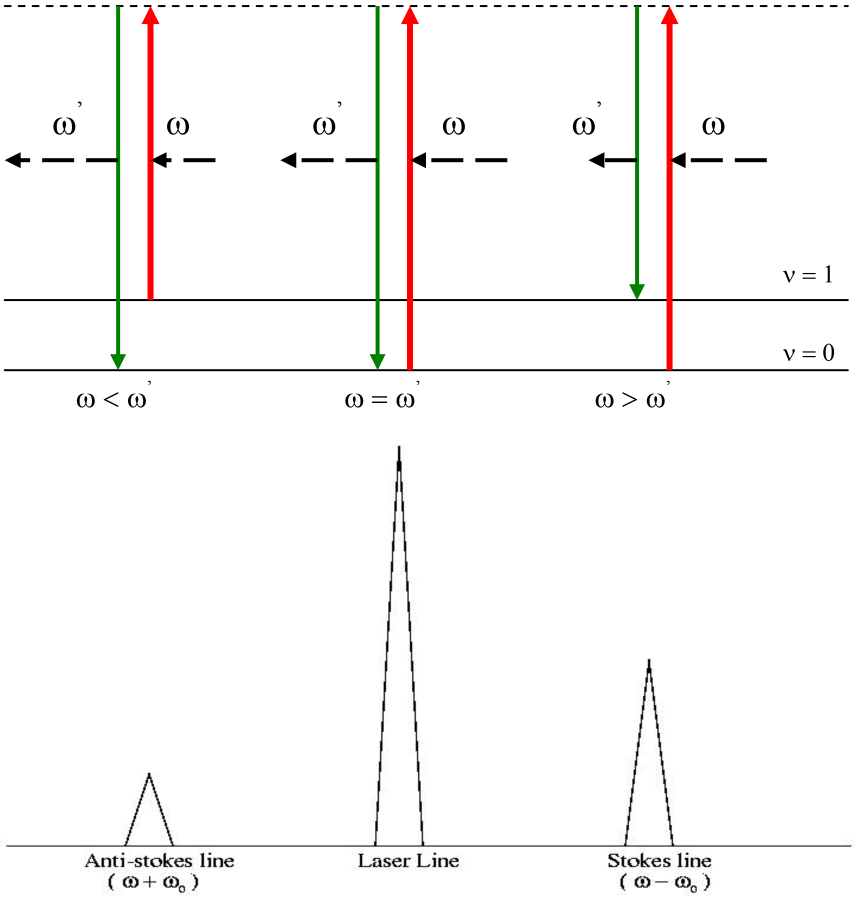

Figure 2.2.1: The top panel in this figure illustrates the three scattering processes with the lower illustrating the respective intensity in each process.

The Raman instruments are equipped with either a notch filter or a grating system to block this peak and help in resolving the Raman scattered light. There are two other peaks that are related that can also occur in the spectrum. These two peaks are the result of Raman scattered photons and only make up, on average, about 0.1% of the scattered photons. As described above, the peak on the far right is called the Stokes peak. This peak is one of the two Raman scattering peaks seen and comes about from the excited electron scattering in the lattice and giving up some of its energy to the creation of a phonon. The emitted light from the electron now is downshifted in energy, which results in a peak appearing at a lower ω. The other peak is called the anti-stokes peak. This process requires that the initial state of the electron (in a given molecule) be in one of the excited vibrational states of the molecule ($\nu = 1$ for example). These initial excited states usually come about from thermal excitations. Once the electron absorbs the incoming photon it emits a photon of higher frequency and returns to the ground state, a lower energy state than the initial state. This results in a peak seen in the spectrum with a higher frequency. In all of these cases, if the excited state of the electron after absorbing the incoming photon is not a real (stable) state in the material it is referred to as a virtual state. This will be explained in greater detail in the next section.

2.2.1 The bond polarizability model:

Bond polarizability is the degree that an electric field affects the bond in a molecule or crystal structure. For simplicity, consider a diatomic molecule. In the absence of an electric field ($\boldsymbol{E}$) the two centers of charge distributions (for two atoms) overlap and result in no net dipole moment. However, in the presence of the electric field, the electrons are shifted in one direction, while the positively charge nuclei are shifted in the opposite direction. This results in a small displacement x in the “center of negative charge” and the “center of positive charge”. In general, the induced dipole moment is related to the electric field by the power series

$$\vec{m} = a\vec{E} + \frac{1}{2}b\vec{E}\vec{E} + \frac{1}{6}g\vec{E}\vec{E}\vec{E} + \ldots \tag{2.2.1}$$

In the above equation, α, β and γ are tensors indicating that the direction of induced dipole moment is not necessarily same as the direction of the applied electric field. In the classical picture, the tensors are considered to be real. The magnitude of δ, γ, etc., are at least 10^{10} smaller than α and can be neglected for this discussion. In such a picture, μ becomes the product of the electric field vector with the polarizability tensor given by equation (2.2.2).

$$\vec{\mu} = \alpha\vec{E} \tag{2.2.2}$$

In the case of Raman scattering the electric field comes from the incoming light source and can be given by Eq. (2.2.3).

$$\vec{E} = E_0 \cos(\omega t)\hat{z} \tag{2.2.3}$$

Substituting Eq. (2.2.3) into Eq. (2.2.2) results in a dipole that oscillates at the same frequency as the incident light as seen in equation (2.2.4).

$$\vec{\mu} = \alpha E_0 \cos(\omega t)\hat{z} \tag{2.2.4}$$

Next, with the molecule or crystal viewed as atoms that are connected by springs we can express the generalized vibrational coordinates as:

$$Q_m = Q_0^m \cos(\omega_m t) \tag{2.2.5}$$

Expanding the polarizability in a Taylor series gives:

$$\alpha = \alpha_0 + \left(\frac{d\alpha}{dQ_m}\right) Q_m + \ldots \tag{2.2.6}$$

Combining Eqs. (2.2.5) and (2.2.6) gives:

$$\alpha = \alpha_0 + \left(\frac{d\alpha}{dQ_m}\right) Q_0^m \cos(\omega_m t) \tag{2.2.7}$$

Again, substituting this expression into Eq. (2.2.4) will give:

$$\vec{\mu} = \alpha_0 E_0 \cos(\omega t)\hat{z} + \left(\frac{d\alpha}{dQ_m}\right) E_0 Q_0^m \cos(\omega_m t)\cos(\omega t)\hat{z} \tag{2.2.8}$$

And finally through a simple trigonometry identity we get:

$$\vec{\mu} = \alpha_0 E_0 \cos(\omega t)\hat{z} + 0.5\left(\frac{d\alpha}{dQ_m}\right) E_0 Q_0^m \left[\cos(\omega t - \omega_m t) + \cos(\omega t + \omega_m t)\right]\hat{z} \tag{2.2.9}$$

Eq. (2.2.9) is the defining equation that gives rise to Raman scattering. It is known that a dipole will emit radiation at the same frequencies that it oscillates. In Eq. (2.2.9) it is clear that the first term will give rise to Rayleigh (elastically) scattered light. The second term is where the Raman scattered light originates. This term contains two parts: Stokes and anti-Stokes peaks in the Raman spectrum respectively. Another interesting feature that can be drawn from this equation is the intensity of the Stokes and anti-Stokes peaks. The intensities for each of these peaks are dependent on the square of the change in the bond polarizability with respect to the m^{th} vibrational coordinate. Therefore, if the polarizability changes little with respect to a particular vibration, then the intensity of the Raman peak will be very small or possibly not observable. Thus, even though a particular mode is allowed it is not necessarily observed in the Raman spectrum. The classical picture is incomplete in several aspects. It does not describe the selection rule process. The observed Raman phenomenon demands a quantum mechanical explanation.

The polarizability tensor a can be geometrically interpreted as an ellipsoid. The quantity $\boldsymbol{r.\alpha.r}$ is an ellipsoid equation ($\boldsymbol{r}$ is the position vector). As seen from equation (2.2.9), the Raman spectra is seen only when the change in polarizability is not zero. In terms of the polarizability ellipsoid, Raman modes can be observed only when the size and shape of the polarizability ellipsoid change.

2.2.2 Overtones and combinations:

The classical picture described in the above section exclusively explains the fundamental or first-order Raman modes. If mechanical anharmonicity is taken into account, the time dependence of the normal co-ordinate Q_k will also include terms such as $cos(i\omega_k t+\delta_{ik})$ *(n=1,2,3…)*. As a consequence, there will be additional induced dipoles with frequencies such as $\omega_0 \pm n\omega_k$.

2.3 Quantum mechanical derivation of Raman Scattering

In the quantum picture, an electron is excited by the incoming photon (from the laser) and is followed by a hole recombination and emission of a photon with different energy. Since energy and momentum are conserved, the generation of a quasi-particle (phonon) is required. The quantum mechanical derivation uses time-dependent perturbation theory in the Schrodinger picture. In Schrodinger picture, a state change from time t_0 to time t can be written as:

$$|\, j, t_0; t\rangle = \sum\nolimits_n c_n\left(t\right)|n\rangle \qquad (2.3.1)$$

The time-dependent coefficients c_n(t) can be expanded as $c_n\left(t\right) = c_n^{(0)} + c_n^{(1)} + c_n^{(2)} + \ldots$

The result of this leads to

$$c_n^{(0)} = \delta_{ni}$$

$$c_n^{(1)} = \frac{-i}{\hbar}\int_{t_0}^{t} e^{i\omega_{ni}t'} H'_{ni}\left(t'\right)dt^{t} \qquad (2.3.2)$$

$$c_n^{(2)} = \left(\frac{-i}{\hbar}\right)^2 \sum\nolimits_m \int_{t_0}^{t} dt' \int_{t_0}^{t'} dt'' e^{i\omega_{nm}t'} H'_{nm}\left(t'\right) e^{i\omega_{mi}t''} H'_{mi}\left(t''\right) .$$

where H'_{nm} and H'_{mi} are equal to $\langle n|H'|m\rangle$ and $\langle m|H'\,|\,j\rangle$, respectively, and H' is the Hamiltonian due to the perturbation. The interaction of light with matter results in a perturbation Hamiltonian that can be expressed as

$$H' = -\,\vec{m}\times\vec{E} \ . \qquad (2.3.3)$$

Evaluation of the second order term, $c_n^{(2)}$, along with the perturbation in Eq. (2.3.3) yields the Kramers-Heisenberg-Dirac (KHD) equation (Eq. 2.3.4).

$$\left(\alpha_{\rho\sigma}\right)_{jf} = \frac{1}{\hbar}\sum_m \left[\frac{\langle j|\mu_\rho|m\rangle\langle m|\mu_\sigma\,|\,f\,\rangle}{\omega-\omega_{mi}} + \frac{\langle j|\mu_\rho|m\rangle\langle m|\mu_\sigma\,|\,f\,\rangle}{\omega+\omega_{mf}}\right] \qquad (2.3.4)$$

This equation forms the basis of Raman scattering in quantum mechanics. The numerators contain what are referred to as transition moments and have the form $\langle a|\mu|b\rangle$. However, further evaluation of this Eq. (2.3.4) is necessary to more clearly understand the Raman process within it. In Eq. (2.3.4) when the denominator in the first term approaches zero, the Raman process is said to be resonant. Further, one can introduce electron-phonon interactions by a perturbation expansion of the $|m\rangle$ state with respect to an electron-phonon perturbation Hamiltonian, H_{ep}, which reflects the electron-phonon scattering events due to thermal excitations. Thus, $\left|m\right\rangle$ can be written as

$$\left|m\right\rangle = \left|\phi_m\right\rangle + \sum_{m'} \frac{\left|\phi_{m'}\right\rangle\left\langle\phi_{m'}\right|H_{ep}\left|\phi_m\right\rangle}{E_{0m} - E_{0m'}} + \ldots \; . \tag{2.3.5}$$

Inserting Eq. (2.3.5) into Eq. (2.3.4) results in

$$\begin{aligned}
\left(\alpha_{\rho\sigma}\right)_{jf} \propto & \sum_{m} \left\langle f\right|\mu_\rho\left|\varphi_m\right\rangle\left\langle\varphi_m\right|\mu_\sigma\left|j\right\rangle + \sum_{m}\sum_{m'} \left\langle f\right|\mu_\rho\left|\varphi_m\right\rangle\left\langle m\right|H_{ep}\left|\varphi_{m'}\right\rangle\left\langle\varphi_{m'}\right|\mu_\sigma\left|j\right\rangle \\
& + \sum_{m}\sum_{m''} \left\langle f\right|\mu_\rho\left|\varphi_{m''}\right\rangle\left\langle\varphi_{m''}\right|H_{ep}\left|m\right\rangle\left\langle\varphi_m\right|\mu_\sigma\left|j\right\rangle \\
& + \sum_{m}\sum_{m'}\sum_{m''} \left\langle f\right|\mu_\rho\left|\varphi_{m'}\right\rangle\left\langle\varphi_{m'}\right|H_{ep}\left|m\right\rangle\left\langle m\right|H_{ep}\left|\varphi_{m''}\right\rangle\left\langle\varphi_{m''}\right|\mu_\sigma\left|j\right\rangle
\end{aligned} \tag{2.3.6}$$

Eq. (2.3.6) is shown here without the energy terms in the denominator to preserve some clarity. The first term of this equation results in no phonon scattering event. The electron is simply excited to a higher state and emits a photon and returns to a lower state without any electron-phonon interaction. The second and third terms in this equation give rise to Raman scattering. In both terms, the electron is raised to a higher energy state where it undergoes a single phonon scattering event before returning to a lower energy state by emission of a photon. The fourth and final term is a double phonon scattering process. After the electron is excited it undergoes two successive phonon scattering events before photon emission. As mentioned earlier, the denominator for these terms can also approach zero (see Eq. 2.3.4) and lead to a double resonance condition.

Another important feature in the quantum mechanical derivation of the Raman process is the introduction of selection rules. These selection rules come about from the electric dipole approximation. This approximation works on the basis that the wavelength of the light is much larger than the atomic dimensions in the material. This approximation begins with rewriting the perturbation Hamiltonian of the incident light as

$$H^{'} = -\frac{e}{m_e c}\vec{A}\cdot\vec{p} \tag{2.3.7}$$

where $\vec{A}$ can be expressed as

$$\vec{A} = A_0\hat{\varepsilon}\left[e^{i\left(\frac{\omega}{c}\right)\hat{n}\cdot\vec{x} - i\omega t} + e^{-i\left(\frac{\omega}{c}\right)\hat{n}\cdot\vec{x} + i\omega t} \right] \tag{2.3.8}$$

with $\hat{\varepsilon}$ and $\hat{n}$ being the polarization and propagation direction, respectively. An expansion of $e^{i\left(\frac{\omega}{c}\right)\hat{n}\cdot\vec{x}}$ can be done to give

$$e^{\left(\frac{\omega}{c}\right)\hat{n}\cdot\vec{x}} = 1 + i\frac{\omega}{c}\hat{n}\cdot\vec{x} + \dots \tag{2.3.9}$$

In the limit that the wavelength of the light is much larger than the atomic dimensions, $\frac{\omega}{c}\hat{n}\cdot\vec{x} << 1$, Eq. (2.3.9) can be evaluated by its leading term. Thus, the spatial dependence of the incident light has been eliminated, which simplifies things considerably. Now the perturbation Hamiltonian can be expressed as

$$H^{'} = -\frac{e}{m_e c} A_0 \hat{\varepsilon}\left[e^{i\omega t} + e^{-i\omega t}\right]\cdot \vec{p} \tag{2.3.10}$$

Now, when evaluating H_{nm} and H_{mi} from Eq. (2.3.2), terms of the form $\langle n|\vec{p}|m\rangle$ come about. Finally, these terms reduce to

$$\langle n|\vec{p}|m\rangle = im\omega_{nm}\langle n|\vec{x}|m\rangle \ . \tag{2.3.11}$$

This new form very strongly resembles the form of a simple dipole moment in a diatomic molecule and is actually a different way of writing the transition moments. At this point the selection rules can be seen in the Raman process. Since we can look at the atoms in the lattice as being connected to each other by springs, we can view the system as many harmonic oscillators that are coupled to one another. With this in mind, the operator, $\vec{x}$, in Eq. (2.3.11) will change the vibrational quantum number by ± 1. This is the selection rule in Raman scattering. Each transition involving the absorption or emission of a phonon will change the magnitude of the vibrational quantum number by one.

While the classical derivation of the Raman effect is a very straightforward approach that yields important information about the process, the quantum mechanical derivation gives even more information about it. Both of these approaches can be used to analyze Raman spectra to draw out important properties when investigating a material. Only a basic introduction to Raman scattering has been presented here, there still remains much more about Raman scattering that has not been given that can help aid in the identification of specific properties in material.

2.4 Non-linear optical spectroscopy and the Z-scan method.

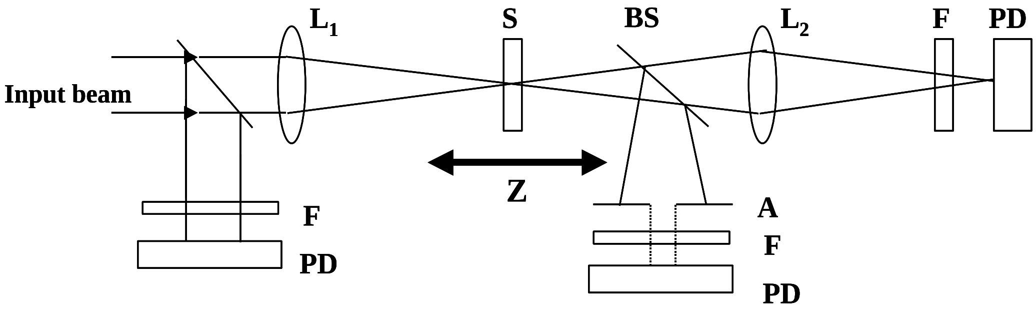

L_1, L_2 - Lenses S - Sample BS - 50-50 beam splitter
F - Neutral density filter A - Aperture PD - Photodiode

Figure 2.4.1: A conventional Z-scan layout for simultaneous open aperture and closed aperture measurement.

The Z-scan technique is a sensitive and simple method employed to measure nonlinear absorption and nonlinear refraction. It has been used extensively to study the optical nonlinearity of various materials like semiconductors, nanocrystals, semiconductor-doped glasses, liquid crystals, organic materials, and biomaterials. Introduced by Sheik Bahae et al. [23] in the early nineties, this widely used technique, which is based on the Kerr lensing effect, has many advantages over other nonlinear spectroscopic methods. In a typical Z-scan, the light induced change in transmittance (ΔT) of a medium due to optical nonlinearity is measured as a function of input light energy density (fluence) or intensity. A continuous variation of the input fluence is achieved by translating the sample under study through the focal region of a focused laser beam (the sample position is taken as z with z = 0 being the focal point for the incident laser beam; hence the name "*Z*-scan"). The consequent fluctuations of the intensity incident at the sample position lead to wavefront distortions (created by nonlinear optical effects in the sample). There are two types of Z-scan techniques, namely, the 'closed aperture' Z-scan and the 'open aperture' Z-scan.

In the closed aperture Z-scan, which is used for studying nonlinear refraction (NLR), the transmitted beam is passed through an aperture placed in the far field, and then measured by a detector, for different values of sample position z. When the medium is far in front of the focal plane no self-lensing occurs. As the medium approaches the focal plane, the high intensity begins to induce a lensing effect in the medium. For a negative nonlinearity this lens tends to collimate the beam, thereby increasing the transmittance through the aperture. At the focal plane, even though the intensity is highest, the influence of the induced lens is minimized, resulting in a transmittance comparable to the linear transmittance. This is similar to placing a thin lens at the focus of a beam; this results in a minimal effect on the far field beam pattern. As the sample is translated beyond the focal plane, the negative lens tends to increase the beam divergence, resulting in a decrease in the aperture transmittance. As the medium is translated still farther from focus, the intensity again becomes weak enough that the induced lensing is negligible. This sequence results in a change in transmittance with a characteristic peak followed by a valley, giving a curve which is symmetric about the focus ($z=0$). For a positive nonlinearity the pattern consists of a valley followed by a peak. Thus, a simple Z-scan experiment can give both the sign and magnitude of the optical nonlinearity in a material. In both these cases, a purely refractive nonlinearity is considered, assuming that no absorptive nonlinearities are present. The sensitivity to nonlinear refraction results from the vital role played by aperture **A** (Fig. 2.4.1). If aperture A is removed then the *Z*-scan is sensitive only to nonlinear absorption (NLA), and this configuration is commonly referred to as the open aperture Z-scan. The absorptive nonlinearity will be a maximum at the focal plane, where the intensity is highest. Thus, the open aperture scheme is employed to characterize materials that exhibit NLA, such as excited state absorption (ESA), two (multi) photon absorption (2PA/MPA), saturable absorption (SA), etc.

Even though closed aperture Z-scan is used to study only NLR, in practice the closed aperture Z-scan curve may contain a contribution from NLA also, depending on the sample. To obtain the NLR coefficient in such a case, it is sufficient to normalize the closed aperture data using the open aperture data before analysis. Although the open aperture Z-scan technique is adequate to detect the presence of nonlinear absorptive effects, it cannot singularly identify the nature of absorptive nonlinearity. For example, at the outset it cannot differentiate a 2PA signature from a two-step excitation signature. Fig.2.4.2 shows typical Z-scan curves simulated for the MPA, SA and RSA processes. The Z-scan curves for SA (peak) and RSA (valley) have shapes which are complementary to each other. It should be noted that the Z-scan curves for RSA and MPA look very similar to each other. To confirm the exact nature of the process, it is often necessary to know the linear absorption properties of the sample from a linear absorption spectrum taken using a spectrophotometer. Z-scans performed using ultrafast laser pulses will also be instructive in this regard.

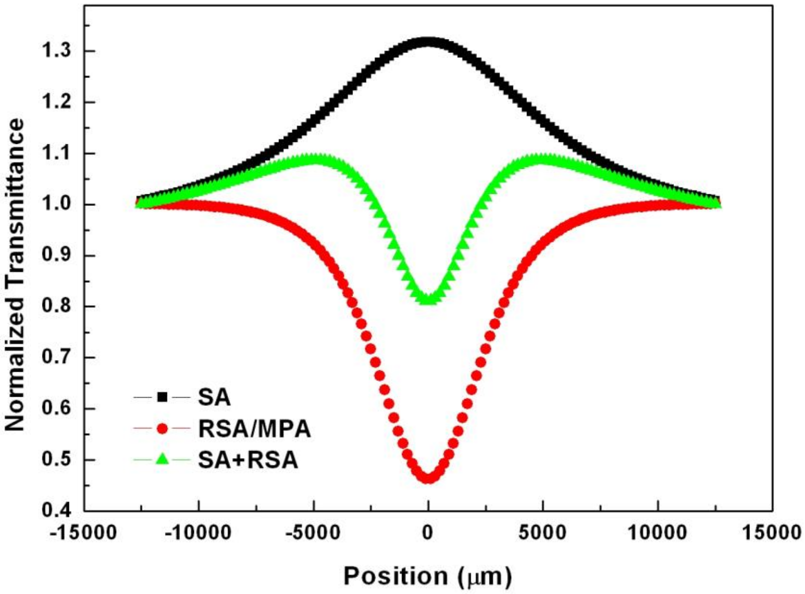

Figure 2.4.2: Simulated Z-can curves for the saturable absorption (SA), reverse saturable absorption (RSA) and multi-photon absorption (MPA) processes.

A recent variation in the z-scan technique is the white light continuum z-scan, where a supercontinuum is used as the light source for doing the z-scan experiment. The "supercontinuum" is an intense, ultrafast, broadband light pulse, wavelengths spanning from the UV to the near IR region, generated when an ultrafast laser pulse is passed through certain transparent NLO media like heavy water. Conversion of the spectrally narrow pump pulse into the resultant broad spectrum involves the interplay of self-phase modulation and self focusing of the pulse, due to an intensity-dependent refractive index of the medium. Since the typical supercontinuum spectrum covers the whole visible range it appears white, and hence it is also known as a "white-light continuum". In the conventional z-scan technique the nonlinearity can be measured only for one wavelength in one measurement. To determine the spectral dispersion of the nonlinearity a tunable laser source has to be used, and separate z-scans need to be done at all the required wavelengths. Obviously this approach is time consuming and tedious. The idea of using a strong white light continuum (WLC) as the light source to measure the dispersion of the nonlinearity in a single z-scan experiment was therefore proposed by Van Stryland's group [24]. Their "WLC Z-scan" allows for rapid, broadband characterization of degenerate NLA and NLR, and the first measurement was in bulk semiconducting materials.

Chapter 3

Role of Defects and Dopants in Magnetic and Optical Properties of ZnO Nanostructures

3.1 Introduction

The control of defects is very important in applications that exploit the unique properties of nanostructures. It is well known that the surfaces of nanostructured materials contain segregated impurities, adsorbed gases that may act as sources and sinks of electrons. The small length scales and large surface-to-volume ratio mean that surface defects play a stronger role in controlling properties of nanomaterials. For example, in order to achieve *p*-type ZnO with sufficient hole concentration, it is necessary to carefully balance between extrinsic doping and intrinsic defect concentration [25]. Similarly, magnetic properties in nano dilute magnetic semiconductors (DMS) are highly dependent upon the native defect density, grain boundaries and absorbed gases. Many researchers have also observed an unexpected presence of ferromagnetic (FM) ordering in nanostructured non-magnetic metal oxides. The study of magnetism in (non-magnetic) oxide nanostructures started with the observation of high temperature FM in nanophase oxides started with reports of HfO_2 and CuO exhibiting FM [26]. Then followed a cascade of communications reporting high temperature FM in other oxides, such as CaO, MgO, ZnO, CeO_2, Al_2O_3, In_2O_3 and SnO_2 [27-29]. Interestingly, it was reported that as the thickness of ZnO films increases, the FM per unit volume decreases, implying that the FM is due to surface defects [30, 31]. FM observed in nanophase TiO_2 was also attributed to surface defects [32]. Furthermore, it is widely believed that the FM in many metal oxides originates from oxygen vacancies [27-36]. The nature and concentration of defects vary with conditions of preparation and therefore controversies regarding reproducibility are commonplace [37-40].

Importantly, systematic studies aimed at unraveling the origin of FM in these oxides are lacking. ZnO, which exhibits properties that are well suited for applications [41], is an ideal system for gaining insights into the origin of FM since it can be readily synthesized in various forms at different length scales such as nanocombs, nanorings, nanosprings, nanobelts, nanowires, nanospheres, and micron-sized cubes. In this chapter, we correlate the changes in the magnetic and optical behavior of pristine ZnO prepared using chemical vapor deposition (CVD) and pulsed laser vaporization (PLV) techniques as a function of thermal treatments in Ar, O_2 and/or Zn vapors. In addition, this chapter also presents *ab-initio* calculations and non-linear optical properties, which suggest that extended defects are responsible for the observed FM.

3.2 Synthesis and Characterization of ZnO nanostructures

The PLV and CVD techniques have been used extensively since the discovery of high temperature superconductors. Soon after Iijima's nanotube discovery in 1991, Smalley and coworkers at Rice University employed high-powered lasers to produce small quantities of high purity, single-walled carbon nanotubes samples (70-80% purity) [42]. Subsequently, several researchers have also used chemical vapor deposition system to carbon nanotubes and other nanomaterials. For instance, these methods have been widely used in a number of studies to grow nanowires of various materials, such as silicon, zinc oxide, and many others [43]. A simple description of the PLV and CVD systems used for the growth of ZnO nanowires is described below.

3.2.1 ZnO nanowire synthesis using pulsed laser vaporization:

The first step involves the deposition of Au nanoparticles on silicon substrates. 0.5-1 ml of poly-L-lysine was dropped on the Si (100) substrates and was allowed to set for 30 seconds before a rinse with distilled water. Once the substrates are reasonably dry, a drop of gold colloid solution (Ted Pella Inc.) with mean diameter 9.5±2 nm is placed on the substrate for 5 seconds before another rinse with distilled water. Once the substrates were prepared they were then loaded into a 1" diameter quartz tube and placed directly in front of a ZnO target. The quartz tube was evacuated and back filled with Ar three times, to attain a final operating pressure of ~160 torr. A gentle flow of Ar was maintained as the furnace temperature was ramped to 850^{o}C and during the ablation process, which typically lasted for 3-5 min. The ZnO target was ablated with the 1064 nm beam (650 mJ) obtained from a Nd:YAG laser operated at 20 Hz.

3.2.2 Chemical vapor deposition of ZnO Nanowires and nanotetrapods:

A 50 mM aqueous solution of $ZnCl_2$ was injected (rate of 0.1 ml/min) into a 1" quartz tube reactor maintained at 550 ^{o}C. A constant flow (10:1) of O_2 and H_2 was maintained at 500 sccm. Si (100) substrates favor the growth of conical shaped ZnO nanowires whereas a combination of micron-scale and nano-scale structures of ZnO is preferentially formed on pyrex substrates.

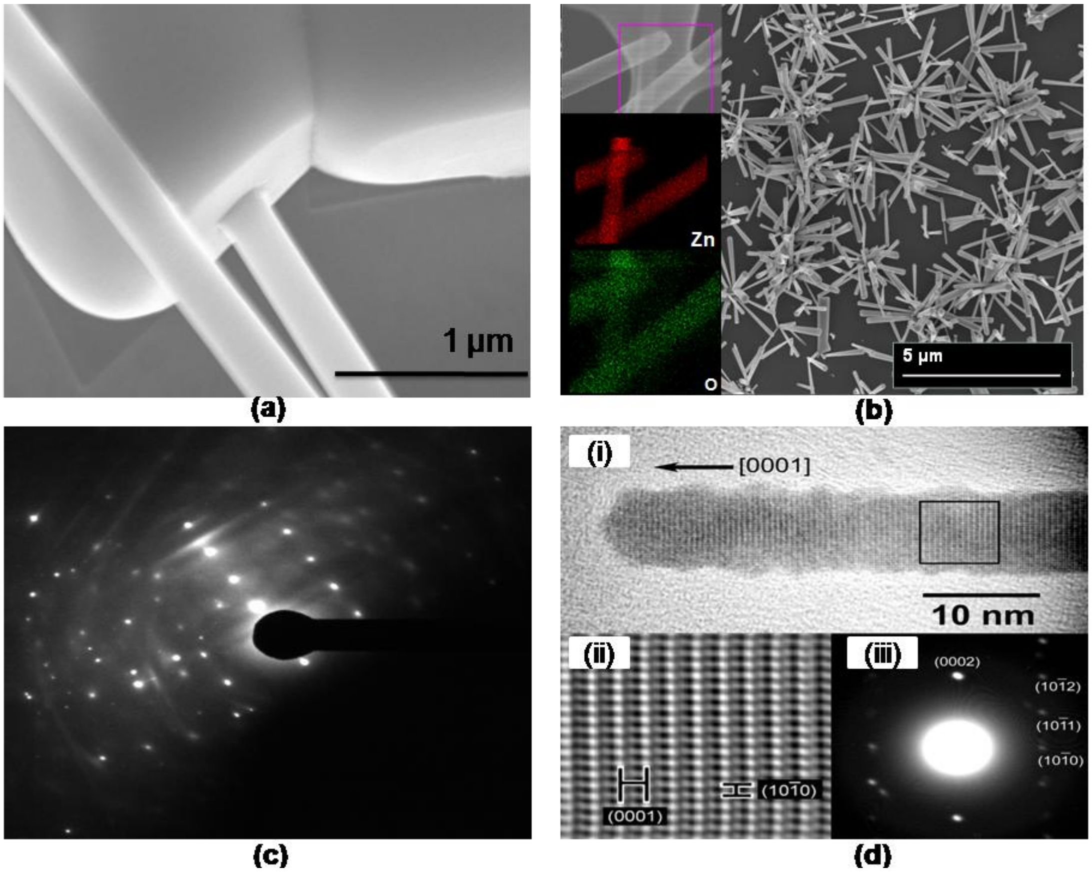

Figure 3.2.1: (a) SEM images of as prepared CVD ZnO nanostructures on Si (100) substrates. (b) SEM images of as prepared CVD microstructures on pyrex substrates. A combination of micron-scale and nanoscale ZnO structures is observed. The inset depicts the elemental analysis which shows no impurity phases in these samples (c) Typical electron diffraction pattern for samples depicted in panels (a) and (b). (d) (i) HRTEM image of an individual PLV grown ZnO nanowire, (ii) a magnified view of the boxed area in (i), and (iii) electron diffraction pattern obtained from a ZnO nanowire shown in (i).

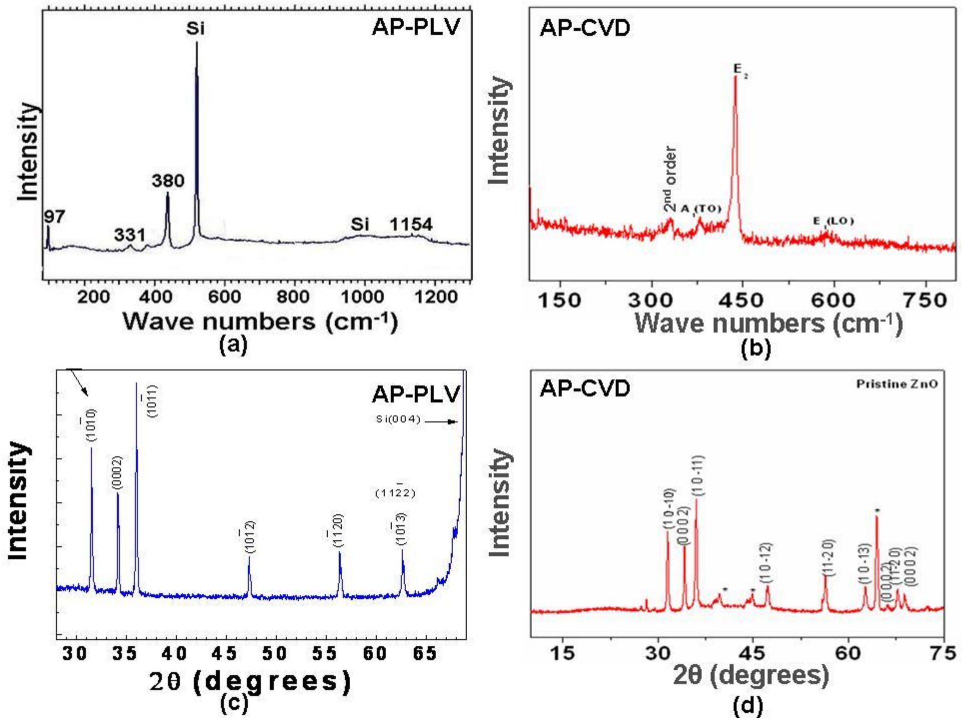

Figure 3.2.2: X-ray diffraction (bottom two panels) and Raman characterization (top two panels) of as prepared PLV (AP-PLV; cf. Fig. 3.2.1d) and CVD (AP-CVD; cf. Fig 3.2.1a ZnO nanostructures. Note that the peaks indicated by the * in (d) correspond to the Al sample holder, and the Si peak in (a) is due to the Si substrate.

Fig. 3.2.2 a-b shows the Raman spectra obtained using Ar^+-ion laser excitations at 514.5 nm in a Horiba-JY Triax 550 single grating spectrometer equipped with liquid nitrogen cooled CCD. All the samples (PLV and CVD) showed the 379 cm^{-1} (A_1 (TO)), 580 cm^{-1} (E_1 (LO)), and 437.5 cm^{-1} (E_2) modes in addition to the second order peak at ~337 cm^{-1}. As shown in Fig.3.2.2 c-d, the X-ray diffractograms of both CVD and PLV samples are also in agreement with the standard JCPDS data for wurtzite ZnO (powder diffraction file #36-145). Sharper peaks are observed in the PLV grown sample than in the CVD samples, indicating their higher crystallinity.

Transmission electron microscopy of PLV nanowires:

The bright field TEM images of PLV nanowires Fig. 3.2.1 d show that the nanowires have an average diameter of 13 nm. The Miller indices and the corresponding *d*-spacings associated with the diffraction rings indicate that the ZnO nanowires have the wurtzite structure. A high-resolution lattice image of a single PLV ZnO nanowire is shown in Fig. 3.2.1 d. The inter-planar spacing for the two perpendicular sets of planes (0001) and (10-10) are in good agreement with that of wurtzite ZnO. The spot diffraction pattern shown in Fig.3.2.1d confirms that the nanowires are single crystals. The relative orientation of the spots with respect to the nanowire length indicates that the growth direction of the nanowire is along the c-axis.

TEM of CVD nanowires:

Fig.3.2.3 shows the selected area diffraction (SAD) pattern and the corresponding real lattice image planes of the nanowires. The measured angles (between the spots) and distances (from the central spot) match the simulated SAD patterns corresponding to [210] or [120] zone axes (obtained using *Crystal Maker* software). The convention for the distance and angles of the diffraction spots are defined in Fig.3.2.4. As shown in Table 3.2.1, the calculated ratios and angles (from Fig.3.2.3) approximately match the simulated image (Fig.3.2.4). Thus, the analysis of diffraction pattern indicates that the growth direction is perpendiculat to [210].

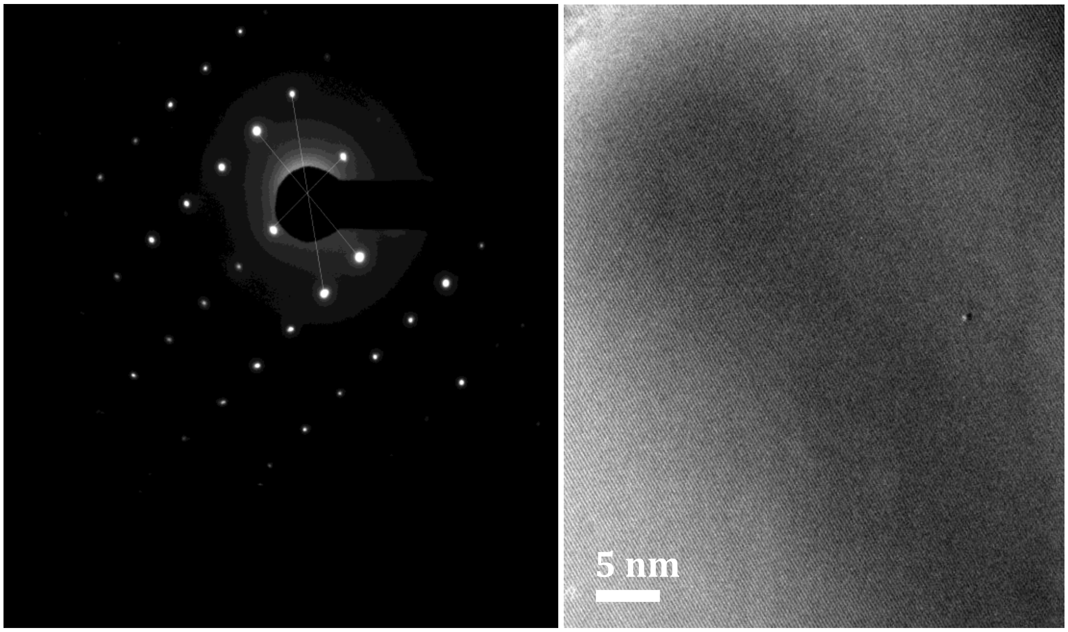

Figure 3.2.3: Typical SAD pattern (left panel) of CVD grown ZnO nanowires. The corresponding lattice image is shown on the right.

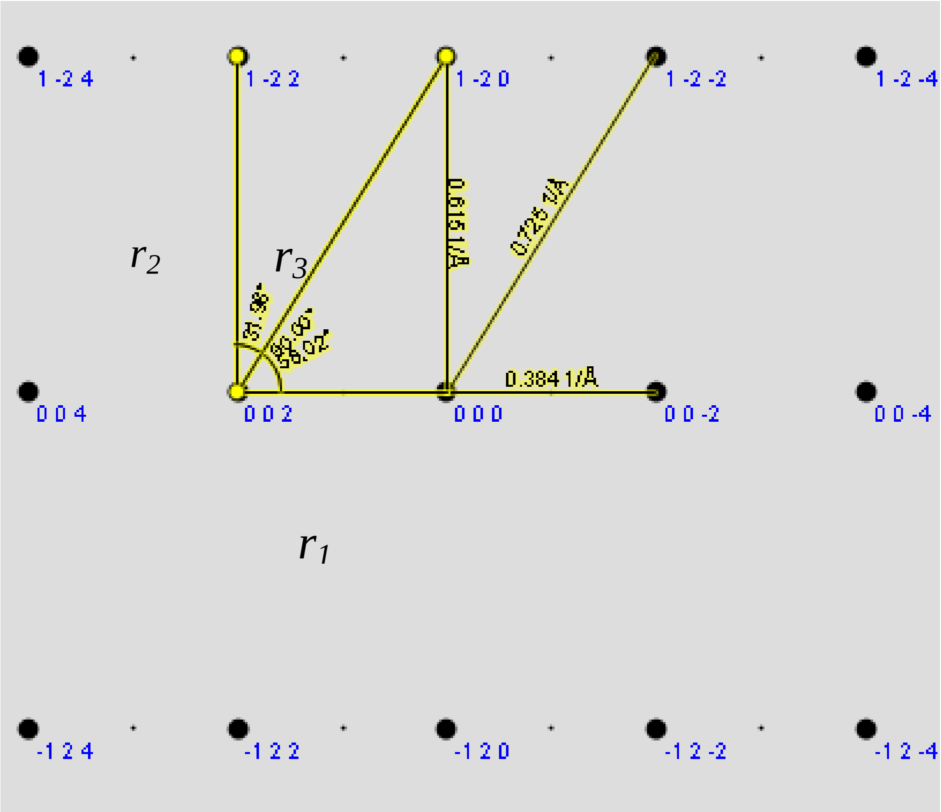

Figure 3.2.4: Simulated electron diffraction pattern along [210] zone axis corresponds to the SAD shown in Fig. 3.2.3.

	Experimental Pattern	Simulated Pattern
r_1/r_2	0.618	0.624
r_1/r_3	0.523	0.529
Angle between r_2 and r_3.	32.36˚	31.98˚
Angle between r_1 and r_3.	57.64˚	58.02˚

Table 3.2.1: A comparision of ratios and angles from the SAD pattern (in Fig. 3.2.3) and the simulated pattern (in Fig. 3.2.4).

3.3 Magnetic properties of pristine and Co-doped nanostructured ZnO

Magnetization studies* were performed using a Quantum Design SQUID MPMS (Model 5S) and the following samples were measured: (i) as prepared (AP-CVD, AP-PLV); CVD grown samples annealed in (ii) an O_2 atmosphere at 100 °C for 5.5 hours (O_2-100-5.5h); (iii) an O_2 atmosphere at 500 °C for one hour (O_2-500-1h) and subsequently exposed to Zn vapors at 500 °C for two hrs (O_2-Zn-500-2h); (iv) an Ar flow at 400°C for 5 minutes (Ar-400-5m) and subsequently exposed to Zn vapors for 2 hours at 500°C (Ar-Zn-500-2h); and (v) Zn vapors at 500°C for two hours (Zn-500-2h). As discussed later in Fig.3.3.2, since room temperature FM was not observed in the PLV prepared samples, these samples were not subjected to the annealing process.

As shown in Fig.3.3.1, a clear evidence for FM is observed in the AP-CVD samples. This FM saturates at low magnetic fields (~ 1 T) and is embedded in a diamagnetic background response. Interestingly, upon annealing in O_2 at 100 °C (O_2-100-5.5h), the FM signature is greatly enhanced as seen in Fig.3.3.1a. It is noteworthy that the sharp transition from a FM to a DM response in the insets in Fig.3.3.1a implies that the measured magnetization is not due to a simple superposition of a ferromagnetic ordering and a diamagnetic response. The signs of saturation at relatively low magnetic fields (~1 T) indicate the presence of reasonably large spin clusters.

*With the help of Dr. Wendy Queen and Palmer West in Prof. Hwu's lab in the Dept. of Chemistry at Clemson University

In addition, field cooled and zero-field cooled magnetization measurements showed the absence of superparamagnetism in these samples. This ferromagnetic ordering may be understood by chemisorption of O_2 to form O_2^-. Since the growth occurs in an O-rich environment, it is probable that O_2 is chemisorbed preferentially near a cluster of Zn vacancies. Given such a possibility one may visualize a dynamic exchange of electrons, as seen in Fig.3.3.1b, between O_2 and O^- leading to FM ordering [44-46].

Furthermore, this FM ordering and hence the sharp transition is absent in AP-CVD samples when annealed in Ar at 400 ^oC for a short period of time (Ar-400-5m, Fig. 3.3.1a). The HRTEM image (Fig. 3.3.1c) shows the polycrystalline nature of the AP-CVD samples. Annealing in Ar presumably leads to (i) the merging of grains, which consequently reduces the net surface/interfacial area [47], and (ii) reduced amount of chemisorbed O_2 in the sample, which results in a diamagnetic response.

Independent experiments to further confirm the loss in the FM ordering as a result of high temperature- induced merging of grains were performed. An AP-CVD sample annealed in O_2 at 500 °C for 1 h (O_2-500-1h) showed an absence of ferromagnetic ordering (Fig. 3.3.2a). Similarly, the PLV grown ZnO samples did not show ferromagnetic ordering (Fig. 3.3.2b), and this observation is consistent with the *ab-initio* calculations discussed later in Fig. 3.3.3d. Alternatively, since ZnO may have Zn defects, the AP-CVD samples were annealed in Zn vapor at 500 °C. The magnetization data for this sample (Zn-500-2h) shows a much suppressed response as compared to the AP-CVD sample (Fig. 3.3.2a).

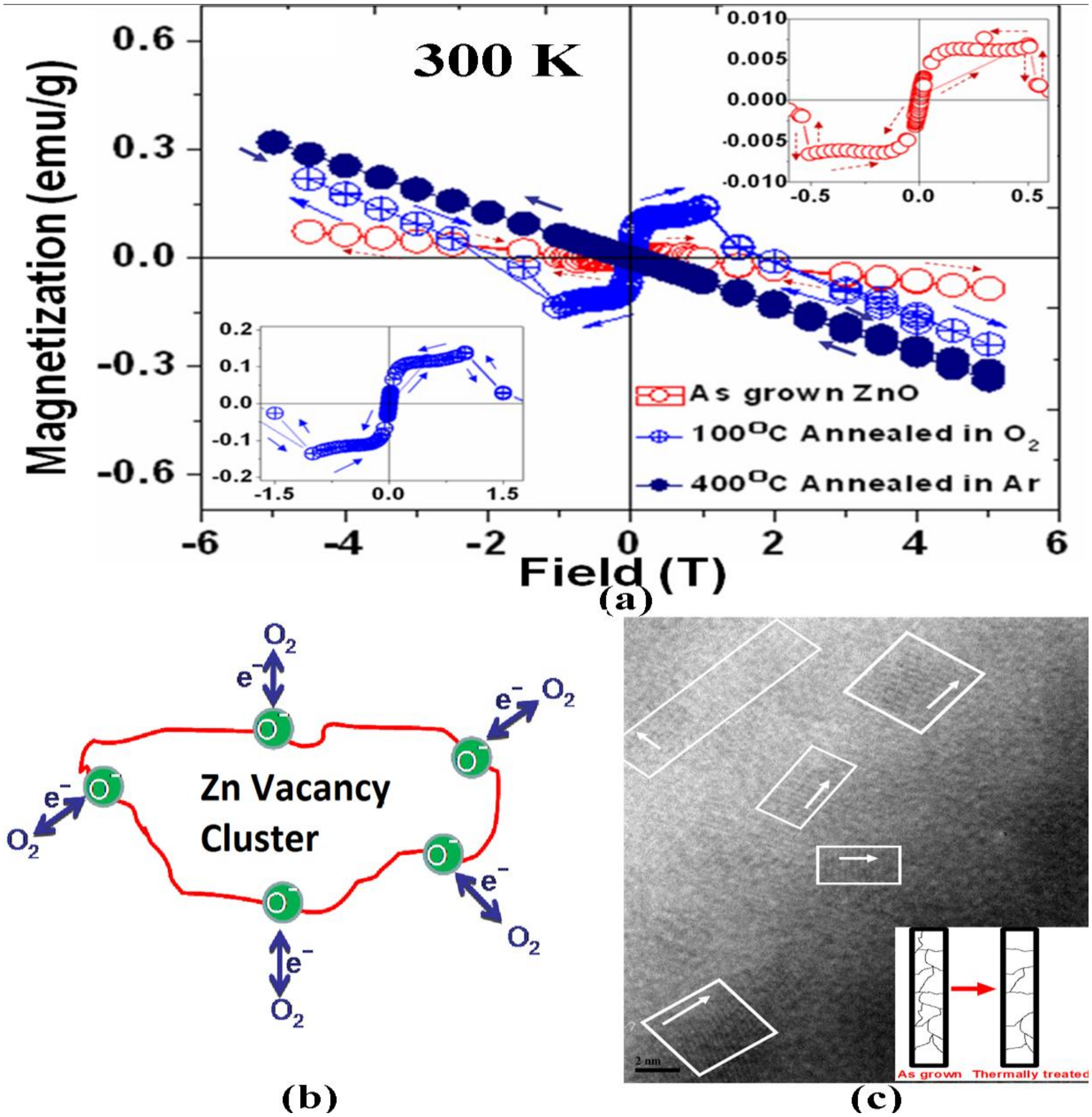

Figure 3.3.1: (a) M-H curves of CVD prepared ZnO nanostructures. As grown nanostructures show a weak, but clear (top inset), FM embedded in a dominant diamagnetic response. The bottom inset shows enhancement in FM ordering by at least an order of magnitude when annealed in O_2 at 100 ^{o}C. (b) O_2 chemisorbs near a cluster of Zn vacancies and a dynamic exchange of electrons between the oxide ions and O_2 could lead to FM. (c) HRTEM image showing the polycrystalline nature of CVD grown ZnO

nanostructures. The inset shows schematically the effect of how thermal treatment might alter the grain size in these nanostructures.

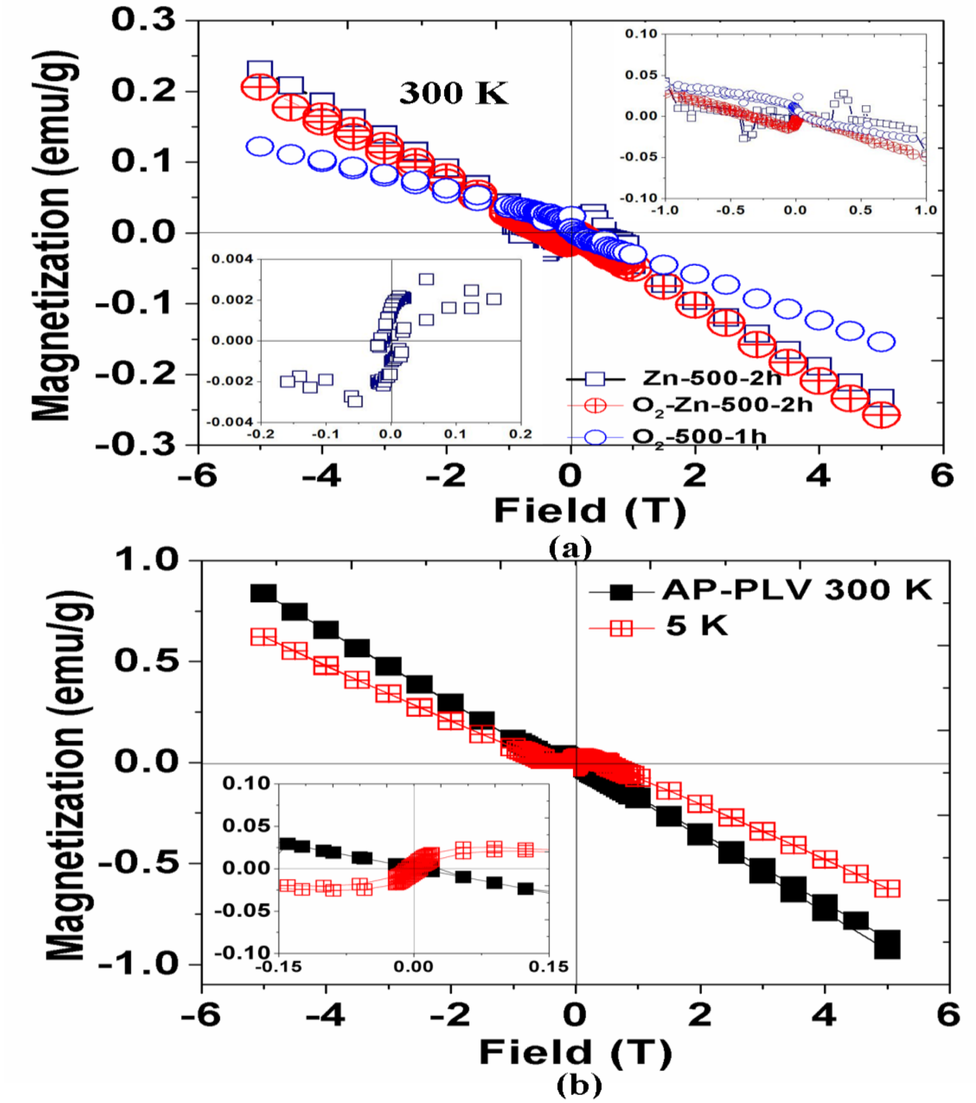

Figure 3.3.2: (a) CVD prepared ZnO nanostructures annealed in oxygen at 500 ºC for 1 hr and re-annealed in Zn vapors at 500ºC for 2 h exhibit a diamagnetic response. Further, a much suppressed FM is seen in as prepared ZnO nanostructures when annealed in Zn

vapors at 500ºC for 2 hrs. (b) Magnetization data for AP-PLV ZnO nanowires do not exhibit FM ordering at 300 K, and show negligible FM at 5 K. In both panels, the inset figures show an expanded view in the low field regime.

Alternatively, *ab-initio* calculations* show that the net magnetization could arise from two possible contributions: one due to localized O_p orbitals and the other due to delocalized O_p orbitals. In this model, the localized orbitals (p_x) are preferentially aligned perpendicular to the wire direction, whereas the delocalized orbitals (p_z) point in a direction parallel to the wire direction. This suggests that the localized orbitals contribute a local moment, forming a paramagnetic center that can interact with other such centers through the delocalized orbitals and thus result in a net magnetization. In Fig. 3.3.3a, we show the spin charge density, i.e., spin up charge density minus the spin down charge density, for a ZnO nanowire along the [1-210] direction. It should be mentioned that although we pick a wire direction in our model calculations, unlike the PLV nanowires, the AP-CVD samples do not have a unique growth direction due to their polycrystalline nature. Therefore, we have computed net magnetization for several wire directions (Fig. 3.3.3d). A strongly localized moment is observed near the surface of the nanowires (ferromagnetic ordering), while the interior of the wire does not show a similar strong contribution (diamagnetic response).

The origin of such magnetization in O *p*-orbitals is further supported by the presence of unpaired oxygen *p* levels at the Fermi energy in the projected density of states (PDOS) (Fig. 3.3.3b). The existence of spin polarization for a certain kind of defects is not sufficient to warrant a *macroscopic* magnetization. In other words, intrinsic point defects may also lead to spin-polarization, but not necessarily to macroscopic magnetization.

For instance, Zn vacancies in *bulk* ZnO are spin polarized. However, their population will never be large enough in order to allow a magnetic interaction between two impurity sites. In AP-CVD samples, we observe the formation of extended defects e.g., the surface (cf. HRTEM image in Fig. 3.3.1c). Such extended defects lead to the formation of surface states in the band structure, which is shown schematically in Fig. 3.3.3c.

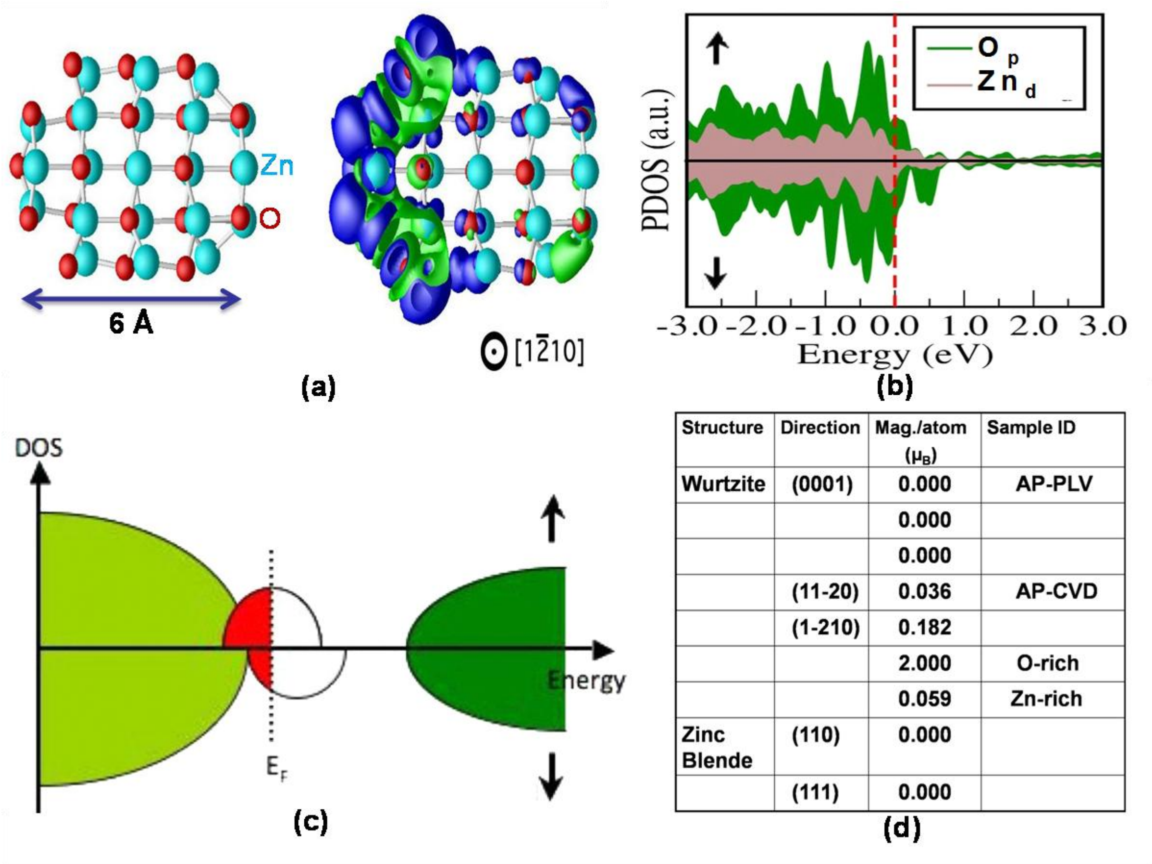

Structure	Direction	Mag./atom (μ_B)	Sample ID
Wurtzite	(0001)	0.000	AP-PLV
		0.000	
		0.000	
	(11-20)	0.036	AP-CVD
	(1-210)	0.182	
		2.000	O-rich
		0.059	Zn-rich
Zinc Blende	(110)	0.000	
	(111)	0.000	

*In collaboration with Dr. Gustavo Dalpian's group at UFABC, Brazil.

Figure 3.3.3: (a) Cross sectional view of a [1-210] nanowire, as obtained after relaxing all forces in our calculations. The figure in the right shows the spin charge density for the [1-210] nanowire. (b) Calculated projected density of states for ZnO nanowires. The upper panel is for spin-up and the bottom for spin down. The dotted line represents the Fermi energy. (c) A schematical view of the density of states. The bands in light and dark green are respectively the valence and conduction bands. The red bands represent delocalized surface states and the dotted/dashed lines represent the Fermi energy. (d) The table shows magnetization obtained per atom in our calculations for different wire directions and structures.

3.3.1 Effects of Dopants:

In order to understand the effects of dopant atoms on the magnetic properties of ZnO nanostructures, we synthesized Co doped ZnO nanostructures using CVD technique. Briefly, a 50 mM aqueous solution of $ZnCl_2$ was injected (rate of 0.1 ml/min) into a 1" dia. quartz tube reactor maintained at 550 °C. An appropriate amount (2 *at.%*) of $Co(CH_3COO)_2$ was added to the $ZnCl_2$ to prepare the 2% Co- doped nanostructures. A constant flow of O_2 and H_2 (10:1) was maintained at 500 sccm.

Figure 3.3.4 shows electron microscope images of 2% Co doped ZnO nanostructures prepared by the CVD technique. Energy dispersive X-ray spectroscopy (EDX) was employed to confirm the presence of the Zn, Co and O atoms in the nanostructures (Fig

3.3.4a). The distribution of Co dopants was observed to be fairly uniform for 2% Co doped ZnO nanostructures.

In addition to the pristine sample described in the previous section, magnetization studies were performed the following samples :(i) Co doped ZnO (AP-CoZnO); (ii) Co doped ZnO samples annealed in an O_2 atmosphere at 100 °C for 5.5 hours (Co-O_2-100-5.5h); (iii) Co doped ZnO samples annealed in an Ar atmosphere at 400 °C for 5 minutes (Co-Ar-400-5m).

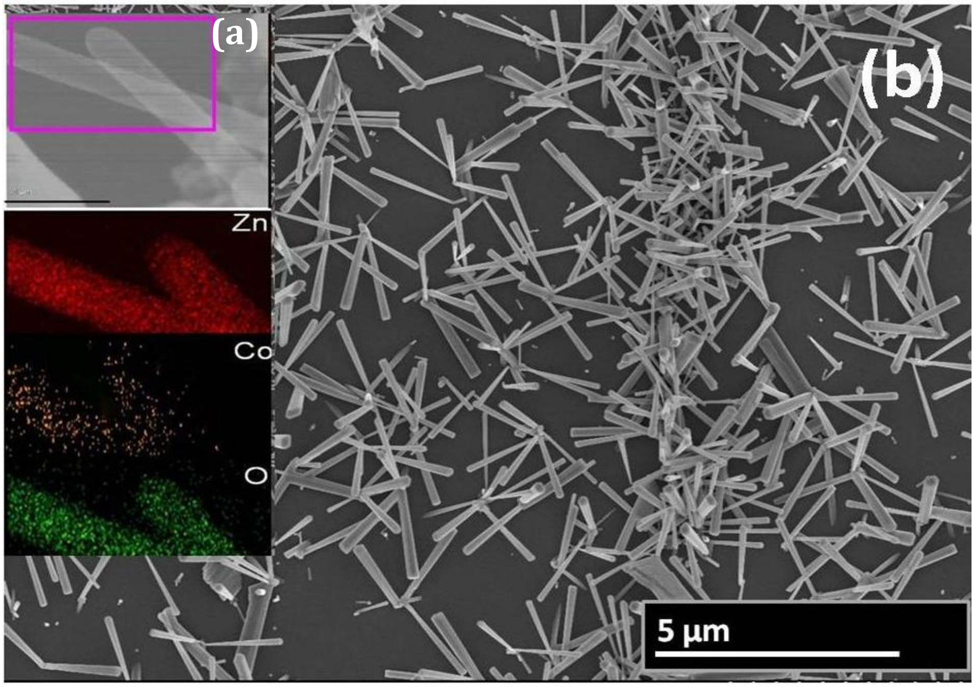

Figure 3.3.4: EDX spectra (shown in (a)) and the scanning electron microscope images of 2% Co doped ZnO nanostructures on Si (100) substrates (shown in (b)). Along with Zn and O, uniform distribution of Co was confirmed as seen in the lower left panel.

As shown in Fig.3.3.5, FM observed in AP-CoZnO samples also saturates at low magnetic fields (~ 1 T) similar to AP-CVD samples (cf. Fig. 3.3.1) and is embedded in a background DM response similar to pristine ZnO. Unlike AP-CVD samples, a sharp transition from FM to diamagnetism is absent in AP-CoZnO samples (Fig. 3.3.5). The absence of a sharp transition indicates that the FM ordering and DM originate from two different sources viz., FM from Co dopants and diamagnetism from ZnO. Furthermore, in the case of AP-CoZnO samples, the transition from FM to DM response does not occur until ~2-3 T, suggesting that the robust FM is due to the presence of Co atoms in the ZnO lattice. It is noteworthy that the net normalized magnetic moment for AP-CoZnO (~ 25 memu/g) samples is at least three times larger than the pristine ZnO nanostructures (~7 memu/g), confirming the enhancement of FM due to Co doping. Thus the FM ordering in AP-CoZnO samples may be understood in terms of Co atoms substitutionally doping the Zn sites. The formation of Co clusters in our samples is highly unlikely, since the nominal doping concentration (2 at %) is very low. Also, EDX confirms uniformly distributed Co in AP-CoZnO samples (Fig. 3.3.4). In addition, no signs of Co clusters were observed in either TEM or X-ray diffraction.

Annealing effects on FM for AP-CoZnO samples were found to be similar to AP-CVD samples. We observed an increase in the net normalized magnetic moment from ~25 memu/g to ~45 memu/g upon annealing the AP-CoZnO samples in O_2 at 100 °C (Co-O_2-100-5.5h; Fig. 3.3.5). We also observed a DM response in AP-CoZnO samples annealed at 400 °C in Ar for 5 minutes (Co-Ar-400-5m; Fig. 3.3.5).

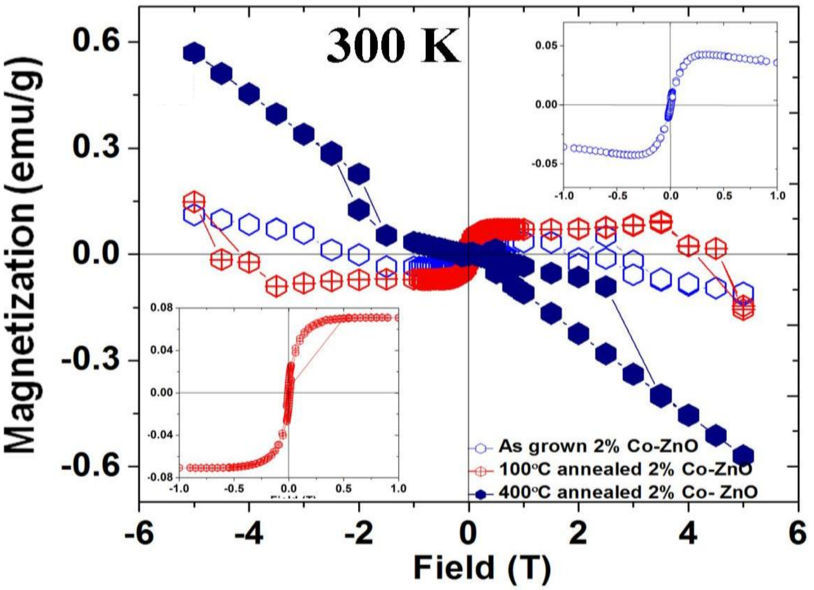

Figure 3.3.5: M-H curves of CVD prepared Co doped ZnO nanostructures at room temperature. As grown Co doped ZnO nanostructures (top inset) exhibit at least 3 times stronger magnetization than pristine ZnO nanostructures. The bottom inset shows enhancement in FM ordering when annealed in O_2 at 100^{o}C.

3.4 Non-linear Optical Studies

The magnetic properties of pristine and doped nanostructured ZnO are strongly influenced by the intermediate states in the band gap. In order to understand such intermediate defect states, we performed NLO measurements using the open aperture Z-scan technique (see chapter 2) with linearly polarized 5 ns optical pulses from a Q-switched frequency-doubled Nd:YAG laser at 532 nm. The samples solutions in isopropyl alcohol were contained in 1 mm thick quartz cells for measuring the change in transmittance.

The Z-scan is a nonlinear optical measurement, in which the light-induced change in transmittance (ΔT) of a medium due to optical nonlinearity is measured as a function of input light energy density (fluence) or intensity. From this one can calculate the nonlinear absorption and refraction coefficients. In the experiment, a continuous variation of the input fluence is achieved by translating the sample under study through the focal region of a focused laser beam (the sample position is taken as z with $z = 0$ being the focal point for the incident laser beam; hence the name "Z-scan"). A detailed description of the Z-scan technique can be in section 2.4. The key point to note here is that except when excited by ultrafast laser pulses, ΔT strongly depends on the excited state population density. In view of this, we have measured the nonlinear transmission of the present samples in the nanosecond excitation regime, using linearly polarized 5 ns optical pulses from a Q-switched frequency-doubled Nd:YAG laser operating at 532 nm. The Z-scan data obtained for AP-CoZnO and pristine ZnO samples (Figs. 3.4.1a and b respectively) are found to be best-fit numerically by a three-photon absorption (3PA) process. The nonlinear absorption coefficient α in the presence of 3PA is given by $\alpha(I) = \alpha_o + \gamma I^2$, where I is the intensity of the laser, α_o the unsaturated linear absorption coefficient, and γ the 3PA coefficient. The value of γ is obtained by fitting the Z-scan curve to the 3PA propagation equation, given by, $\frac{dI}{dz'} = -\alpha_0 I - \gamma I^3$, where z' is the propagation distance within the sample.

The values of γ numerically obtained from the fits indicate that nonlinear absorption in the present case arises not only from genuine 3PA, but also from “effective” three-photon nonlinearity [48, 49]. Such effective 3PA originates from sequential excited state absorption as shown in inset of Fig. 3.4.1a. In the case of genuine three photon absorption (3PA), where the transition states involved are virtual, the 3 PA coefficient (γ) is a constant and is independent of the incident laser fluence. All genuine ground state absorption coefficients (such as 2 PA or 3PA) are dependent on the ground state population N, since the absorption coefficient is obtained by multiplying the corresponding absorption cross section (σ) by N. The absorption cross section is a microscopic parameter, independent of N, that characterizes the average two photon/three photon absorbability per molecule. However, the change in γ will be evident only when there is a substantial change in the ground state population due to the absorption. Therefore if the absorptions are weak, the coefficients can be considered to be almost constants, since there is a negligible change in N. Genuine 2PA and 3PA are usually very weak phenomena, and hence the corresponding coefficients can be considered as material constants at a given wavelength and concentration. But strong excited state absorptions (ESA) during an effective 3PA may deplete the ground state population significantly so that the absorption coefficient is no more a constant. Hence a change in γ w. r. t incident laser intensity can help confirm the presence of surface states in the forbidden gap of ZnO.

Both two-photon absorption and/or sequential absorption of two photons at 532 nm (2.33 eV; inset Fig. 3.4.1a) will result in a *real* terminal level which is above the lowest excitonic state that lies around 363 nm (3.4 eV) for ZnO, and another one-photon absorption to go from this level to the band edge. Figs. 3.4.1c & d show the variation of γ for AP-CoZnO, AP-CVD, O_2-100-5.5h and Ar-400-5m respectively, as a function of incident laser energy. While γ remains almost a constant with input energy in AP-CVD, there is a pronounced increase in γ with incident energy in AP-CoZnO and O_2-100-5.5h samples. Moreover, the 3PA coefficient (and hence the optical limiting efficiency) for AP-CoZnO samples is obviously higher than that of pristine ZnO. These observations concur with the enhancement seen in the magnetic moment of AP-CoZnO & O_2-100-5.5h samples and indicate the presence of an enhanced surface state density due to Co atoms in the ZnO lattice. Thus the increase of γ with the incident laser energy confirms an effective 3 PA due to the existence of a wide range of surface states in AP-CoZnO and O_2-100-5.5h samples. Furthermore, the lowest γ values and a constant trend with input fluence were observed for Ar-400-5m samples indicating the absence of any surface states. Thus, we believe that an enhanced surface state density in AP-CoZnO due to Co doping results in stronger FM and better optical limiting as compared to pristine ZnO nanostructures.

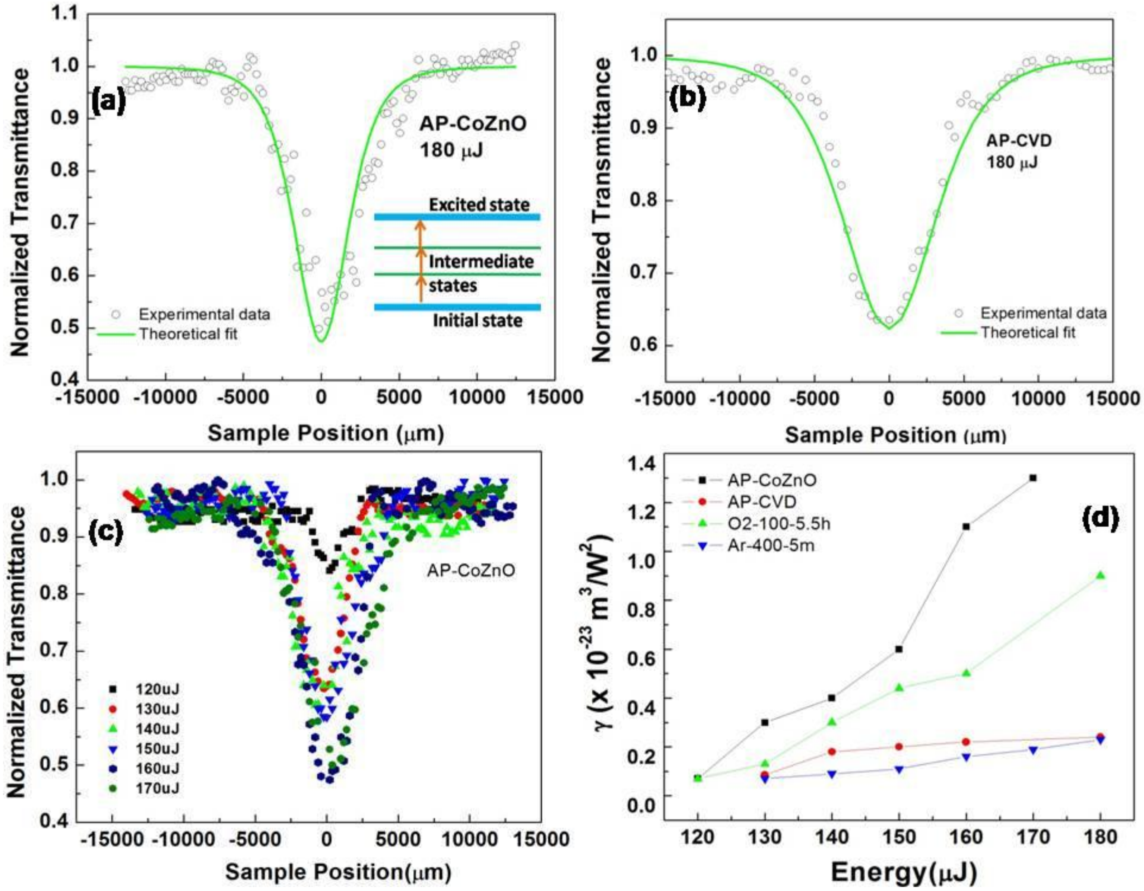

Figure 3.4.1: a) Z-scan data for AP-CoZnO samples fitted to a three-photon absorption (3PA) equation. Inset is a schematic depicting effective 3PA. When the intermediate states are virtual the effect is genuine 3PA, but when they are real it is an effective 3PA arising mostly from excited state absorption. (b) Z-Scan data for pristine ZnO samples fitted to a 3PA equation. (c) Z-scan data for AP-CoZnO samples at different incident laser energies. (d) Variation of the 3PA coefficient (γ) as a function of the incident laser pulse energy for AP-CVD, AP-CoZnO, O2-100-5.5h and Ar-400-5m samples.

To summarize, unlike AP-PLV nanowires, the AP-CVD samples showed a weak but clear FM signature, thus confirming the role of surface defects in FM ordering. Low-temperature (~100 °C) annealing of AP-CVD samples in flowing oxygen enhances the ferromagnetic ordering; this enhancement is attributed to an increase in the amount of chemisorbed oxygen. However, annealing at high temperatures (~500 °C), irrespective of the environment, leads to a diamagnetic response due to an increase in the crystal grain size. A model based on the dynamic exchange of electrons between chemisorbed O_2 and O near a cluster of defects was proposed. Possible explanations based on macroscopic magnetization observed in simulations of ZnO nanowires, using *ab initio* calculations were also discussed. The 2% Co-doped ZnO nanostructures (AP-CoZnO) samples showed FM signature similar to AP-CVD and AP-PLV samples. The magnitude of the observed change in magnetization was pronounced for AP-CoZnO samples and is presumably due to the presence of Co induced intermediate states. As expected, a sharp transition from FM to DM was not observed in AP-CoZnO samples indicating the presence of Co dopants in the ZnO lattice. Lastly, we confirmed the presence of intermediate states in the gap region of ZnO nanostructures using Z-scan non-linear optical measurements.

Chapter 4

Role of Defects and Curvature in the Determination of Optical and Vibrational Properties of Carbon Nanostructures

4.1 Introduction

Carbon occurs in several stable forms (or hybridizations), and the dependence of the properties of each form on its special structure makes carbon a truly unique building block for nanomaterials. Carbon has been investigated for the past 60+ years without exhausting its wonders and challenges. Especially with the discovery of single layer graphene, researchers are still finding new properties for carbon nanostructures. As discussed in chapter 1, single monolayer graphene (SLG), the planar honeycomb lattice of sp^2 hybridized carbon atoms, is often considered to be mother of nanocarbon systems. Although this system can be large (ideally infinite in-plane), it is only one atom thick, thus representing a two-dimensional (2D) sp^2 nanocarbon system containing two atoms per unit cell, A and B (Figure 1.1.1). A stacking of 2 or 3 single layers results in bi-layer (BLG) and tri-layer graphene (TLG). In the formation of such multilayer graphene (MLG), stacking order is important with the AB Bernal stacking (shown in Figure 1.1.3) leading to the lowest energy geometry (ground state) and with an equilibrium *c*-axis (distance between the layers) lattice constant of 0.335 nm. Rolling-up a narrow strip of SLG in a seamless way into a cylinder forms a single-wall carbon nanotube (SWNT). Conceptually, nanotubes can be infinitely long, thus representing one-dimensional systems. By adding one- and two-layer concentric cylinders to a SWNT, we get double- and triple-wall carbon nanotubes, and by adding many rolled-up concentric cylinders, a multiwall carbon nanotube (MWNT) is obtained. A piece of graphite with small lateral dimensions (a few hundred nanometers and smaller) is called nanographite, which is similar to a zero-dimensional (0D) system.

4.1.1 Raman Spectroscopy of Carbon nanomaterials:

Raman spectroscopy has played a very important role in the study and characterization of graphitic materials [50]. It has been used to characterize highly ordered pyrolytic graphite (HOPG), carbon fibers, glassy carbon, pitch-based graphitic foams, nanographite ribbons, fullerenes, carbon nanotubes, and graphene [50-57]. For sp^2 nanocarbons such as graphene and carbon nanotubes, Raman spectroscopy can give information about the following: in-plane crystallite size (L_a), the presence of sp^2–sp^3 hybridization, the introduction of chemical impurities (or charge transfer), the optical energy gap, elastic constants, doping, defects, edge structure, strain, number of graphene layers, nanotube diameter, chirality, curvature, and finally the metallic *vs* semiconducting behavior.

In this chapter, we discuss the effects of layer stacking, defects, dopants and curvature on the optical and vibrational properties of SWNTs and graphene. We correlate the changes in optical absorption and Raman spectra of carbon nanostructures to their defects and curvature. The outline of the chapter is as follows: the first section discusses synthesis of single-, bi- & few-layered graphene. Section 4.3 and 4.4 elucidate the effects of layer stacking and defects on the optical and vibrational properties of graphene. Finally, section 4.5 describes the curvature-induced symmetry breaking and the origin of intermediate frequency modes in the Raman spectra of SWNTs.

4.2 Synthesis of Single-, Bi- & Few-layered Graphene

4.2.1 Mechanical cleavage:

High quality graphene samples can be obtained using the standard "mechanical exfoliation" technique [58]. This involves cleaving HOPG by placing it on Scotch tape and repeatedly folding the tape over graphite and opening it up again. Once the tape is coated with a relatively thin layer of graphite, it is pressed onto a 300 nm SiO_2-covered wafer. The back of the tape is rubbed lightly for 1-5 minutes. Finally, the tape is removed from the SiO_2 substrate. The optical image in Fig. 4.2.1 shows a typical sample demonstrating how visible contrast can be used to detect graphene.

4.2.2 Chemical Vapor Deposition:

High quality graphene samples can also be grown using the CVD technique. In CVD, polycrystalline graphene layers are grown on a metal substrate (Cu, Ni, etc.) and are later transferred to any desired substrate (see Fig.4.2.2). For the growth, Cu foils (1 cm x 1 cm) are placed in a 1 in. quartz tube furnace and heated to 1000 °C in the presence of 50 sccm of H_2 and 450 sccm of Ar. Subsequently, methane at different flow rates (1 – 8 sccm) is introduced into the furnace for 20−30 min. The samples are finally cooled to room temperature under flowing H_2, Ar and CH_4. It is important to leave the samples

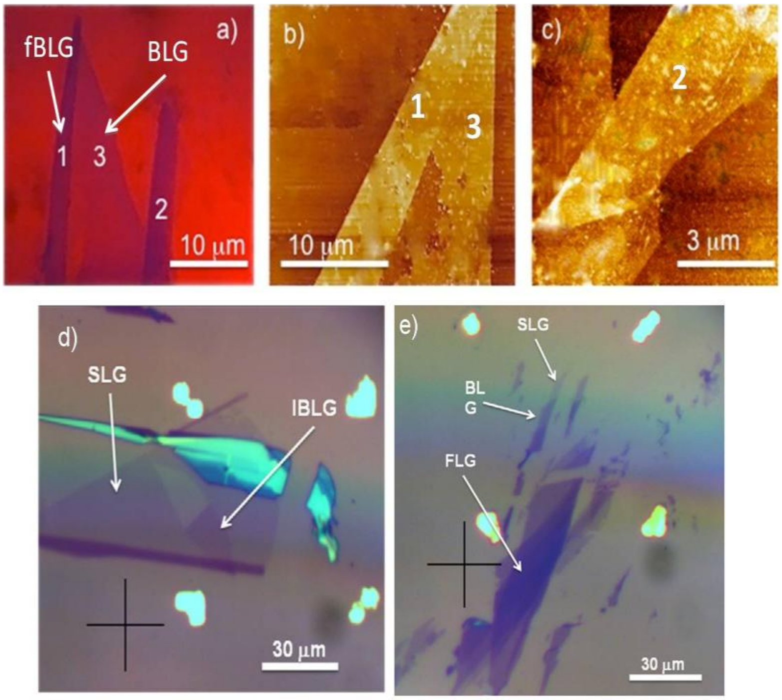

Figure 4.2.1: Typical optical micrograph of mechanically cleaved SLG, BLG, IBLG and folded BLG (fBLG) on 300 nm SiO_2 substrates (a, d and e). Atomic force micrographs corresponding to (a) are shown in (b) and (c).

under flowing gases for 2-3 hours after room temperature is attained. To transfer the graphene layers to the quartz substrates, the Cu substrates are spin-coated with PMMA (diluted with 4% anisole) at 4000 rpm followed by a heat treatment for 5 mins at 150 ^{o}C. Next, the Cu foil is etched away using CE-100 transene etchant leaving the graphene layers attached to the PMMA layer. The graphene attached to PMMA samples is subsequently exposed to 10% HCl for 10 mins, and carefully washed in de-ionized water for 10 mins before (and after) their exposure to 10% HCl. Finally, the sample can be transferred to any desired substrate. Annealing at 450^{o}C in Ar (300 sccm) and H_2 (700 sccm) for 2 hrs is necessary to remove the residual PMMA layer.

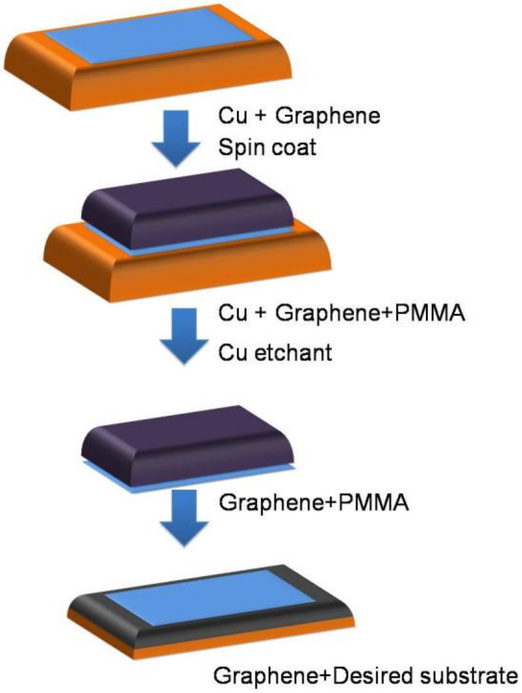

Figure 4.2.2: A schematic showing the steps in the graphene transfer process

4.3 Effects of layer stacking on the optical and vibrational properties of Graphene

Single layer (SLG) and bi-layer graphene (BLG) have recently attracted much attention from the research community, mainly due to their extraordinary electronic properties, which are interesting for both fundamental and applied sciences [59, 60]. SLG and BLG are quite different from each other with respect to their band structure. SLG is a semimetal with a vanishing density of states at the Fermi level [61], while AB-stacked BLG possesses massive Dirac fermions with a transverse-field-tunable band gap [62]. On the other hand, incommensurate BLG (IBLG) behaves in a fashion similar to SLG with reduced Fermi velocities [63, 64].

As mentioned earlier, Raman spectroscopy (See Section 1.2) is the standard technique to distinguish between SLG, BLG, IBLG, and graphene samples with a few layers (FLG) [65]. The most commonly used Raman signature for layer thickness is a peak occurring at ~2700 cm^{-1} called the 2D (also called the G') band, which is an overtone of the disorder-induced D band located at ~1350 cm^{-1} (see section 1.1 for further details). Both the D and 2D bands occur due to an inter-valley double resonance Raman process [66] where the D band phonon scattering is a second order process mediated by a defect, while the 2D band occurs due to scattering by two phonons and does not need any defects for activation. The 2D band in SLG can be fit to a single Lorentzian peak and its intensity has been found to be much higher than that of the G band (located at ~1580 cm^{-1}) for SLG; hence it is often used as an indicator of an SLG region [65, 67-70]. On the other hand, the 2D band in BLG can be clearly deconvoluted into four Lorentzian peaks and its intensity is lower than that of the 2D band in SLG on 300 nm SiO_2 [65]. As the number of layers increase to more than 3 the 2D band evolves into a two-peak structure along with a concomitant decrease in intensity with respect to the G band. It has recently been shown that IBLG can be distinguished from SLG and BLG by the presence of a new defect-induced peak (I band) located on the high frequency side of the D band (Fig. 4.3.1a) [71]. The I band appears due to one layer imposing a perturbation on the other and is a signature for the presence of non-AB stacked graphene. Moreover, frequency of the I band depends on the angle between the two incommensurate (parent and the folded layer) layers [71].

However, the truncation of translational symmetry in finite size graphene activates vibrational modes that are not at the center of Brillioun zone. These modes occur due to the combination of the optical and acoustic phonons in graphene. We have performed detailed investigations of such combination modes involving iTO, LO and TA phonons in SLG, BLG, FLG and IBLG and observed three new features in the region between 1650 and 2300 cm^{-1}. (1) We observed a previously unidentified dispersive mode at ~1880 cm^{-1} ($iTALO^{+}$) when excited with E_{laser} = 2.33 eV in SLG, which strongly depends on the number and stacking order of graphene layers. This mode was tentatively assigned as a combination of the oTO + LO phonons mode around the K point in the graphene Brillouin zone. (2) Another previously unidentified mode was observed at ~2220 cm^{-1} in SLG (when excited with E_{laser} = 2.33 eV). This mode has a negative dispersion with respect to laser energy and was tentatively assigned as a combination of the iTO and iTA phonons (iTOTA mode) around the K point. (3) The combination modes involving the LO phonon ($iTALO^{-}$, $iTALO^{+}$, and LOLA modes) upshift in frequency with increase in the number of graphene layers, while the iTOTA mode frequency downshifts with increasing graphene layers. An additional stiffening of all the combination modes wass observed for IBLG.

Fig. 4.3.1a shows the D and G band region and the G' band regions from the graphene samples collected using E_{laser} = 2.33 eV. Also included in Fig. 4.3.1 are spectra collected from bulk graphite (HOPG). The D band intensity is very low across all graphene samples and is negligible for HOPG. Not surprisingly, the I_D/I_G value for IBLG is the highest and it decreases in general as the number of graphene layers increase as shown in the inset in Fig. 4.3.1a. In addition, a second peak in the D band region can be observed in the IBLG spectrum. This peak, called the I band, appears at 1374 cm^{-1} and can be used as a metric for identification of IBLG. The 2D band from SLG, BLG, FLG and HOPG can be fit to 1, 4, 2 and 2 Lorentzian peaks, respectively, thus indicating presence of 1, 2, few layer graphene or bulk graphite (Fig. 4.3.1b) in a specimen. The Raman signature from IBLG is different from both SLG and BLG; the 2D band intensity is higher than the G band, but reverts to a single Lorentzian peak similar to SLG with a blue-shifted (~ 7 cm^{-1}) frequency [64, 72, 73].

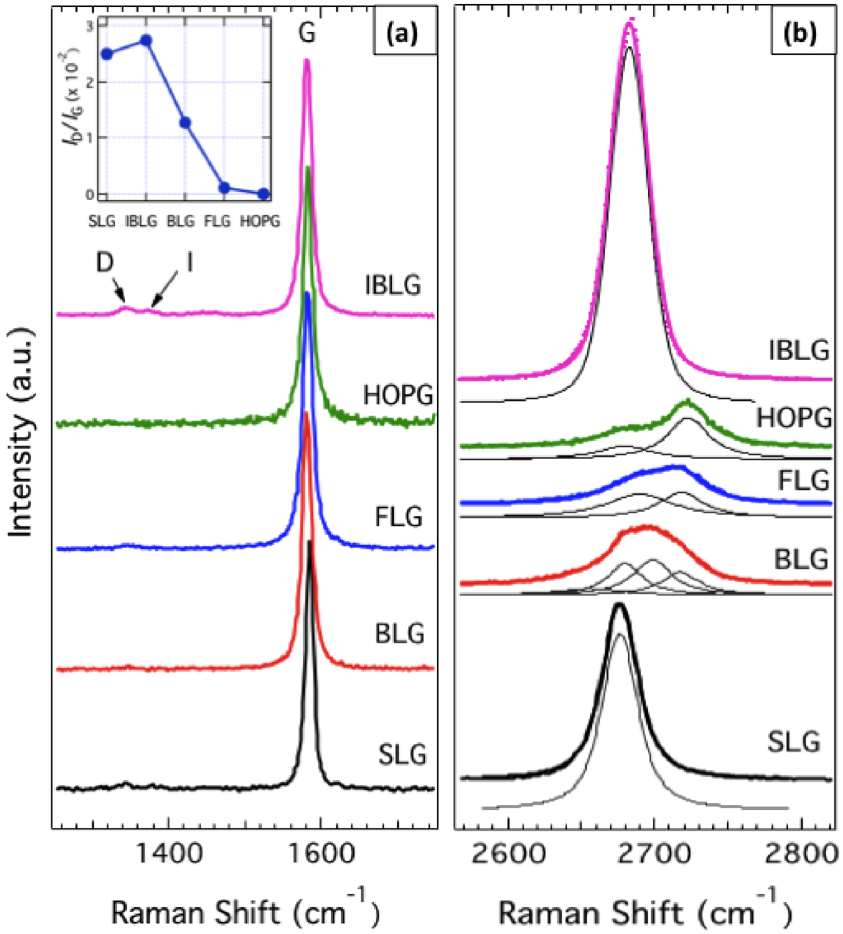

Figure 4.3.1: (a) Raman spectra in the D and G band region,. (b) The second order G’ band region from single and multiple layer graphene samples. The inset in (a) shows the

I_D/I_G ratios for the various samples. All spectra are normalized with respect to the G band intensity and offset for clarity.

Figure 4.3.2a shows peaks in the region between the G and G' bands (1650 – 2300 cm^{-1}), which are typically much lower in intensity than the other peaks in the Raman spectra of graphene. The strong dependence of peak frequencies and intensities of these modes on the number of layers can be observed clearly in Fig. 4.3.2a. The lowest frequency peak in Fig. 4.3.2a appearing at ~1750 cm^{-1} is a double peak feature called the M band, which is an overtone of the out-of-plane o-TO phonon and has been observed in graphite and single-walled nanotube (SWNT) samples [74, 75]. The M band, which is intensified by strong coupling between graphene layers, is suppressed for SLG and IBLG as observed previously [72]. In addition, the lower frequency peak in the M band (M^-) is downshifted by ~20 cm^{-1} in BLG compared to FLG or HOPG (vertical dashed line in Fig. 4.2.2a). The peak at ~1860 cm^{-1} in SLG has been assigned to a combination of the in-plane iTA phonon and the LO phonon and can be called the $iTALO^-$ mode [72, 74]. However, instead of a single peak as reported in previous studies [72, 74], we observe a two-peak structure for this mode. Furthermore, the intensity of both peaks clearly decreases with increasing layers of graphene. We also observe these peaks in SLG samples on other substrates such as mica and quartz, confirming that the peaks are intrinsic to graphene and are not a substrate effect. The third set of peaks in the range shown in Fig. 4.3.2a occur due to combinations between the iTO + LA (lower frequency peak) and LO + LA phonons (higher frequency peak) [72]. It has recently been shown that the higher frequency LOLA peak is more sensitive to defects and decreases in intensity upon heat treatment [76, 77]. Finally, a previously unidentified peak at ~2220 cm^{-1} is observed in all graphene samples. Its origin is discussed below.

Two novel features can be observed from Fig. 4.3.2a. A new mode appears at ~1880 cm^{-1} (iTALO^{+}) as a shoulder on the higher frequency side of the iTALO^{-} peak in SLG. In addition, this new mode is greatly suppressed in IBLG in contrast with SLG and BLG, indicating that it is very sensitive to the stacking order of graphene layers. As such, we refer to the absence of this mode as an indicator for IBLG. We tentatively assign this peak to a combination of the oTO and LO phonons around the K point of the graphene Billouin zone, as explained below. The second new feature in Fig. 4.3.2a is the appearance of a peak at ~2220 cm^{-1} that has not been seen previously in graphene samples. This peak has, however, been observed in single-walled carbon nanotubes (SWNTs)[20] and is tentatively assigned as combination of the iTA and iTO phonons around the K point in the Billouin zone of graphene.

Fig. 4.3.2b plots the frequencies of all the combination modes between 1650–2300 cm^{-1} (iTALO^{-}, iTALO^{+}, iTOLA, LOLA, and iTOTA modes) for graphene samples with increasing layers. The iTALO^{-} mode is absent for HOPG. The peaks involving the LO phonon, namely the iTALO^{-}, iTALO^{+}, and LOLA peaks, increase in frequency due to increasing layers, while the iTOLA peak at ~1970 cm^{-1} remains more or less at the same position. In addition, the frequency of the iTOTA mode at ~2220 cm^{-1} (inset in Fig. 4.3.2b) is observed to decrease with increasing graphene layers. The frequency increases of the iTALO^{-} and iTALO^{+} modes indicate a high degree of sensitivity of these modes to the stacking order of graphene layers.

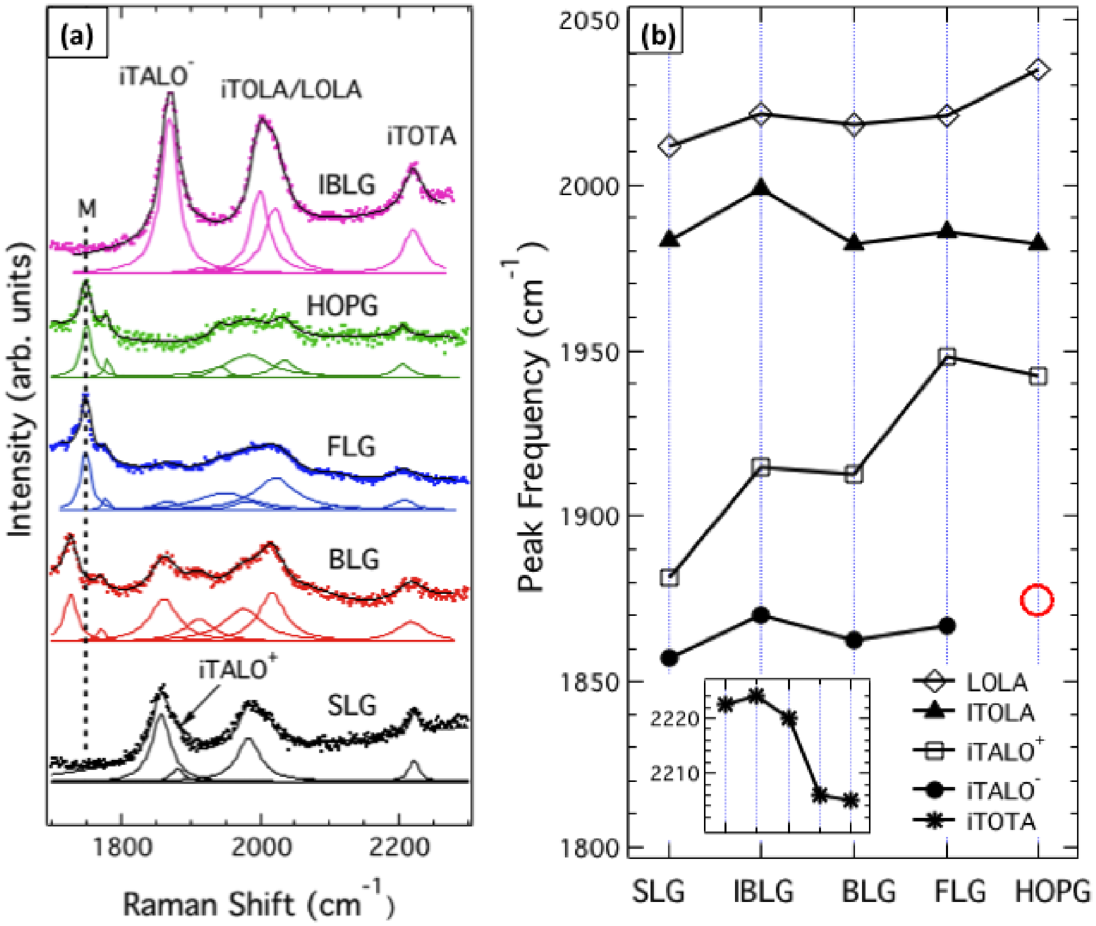

Figure 4.3.2: (a) Raman spectra between 1650 – 2300 cm^{-1} from graphene samples collected with E_{laser} = 2.33 eV. All spectra have been normalized by the G band intensity and fitted with Lorentzian peaks. (b) Change in peak frequency of the various second order double resonance Raman modes (see section 4.3 discussion of all the peak assignments) due to increasing layers in graphene samples. The absence of the iTALO peak at ~1860 cm^{-1} in HOPG is indicated by the hollow (red) circle. Inset in (b): Position of the iTOTA peak for the various samples. The *x*-axis is the same as in (b).

All the combination modes in IBLG are further upshifted in frequency compared to both SLG and BLG. This is different from what is observed for AB-stacked graphene layers, suggesting an additional mechanism such as compressive strain between the two incommensurate graphene layers that causes an added stiffening of all the combination modes in IBLG compared to SLG and AB-stacked graphene layers. We confirmed that the relative shift of all the combination modes is maintained between the unfolded SLG and IBLG regions on the same sample, suggesting that the results shown in Fig. 4.3.2b are not due to variations in the electronic doping of different samples.

Interestingly, we find that all the combination mode frequencies exhibit an almost linear dependence on $1/n$ according to the following relation: $\omega(n) = \omega(\infty) + \beta/n$, where n is the number of graphene layers, and β is a constant (Fig.4.3.3). Such a linear dependence on $1/n$ has been observed previously for the G band phonons in exfoliated grapheme [68]. As seen in Fig. 4.3.3, the values of β for the iTALO$^-$ and LOLA are comparable to shifts caused by the van der Waals interactions (~12-13 cm^{-1}) in the radial breathing modes of bundled SWNTs [78, 79], suggesting that these modes are mostly affected by layer stacking rather than changes in the electronic band structure. On the other hand, the high β value for the iTALO$^+$ mode, which occurs due to a higher frequency shift with increasing graphene layers suggests that this mode may be more sensitive to the electronic structure of graphene, similar to the 2D band.

The dispersion of the combination modes discussed above versus laser energy is shown in Fig. 4.3.4. The iTOLA and LOLA modes upshift with laser energy by 204 cm^{-1}/eV and

223 cm^{-1}/eV respectively. These dispersions are similar to the peak dispersions of the iTOLA and LOLA modes in graphite and SWNTs [75, 77, 80]. In addition, the dispersion of the $iTALO^-$ mode is ~ 140 cm^{-1}/eV, similar to the value reported recently by Cong *et al.,*[14] while the dispersion of the $iTALO^+$ mode is a little higher (~150 cm^{-1} /eV). One could consider the two peaks around 1860 cm^{-1} to occur in a similar fashion as the M band at ~1750 cm^{-1}, which also consists of two peaks. The two peak structure of the M band has been explained in the context of double resonance Raman scattering (see chapter 1) with the lower frequency (M^-) peak attributed to scattering by a phonon with a momentum double that of the scattered electron ($q \approx 2k$), and the higher frequency (M^+) peak due to scattering by a phonon with near zero momentum ($q \approx 0$) [75]. This explains the fact that the M^+ peak does not disperse with laser energy while the M^- peak downshifts with increasing laser energy. However, both the $iTALO^-$ and $iTALO^+$ modes are observed to shift with laser energy with similar dispersions, ruling out the $q \approx 0$ phonon within the framework of double resonance theory. Furthermore, the relative intensity between the $iTALO^-$ and $iTALO^+$ modes changes dramatically for IBLG. The inset in Fig. 4.3.4 shows the ratio of peak intensities of the $iTALO^+$ and $iTALO^-$ (I_{iTALO+}/I_{iTALO-}) modes plotted for SLG, IBLG, BLG and FLG. An obvious decrease in the ratio for IBLG can be observed, suggesting that the $iTALO^+$ peak is quite sensitive to the interlayer interaction of individual graphene layers.

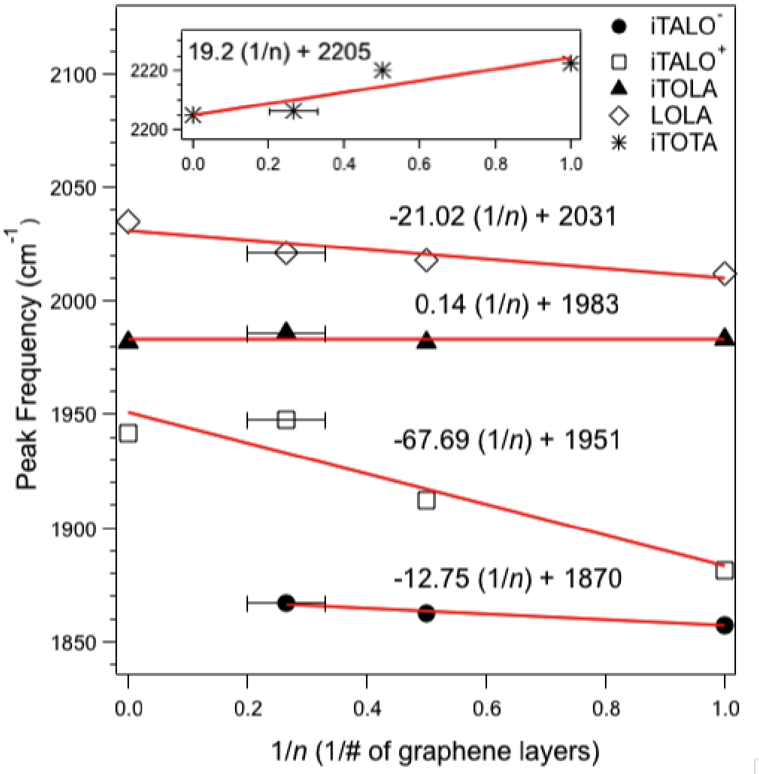

Figure 4.3.3: The peak frequencies of various combination modes (see text for more details) as a function of inverse number of graphene layers (*1/n*). The solid lines represent the results of a least squares fit to the data. The error bars for the FLG samples were obtained from AFM measurements which confirmed the presence of 3-5 graphene layers.

A recent theoretical study predicted the absence of infrared modes in non AB-stacked grapheme [81]. The suppression of the iTALO$^+$ mode in IBLG could therefore be due to this lack of the infrared active oTO phonon. In fact, for the iTALO$^+$ peak in HOPG at ~ 1940 cm^{-1} (see Fig. 4.3.2b), a good agreement can be found for a combination of the oTO (~620 cm^{-1}) and LO modes (~1350 cm^{-1}) around the K point of the graphene Brillouin zone [66]. In addition, for the excitation ranges used in this study, the dispersions of the oTO and LO modes around the K point are both positive and could account for the ~150 cm^{-1}/eV dispersion of the $iTALO^+$ mode. Based on the above arguments we tentatively assign the $iTALO^+$ mode as a combination of the oTO and LO phonons around the K point of the graphene Brillouin zone. It is worth mentioning that second

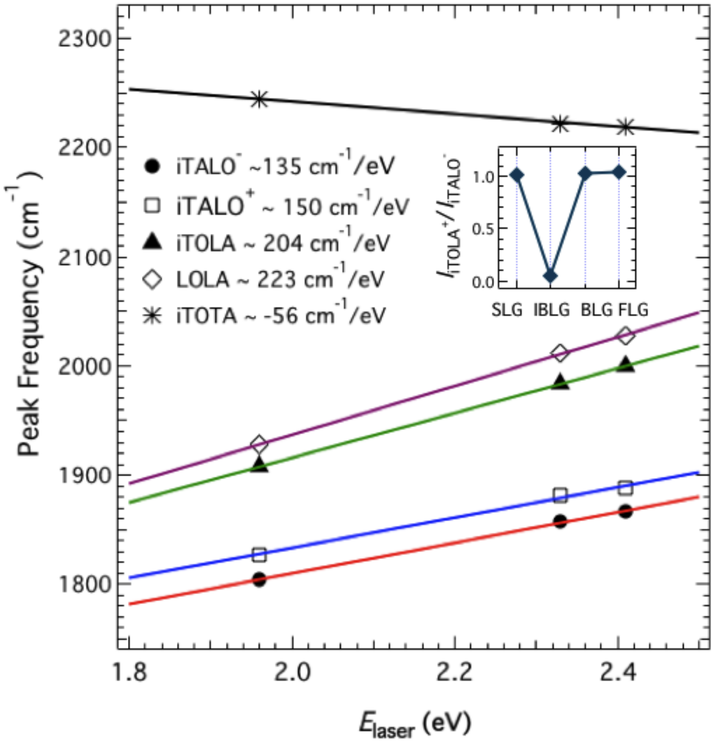

Fig. 4.3.4: Dispersion of the combination modes between 1650– 2300 cm^{-1} versus laser energy in SLG. Inset: Ratio of peak intensities of the $iTALO^+$ mode with respect to the $iTALO^-$ mode for SLG, BLG, IBLG and FLG samples.

order modes with large dispersions (such as the iTOLA and LOLA modes) typically occur due to the combination of an acoustic and optical phonon, yet these other modes do not fit our data. Further theoretical and experimental studies are needed to understand why this particular combination mode appears for single layer and AB-stacked graphene but not IBLG.

The second previously unidentified mode in SLG at ~2220 cm^{-1} (for E_{laser} = 2.33 eV) has a negative dispersion with laser energy and the peak frequency downshifts with increasing excitation energy by ~ -56 cm^{-1}/eV (Fig. 4.3.4). A peak at ~2200 cm^{-1} has been observed in SWNTs but was left unassigned [78]. Moreover, as shown in Fig. 4.3.2b, the peak at ~2200 cm^{-1} downshifts in frequency with increasing graphene layers in contrast to the other modes involving the LO phonon. The iTA branch around the K point has a negative dispersion and peaks around 1100 cm^{-1} corresponding to the iTA phonon have been observed in graphite whiskers [74] and carbon nanotubes [53]. However, the dispersion of the iTA branch is ~ -75–100 cm^{-1}/eV [82], which implies that the dispersion of its overtone would be twice as much. This makes it unlikely for the 2220 cm^{-1} peak to be the overtone of the iTA phonon. On the other hand, a combination of the iTA phonon (at ~940 cm^{-1}) and iTO phonon (~1350 cm^{-1}) around the K point could account the 2200 cm^{-1} mode. The iTO phonon branch has a positive dispersion (~50 cm^{-1}/eV) while the iTA branch has slight negative dispersion (~-20 cm^{-1}/eV) around the K point of the graphene Brillouin zone [66]. However, there is limited experimental data available for the iTA phonon branch around the K point of graphene (or graphite) [66] and this ambiguity could account for the -56 cm^{-1}/eV dispersion observed for the 2220 cm^{-1} combination mode. We thus assign this mode as a combination of the iTA and iTO phonon (hence the name iTOTA) around the K point of the graphene Brillouin zone. All the combination modes discussed above are listed for SLG and HOPG in Table 4.3.1. Also included in Table 4.3.1 are the phonon modes involved in the double resonance Raman scattering process for these combination modes.

In summary, we have observed changes in various combination modes in the Raman spectra of graphene that depend on the number and stacking of layers. The overtone of the infrared active oTO phonon, also called the M band disappears for SLG and non AB-stacked bilayer samples, indicating that the M band is strongly dependent on stacking order of graphene layers. In addition, the lower frequency peak within the M band (M^- peak) downshifts by ~20 cm^{-1} for BLG compared to FLG and HOPG. A peak at ~ 1860 cm^{-1} is attributed to iTA + LO phonons, and its intensity is observed to decrease with increasing graphene layers. Moreover, the iTALO band can be deconvoluted into two peaks, with similar dispersions versus laser energy. The higher frequency peak at ~1880 cm^{-1} has a similar dispersion as the iTALO band and shows a strong dependence on stacking order of graphene layers. This peak is assigned to a combination of the oTO and LO phonons around the K point in the graphene Brillouin zone. A peak at ~2200 cm^{-1} is observed for all graphene samples and is assigned to a combination of the iTA and iTO phonons around the K point. The peak frequencies of all the combination modes involving the LO phonon are observed to increase linearly with increasing graphene layers, indicating a strong coupling of the LO phonon between graphene layers.

Peak Frequencies (cm^{-1}) **SLG (HOPG)**	**Mode**	**Phonons**	**Dispersion (cm^{-1}/eV)**	**Experimental Observation**
(1725)	M	2oTO	0	Refs. 16, 17
(1750)	M	2oTO	~ -10	Refs. 16, 17
1857	$iTALO^-$	iTA + LO	~ 135	This work and Ref. 14
1880 (1940)	$iTALO^+$	oTO + LO	~ 150	This work
1983 (1982)	iTOLA	LA + iTO	~ 204	Refs. 16, 18, 19, 22
2012 (2035)	LOLA	LA + LO	~ 223	Refs. 16, 18, 19, 22
2222 (2206)	iTOTA	iTA + iTO	~ -56	This work

Table 4.3.1: Peak frequencies and assigned labels for experimentally observed double resonance Raman modes. The table also lists the peak dispersions versus laser energies for various combination modes for SLG and HOPG.

4.4 Effects of crystallite size and defects on the optical properties of graphene

The *G'*-band present at ~2700 cm^{-1} in the Raman spectrum of graphene exhibits a characteristic lineshape depending on the number of layers. For example, the *G'*- band in SLG can be fit to a single Lorentzian peak and its integrated area ($I_{G'}$) is higher than that of the *G*-band located at ~1585 cm^{-1}[66]. As the number of layers increase (from SLG to HOPG), the *G'*-band evolves into a two-peak structure with a concomitant decrease in $I_{G'}/I_G$, where. $I_{G'}$ and I_G represent the integrated intensities of the *G'* and *G* bands, respectively. The Raman spectrum of graphene or nanographite exhibits an additional feature at ~1350 cm^{-1} (known as the *D*-band) due to the presence of structural disorder such as, impurities, edges, and finite size effects that breaks the translational symmetry. The ratio I_D/I_G has also been widely used in the literature for determining the in-plane crystallite size (L_a) for polycrystalline graphite samples [2, 82, 83, 84].

Several fundamental properties of graphene have been discerned from studies using exfoliated single-grain graphene samples (see section 4.3) and the effects of layer stacking (crystallinity perpendicular to the graphene plane) on the optical properties of graphene, such as Raman scattering and linear absorption, are well understood. Recently, the chemical vapor deposition (CVD) technique has gained popularity since large area high-quality *polycrystalline* graphene on metallic substrates can be readily prepared using this method. It is well known that L_a [2, 8, 83-85] significantly influences many physical properties of polycrystalline graphitic materials, and thus the presence of grain boundaries in the CVD grown samples is expected to considerably modify the electronic and optical properties of graphene. Moreover, there are only a few studies which describe the effects of in-plane crystallinity (L_a) on the optical properties of grapheme [86]. Dawlaty *et al.* [86] found that higher values of L_a (or smaller crystal disorder) result in long-lived photogenerated carriers in graphene. Hashimoto *et al.* [84] and Osipov *et al.* [85] observed changes in the plasmon energy of graphite and nanographite structures due to varying L_a. In this article, we present the effects of disorder on the linear and non-linear optical properties of CVD grown graphene. We find that the pi-plasmon energy and the excitonic lineshape in the optical absorption spectra of polycrystalline graphene exhibit significant changes as a function of L_a. In addition, saturable absorption properties of these samples, probed using the open aperture Z-scan measurements, indicate that the saturation intensity varies linearly as function of L_a.

Micro-Raman spectroscopy: As evident in Fig. 4.4.1a, all CVD grown graphene samples exhibit strong *D*- and *G*-bands. The *D*-band observed at ~1350 cm^{-1} confirms the polycrystalline nature of our samples. The lineshape of the *G'*-band for the 1 sccm samples is consistent with the Raman spectrum of BLG. Previously, Park *et al.* [87] argued that the origin of the *G'*-band in BLG (tri-layer graphene or TLG) can be traced to four (nine) possible optical Raman processes. However, only three (five) of such optical processes are non-degenerate. Thus, the Raman spectrum for 1 sccm samples was fitted to 3 Lorentzians consistent with the established peak widths (or phonon life times) for BLG. The lineshape of the *G'*-band of 2, 4 and 8 sccm samples consists of 3 or more peaks and suggests the existence of 3-5 graphene layers (or FLG).

Electron microscopy: Figures 4.4.2a & b show typical TEM images of our samples discussed in Fig. 4.4.1. The hexagonal electron diffraction pattern along with the TEM images confirms the presence of polycrystalline nature of our samples. Previously, Huang *et al*. [88] observed varying mean grain size for graphene grown on different Cu foils suggesting that the substrate grain size distribution influences the in-plane crystallinity of CVD grown graphene. In order to further understand the correlation between the graphene crystallinity and the Cu grain size, and the ensuing optical properties described below, we used Raman spectroscopy to obtain L_a values for graphene from Cancado's formula (see chapter 1).

$$L_a\,(nm) = 2.4 \times 10^{-10}\, \lambda^4\, (I_G/I_D)$$

where λ is the excitation wavelength.

Although the Cu grains present in the foil exhibited arbitrary sizes and shapes, the size and distribution of Cu grains was evaluated by approximating the grain size to the square root of the grain area obtained from the optical images using ImageJ software. Interestingly, we find a linear dependence of L_a on the Cu substrate grain size (Fig. 4.4.3a), consistent with a previously observed trend of large crystalline metallic substrates favoring larger graphene crystallites. Furthermore, we find that the growth of graphene with lower defects (higher L_a) is favored above a critical Cu grain size of ~40 μm) confirming that the crystallinity of Cu substrate is a crucial factor in the graphene synthesis.

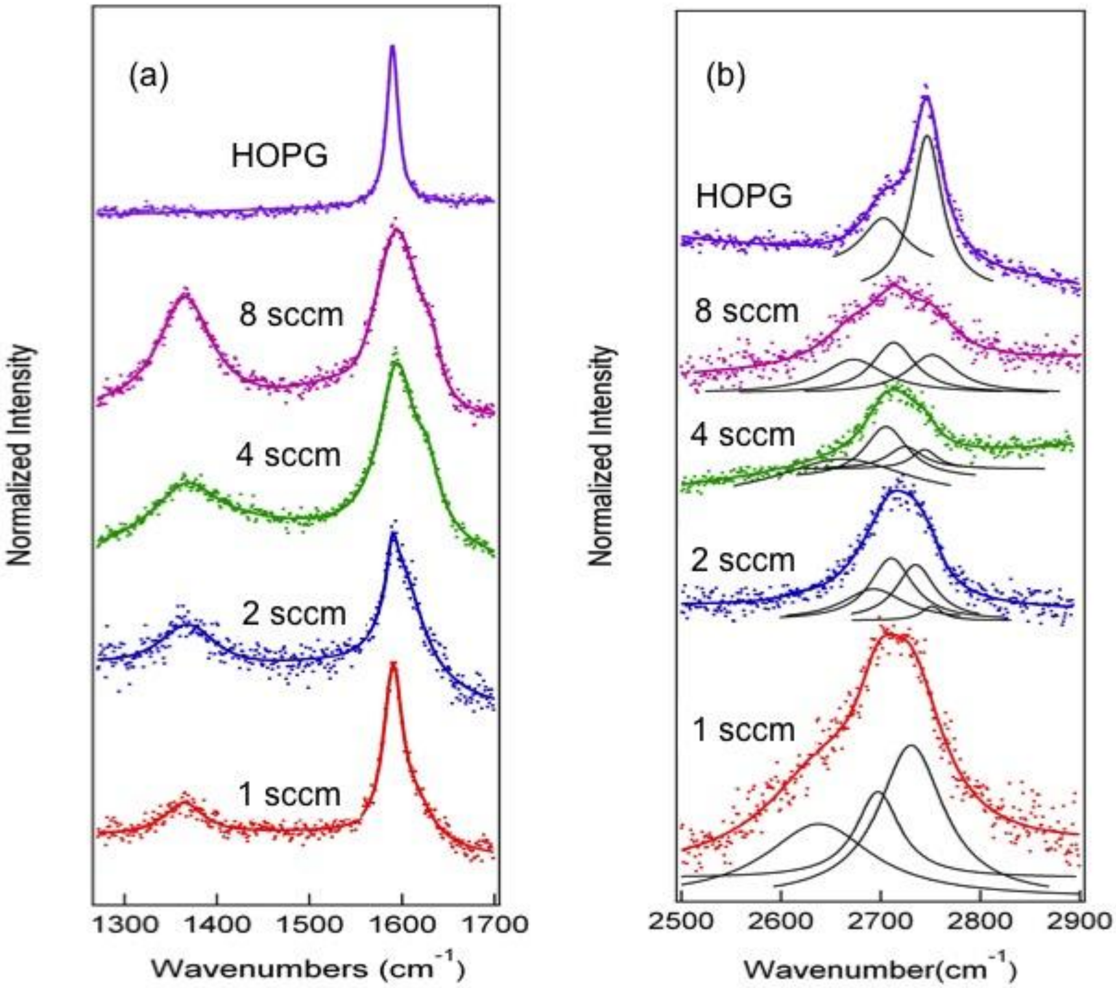

Figure 4.4.1: Room temperature Raman spectra of as-prepared CVD grown graphene samples showing the *D*- and *G*- bands (a) and the *G'* band (b). The methane flow rates are indicated in both panels. The multi-peak fitting analysis suggests the presence of BLG in 1 sccm samples and FLG in 2, 4 and 8 sccm samples. The top most spectra correspond to the the Raman spectra of HOPG. As expected, the *D* Raman band in HOPG is absent due to its high crystalline order.

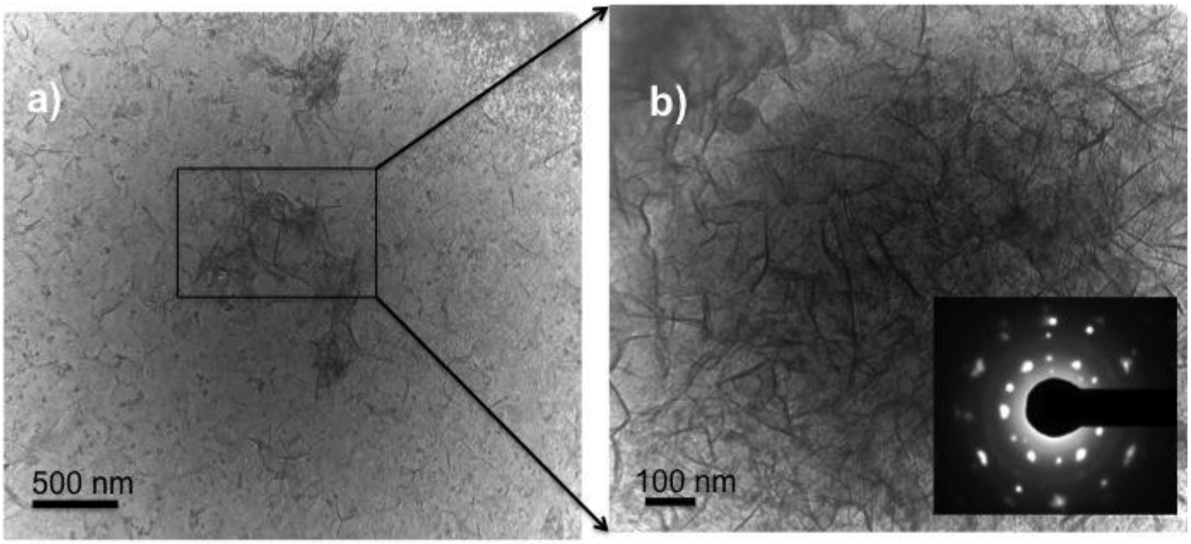

Figure 4.4.2: (a) Typical transmission electron microscope images of CVD grown poly-crystalline graphene. (b) A magnified view of the boxed area in (a). The inset shows hexagonal diffraction pattern obtained from the graphene samples.

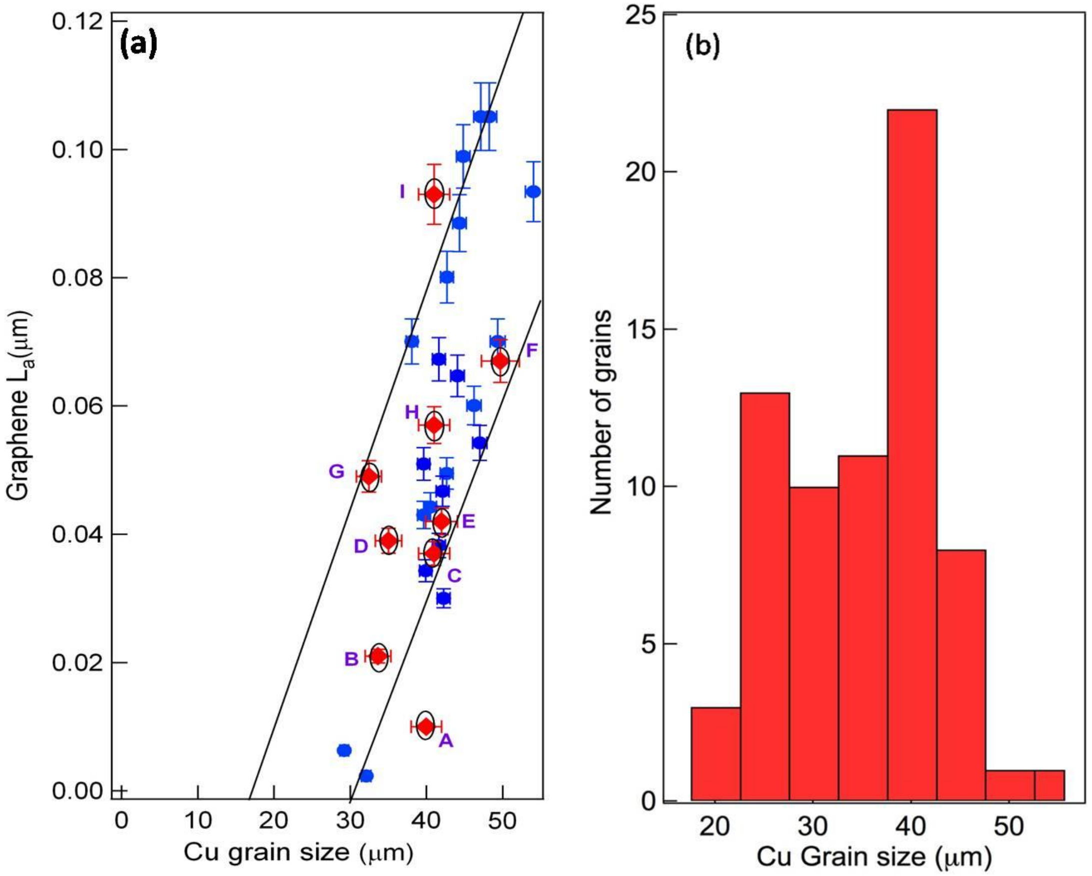

Figure 4.4.3: (a) A map of graphene crystallite size L_a (obtained from micro-Raman spectroscopy) as a function of Cu grain size present in the copper foils used in the CVD synthesis of graphene. The L_a values were obtained by averaging the Raman spectra at 10 differentspots. Highlighted areas show the range of dominant Cu grain sizes. The top right hand corner of the plot indicates that high quality graphene (low defects) is obtained when the Cu grain size exceeds ~40 μm. (b) A histogram showing the population of various Cu grain sizes.

Optical absorption studies:

We measured the optical absorption of six different samples (indicated as A –F in Fig. 4.4.3a and Fig. 4.4.4) with different L_a to study the effect of crystalline order on the saddle point exciton energy in graphene. The UV-visible absorption spectrum of graphene exhibits a pronounced resonance feature at ~ 260 nm which arises from the electronic transitions near the *M*-point (from *pi* to *pi** orbital) in the Brillouin zone of graphene [90-92]. The energy dispersion near the *M*-point is locally flat (saddle point) and thus leads to a *discrete* van Hove singularity (vHS) in the graphene density of states. The transition occurring slightly below the *M*-point feature (or the vHS in the density of states) is also known as *pi*-plasmon in graphite and carbon nanotubes [84, 85] and has also been observed in grapheme [89-91]. Specifically, Mak *et al.* [90] observed that the optical conductivity of exfoliated graphene deviated significantly from the predicted universal value (~2.3%) within an independent-particle model. However, Mak *et al*. observed only a very slight variation of excitonic resonance with layer thickness in few-layer graphene (FLG). In addition, the *pi*-plasmon resonance peak was also found to exhibit asymmetric Fano line shape (*Eq. 4.4.1*) due to the interaction of the discrete vHS with continuum states near the *K*-point [90, 91],

$$I(E) = I_o \frac{\left(1 + \frac{E - E_o}{q\Gamma}\right)^2}{\left(1 + \left(\frac{E - E_o}{\Gamma}\right)^2\right)} \qquad (\ 4.4.1\ )$$

In the above equation, *I* is the intensity, E_o is the resonance energy, Γ is half-width of the resonance peak and *1/q* is the Fano interaction parameter.

The pi-plasmon energy of graphene is given by [84]

$$h\omega_{pi} = \frac{h\omega_p}{2}\left(1 - \frac{4\pi^2 m a^2 \gamma_o}{3h^2}\left(1 + \frac{\gamma_1 c^2}{4a^2\gamma_o}\right)\right) \qquad (4.4.2)$$

where $h\omega_p = \sqrt{\frac{4\pi n e^2}{m}}$.

a, *c* are graphene lattice parameters, *m* is electron rest mass, *n* is the carrier concentration and *h* is Planck’s constant, γ_0 and γ_1 are overlap integrals. Since the pi-plasmon peak results from the p_z orbitals present in the hexagonal network of carbon atoms, the in-plane defect density (hence L_a) will influence the plasmon energy more significantly than the layer stacking in graphene. We find that the pi-plasmon wavelength of our graphene samples varies inversely as a function of L_a (Fig. 4.4.5), similar in behavior to that observed in graphite [84, 85].

Following Hashimoto *et al.* [84] we explain the observed changes in the pi-plasmon energy of graphene in terms of a change in the carrier concentration (*n*) due to varying defect density in our polycrystalline graphene samples (Eq. 4.4.2). As described in Fig. 4, the peak ~260 nm exhibits a Fano line shape (Eq. 4.4.1) due to the interaction with the Dirac continuum states in the vicinity of the K point. We show that the parameter *q* (Eq. 4.4.1) depends on L_a (inset of Fig. 4.4.5); suggesting that the crystallite size influences the interaction between the *pi*-plasmon and the continuum states in graphene. Thus, we conclude the observed upshift in the *pi*-plamson energy (or the downshift in wavelength) to changes in the interaction (indicated by *q*) between the discrete vHS and Dirac continuum states with varying L_a. Further, we find that the pi-plasmon wavelength in our data follows an empirical relationship $\lambda_\pi = 250.5nm + {89.5nm^2}/{L_a}$.

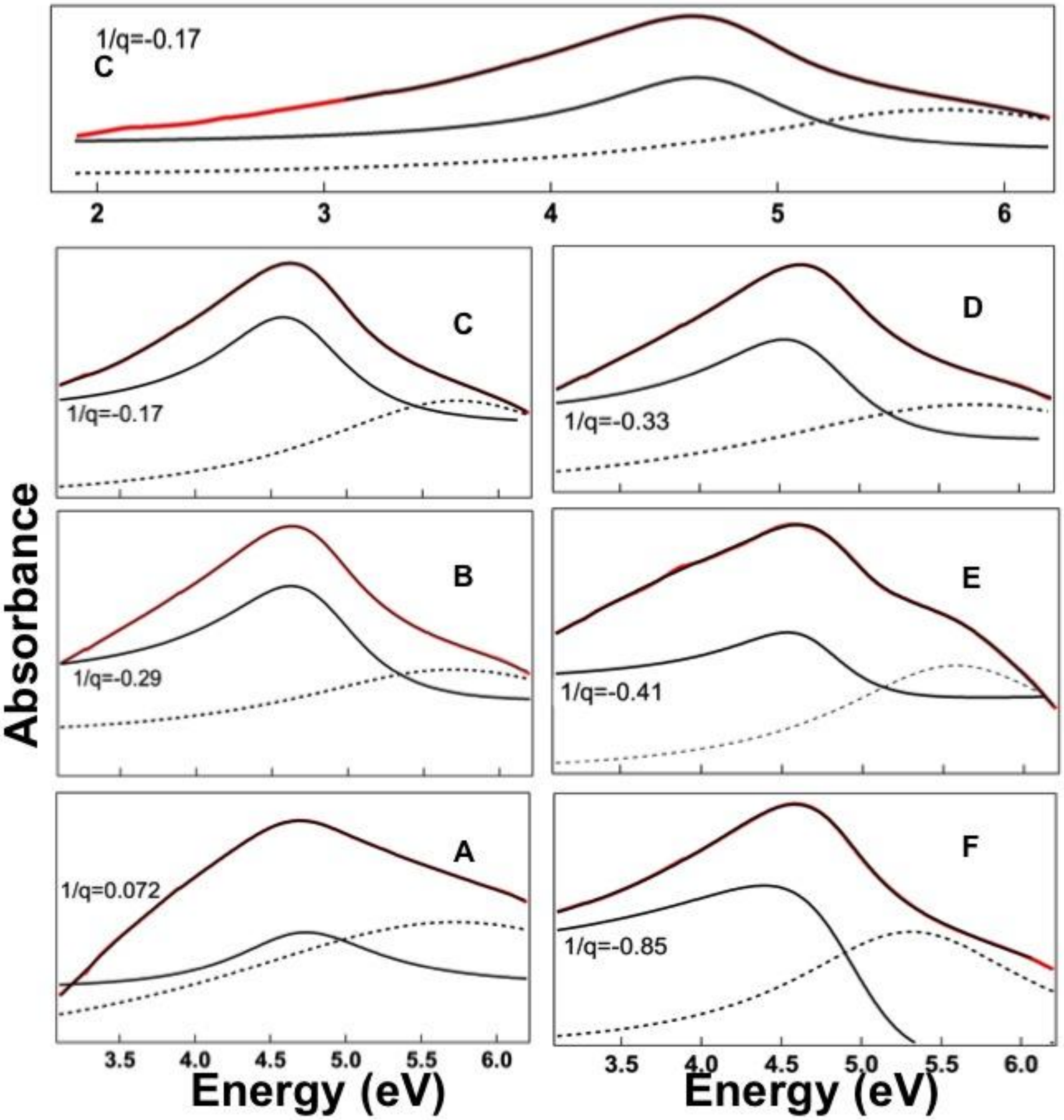

Figure 4.4.4: UV-Visible absorption spectra of graphene samples with different crystallite sizes (for samples A-F indicated in Fig, 4.4.3a). Clearly, the peak ~260 nm in the top panel shows the presence of asymmetric Fano lineshape (see text for details). The small Lorentzian (shown in dashed lines) slightly below (above) the plasmon wavelength (energy) is the vHS in the density of states.

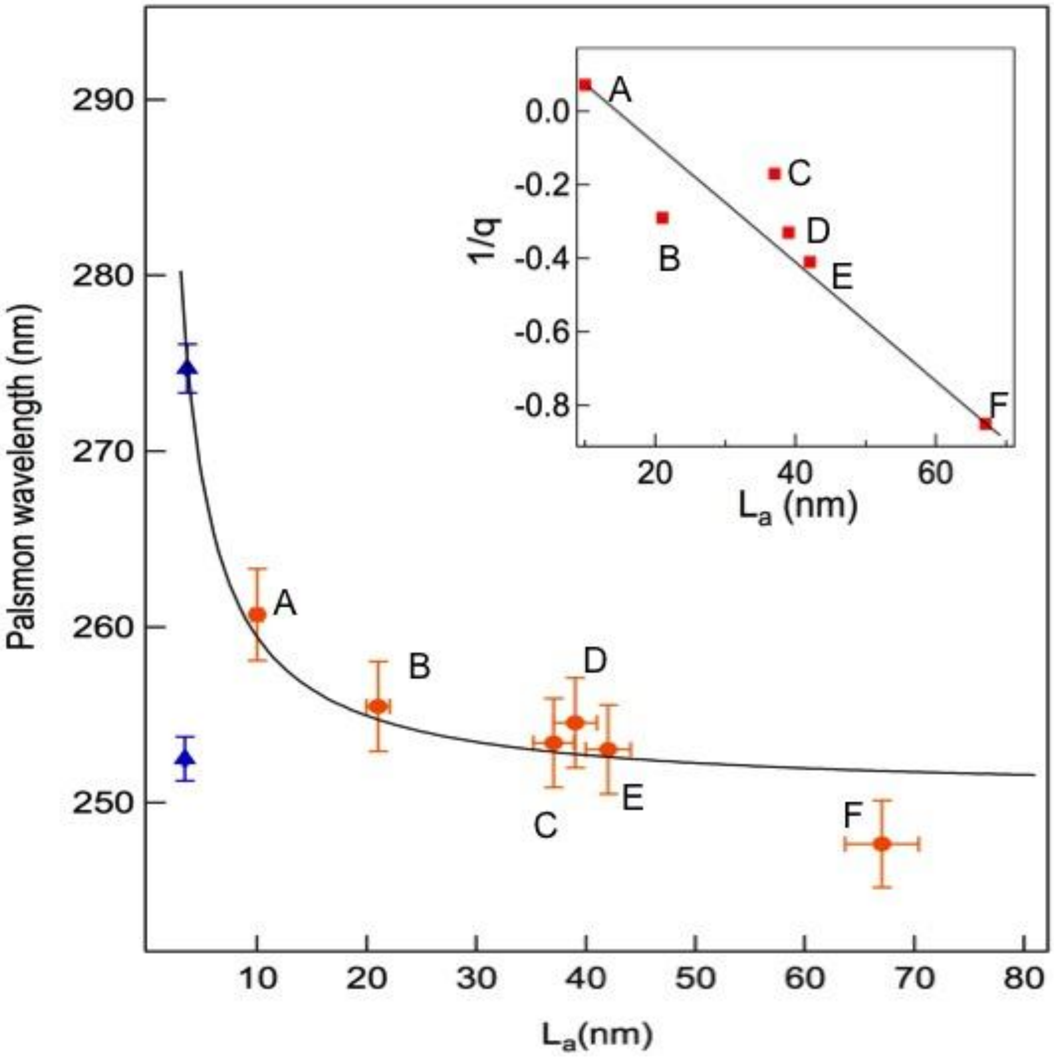

Figure 4.4.5: Dependence of the pi-plasmon wavelength on L_a. The curve serves as a guide to the eye. The data points in blue are the plasmon energies for nanographite obtained from Ref. 85. The inset shows the variation of interaction parameter as a function of crystallite size.

Non-linear optical studies: In this final section, we address the effect of L_a on the non-linear optical properties. Figure 4.4.6 shows the Z-scan data obtained for the samples G, H and I (shown in Fig. 4.4.3) with ~65% linear transmittance.

Irrespective of the excitation energy used in the experiment, an increase in the normalized transmittance ($\Delta T/T$) is evident as the samples approach $z = 0$; confirming the presence of saturable absorption in all three samples. It is important to note that in the ns regime, ΔT strongly depends on the excited state population density. Saturable absorption occurs when the absorption cross-section of the excited state is less than that of the ground state. When the samples are excited using a high intensity laser, the increase in the concentration of the photogenerated carriers results in a carrier density that is much larger than the intrinsic carrier density of graphene. Hence there is a rise in ΔT of the system when most of the electrons in the ground state are cyclically excited within the width of the incident laser pulse. The saturable absorption occurs since two photoexcited carriers cannot occupy the same state as governed by the Pauli's exclusion principle (known as Pauli blocking). The data in Fig. 4.4.6 suggests that the ns pulses excite carriers in graphene with relaxation times on the order of few hundred ps (in case of multiple absorption processes occurring within the incident pulse width) or ns.

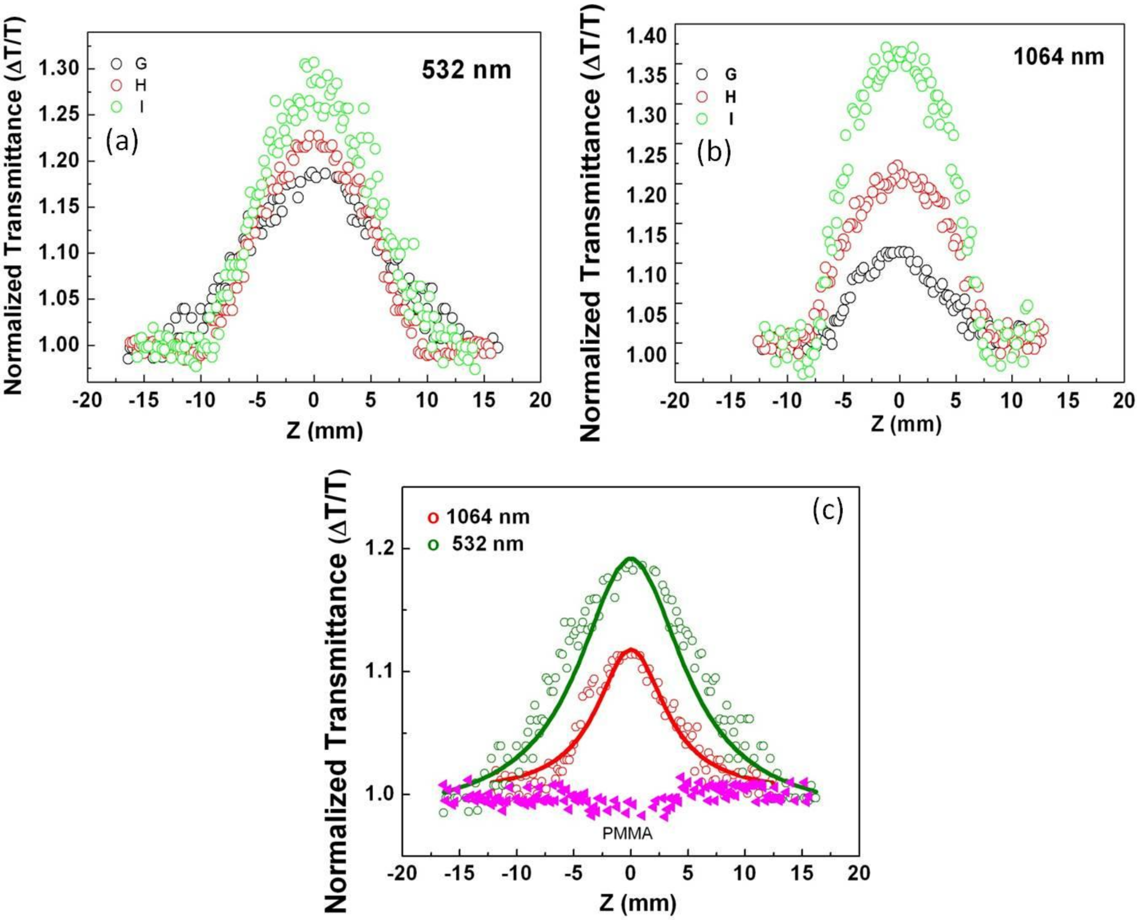

Figure 4.4.6: Open aperture *Z*-scan data obtained for G, H and I samples using 20 μJ of 5 ns pulses of 532 nm (a) and 30 μJ 1064 nm (b). Numerical fits obtained from eqns.3 and 4 are shown (c). The bottom most spectrum in (c) corresponds to the *Z*-scan data for PMMA (using 532 nm excitation) which does not contribute significantly to the graphene spectrum.

It is noteworthy that the saturable absorption process is independent of excitation energy since the energy dispersion of graphene is linear in the vicinity of the K point (i.e., any level in the valence band may be coupled to an appropriate level in the conduction band by the incident photon). Importantly, as explained below, the increase in normalized ΔT is sensitive to the number of graphene layers present in the sample, L_a and the excitation wavelength used in the experiment.

In order to identify the exact nature of the nonlinearity, the *Z*-scan data was fit to different nonlinear transmission equations 4.4.3 & 4.4.4 (Fig. 4.4.6c). Our analyses suggest two possible origins for the observed nonlinearity in the nanosecond excitation regime: (i) a strong saturation of the ground state absorption and (ii) weak two photon absorption (2PA). Therefore, an effective nonlinear absorption coefficient $\alpha(I)$, given by

$$\alpha(I) = \frac{\alpha_0}{1+\frac{I}{I_s}} + \beta I \qquad (4.4.3)$$

was considered, where α_0 is the unsaturated linear absorption coefficient at the excitation wavelength, I is the input laser intensity, I_s is the saturation intensity (intensity at which the linear absorption drops to half its original value) and β is the effective 2PA coefficient. The transmitted intensity for a given input fluence is calculated by numerically solving the propagation equation

$$\frac{dI}{dz'} = -\left[\left(\frac{\alpha_o}{1+ {}^{I}\!/_{I_s}}\right) + \beta I\right] I \qquad (4.4.4)$$

Here z' indicates the propagation distance within the sample. The nonlinear parameters β and I_s are determined from the best-fit analysis of the experimental data.

Fig. 4.4.7 shows the variation of the effective 2PA coefficient (β) at 532 nm as a function of the $I_{G'}/I_G$. Clearly, β shows a small change as a function of $I_{G'}/I_G$ indicating that the layer stacking does not significantly affect the 2PA coefficient which can be rationalized as follows. It is well known that the linear absorption in graphene is 2.3% for a single layer irrespective of the incident energy. Thus, it is reasonable to expect that the transition probability for the carriers does not change drastically for the samples used in this study.

On the other hand, the saturation intensity (I_s) decreases considerably with a decrease in $I_{G'}/I_G$ for both 532 and 1064 nm (Fig. 7b). In the case of saturation intensity, the effects of layer stacking are two-fold: (i) *Effect of excitation:* The longer wavelength at 1064 nm probes the carriers closer to the Fermi level when compared to 532 nm (Fig. 4.4.7a). Since the density of states is lower near the Fermi level, longer wavelength excitations result in lower values of I_s for a given number of layers (bottom 2 curves in Fig. 4.4.7b). (ii) *Effect of layer stacking:* As discussed in Ref. 92, the saturation carrier density (N) may be approximated for a continuous wave excitation using Eq. 4.4.5.

$$N = \alpha F\tau \big/ \hbar\omega \tag{4.4.5}$$

where τ is the recombination time, F is the input fluence and ω is the excitation frequency. Hence, for a given incident excitation and fluence, the saturation carrier density is determined solely by the recombination time. The recombination time depends upon the defect density in the given sample and may be correlated to the crystal coherence length (L). Dawlaty *et al.* [86] previously observed that for higher values of L_a (or smaller crystal disorder), the photogenerated carriers will have a longer recombination time. Thus, the saturation intensity is expected to vary linearly as a function of L_a. This behavior is observed in Fig. 4.4.7c indicating that the saturation intensity in our samples occurs due to different recombination times (or crystallite size).

In summary, we observed that the pi-plasmon energy of graphene shows renormalization effects due to Fano resonance near the M-point. The crystallite size strongly influences the plasmon energy via the interaction between discrete vHS and Dirac continuum. Furthermore, we showed that the layer stacking in graphene has no significant effects on the effective two-photon absorption coefficient. The saturation intensity, in the Z-scan experiments, was observed to vary both as a function of the incident energy, crystallite size indicating that it is sensitive to the changes in the defect density.

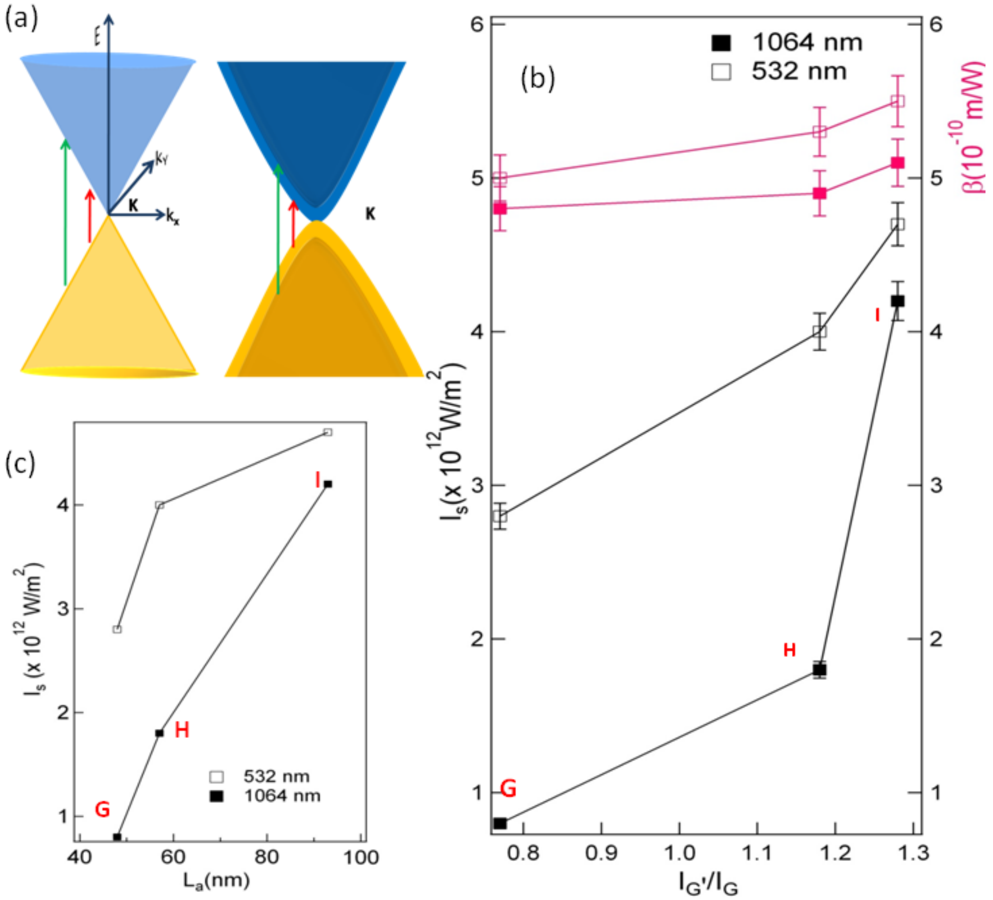

Figure 4.4.7: (a) The electronic energy band structure for SLG and BLG near the K-point. Energy varies nonlinearly with momentum as the layer stacking increases. In addition, the stacked layers result in sub-bands. (b) The variation of 2PA coefficient and saturation intensity (obtained using the fits described in Fig. 4.4.6c) as a function of $I_{G'}/I_G$. (c) The variation of saturation intensity as a function of L_a.

4.5 Curvature induced changes in the vibrational propeties of sub-nm SWNTs

Single-wall carbon nanotubes can be understood as folded sheets of single layer graphene. The quantum confinement in SWNTs, along the radial direction, causes van Hove singularities in their electronic structure. Since 1D nanotubes are rolled up from 2D sheets graphene, different subbands in the 1D reciprocal space of the nanotube can beextended into the 2D reciprocal space of a single graphene sheet as a set of parallel equidistant lines or cutting lines, as shown in Figure 4.5.1a. The method of constructing 1D electronic energy subbands by cutting the 2D electronic dispersion relations with these lines is known as the "zone-folding scheme" [cutting-lines]. Using the zone-folding scheme, one obtains the energy gap between the i^{th} vHS in SWNTs as $E_{ii} = 2i\gamma_0/\boldsymbol{a_{c\text{-}c}}$. Here, $\boldsymbol{\gamma_0}$ is the overlap integral and $a_{c\text{-}c}$ is the carbon bond length. Thus, in case of SWNTs, when laser excitation energy (E_{laser}) matches the energy gap (E_{ii}) between a pair of i^{th} vHS, one observes a resonance enhancement in the intensity of Raman-active modes such as the radial breathing mode (RBM) and the tangential stretching mode (G-band). Within the framework of the zone-folding scheme, most Raman features of SWNTs whose average diameter is > 1 nm have been well understood.

In this section, we present strong spectroscopic evidence, which suggests that curvature-induced effects lead to the activation of resonant intermediate frequency modes (IFMs) and new IR modes in highly curved sub nanometer SWNTs (sub-SWNTs). Previously, extremely *weak* IFMs (600-1100 cm^{-1}) and IR modes have been reported by several groups [93-98] in SWNTs with average diameter in the range of 1.5±0.3 and

1.0±0.3 nm. For example, Fantini *et al.* observed a step-like dispersion of the IFMs in semiconducting and metallic SWNTs and attributed its origin to the creation of an optic phonon and annihilation of an acoustic phonon. We find that the intensity of the IFMs can equal that of the RBMs in chemical vapor deposition (CVD) grown sub-nm SWNTs (Fig. 4.5.1a and b). Interestingly, we also observe S-like dispersion (Fig. 4.5.1c) for the G-band which is a result of curvature-induced perturbation of the electron-phonon (el-ph) interaction. We show that by taking into account the chiral dependence of $E_{ii,}$ (obtained from the tight-binding method [99]) and the overlap integral γ_o, the origin of the observed Raman features in sub-nm SWNTs can be understood. Furthermore, from our molecular dynamic simulations which employ a curvature-dependent force field [100], we find that (i) the G band dispersion consists of a family of lines with $2n + m$ = constant, where n and m are the standard chiral indices and (ii) the intensity of the IFMs decreases with decreasing nanotube curvature.

Sub-nm SWNT bundles were synthesized using a thermal CVD process with either mono (Co) or bimetallic (CoMn) catalysts as [101, 102]. Briefly, a CoMn-MCM-41 catalyst with 3% (or 1%) metal loading (Co:Mn in a molar ratio of 1:3 or 1:1) was synthesized by isomorphous substitution of metal in the silica framework. The MCM-41 wafer has an average pore diameter of about 3 nm as determined by nitrogen physisorption measurements. Sub-nm SWNT bundles were obtained from a thermal disproportionation of CO at 600 – 800 ^{o}C in a quartz tube reactor. The CoMn-MCM-41 catalyst (~200 mg) was reduced (flowing hydrogen, 700^{o}C, 1atm.) prior to the disproportionation of pure CO at 5-6 bar at desired synthesis temperature. For simplicity, we focus on

CVD-Co-Silica-550 sample which exhibited RBMs above 240 cm^{-1} confirming the presence of sub-nm SWNTs (average SWNT diameter ~ 0.75±0.1 nm) as shown in Fig. (4.5.1a). Sample ID CVD-Co-Silica-550 refers to the sub-nm SWNT bundles prepared at 550 ^{o}C using 3% Co catalyst supported on a grafted Silica wafer.

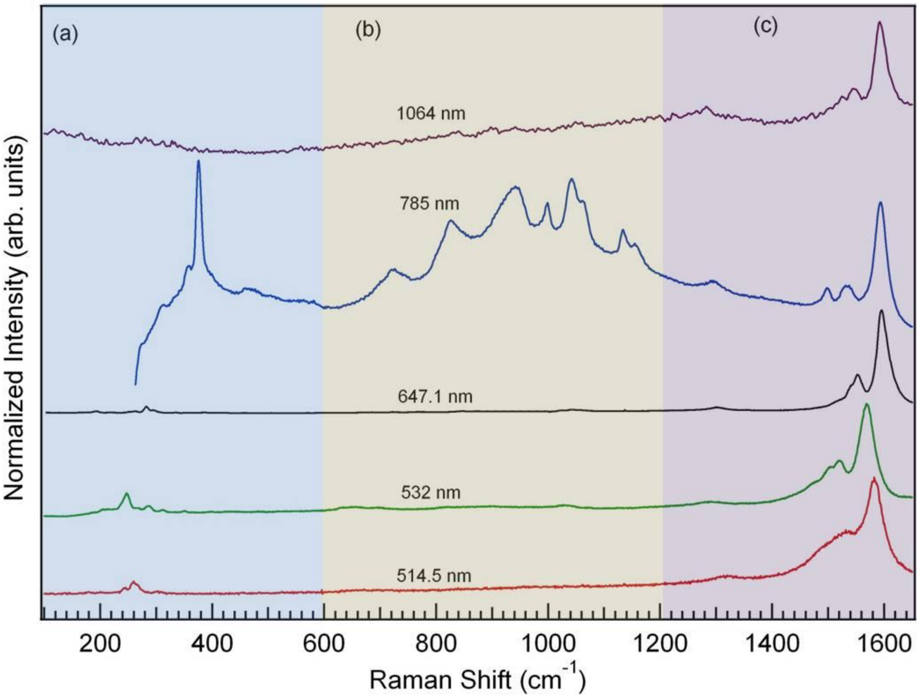

Figure 4.5.1: Raman spectra of CVD-Co-Silica-550 sub-nm SWNT samples. (a) Radial breathing modes at different excitation wavelengths. The 785 nm excitation is observed to be in resonance with 0.61 nm (ω_{RBM} ~ 374 cm^{-1}). (b) Intense intermediate frequency modes appear in the spectrum excited at 785 nm excitation. (c) S-like dispersion of the G-band (both TO and LO modes) is observed as the excitation wavelength was varied from 514.5 to 1064 nm.

The G-band frequency is known to be weakly dependent on the tube diameter. In contrast to such observations, the G-band frequency (both G^- and G^+ modes [103]) in Fig. 4.5.1c softens (downshifts) at first ($\lambda_{excitation}$ = 532 nm) and hardens (upshifts) with increasing excitation wavelength ($\lambda_{excitation}$ = 647 nm). With further increase in $\lambda_{excitation}$, it re-softens ($\lambda_{excitation}$ = 785 and 1064 nm) exhibiting an overall S-like dispersion. We relate this dispersion of the G-band to electron-phonon interaction and perturbation of the optical phonon energy due to the *high curvature* in sub-nm SWNTs (cf. Eq. 4.4.1). It is well known that the lineshape of the G-band deviates from a Lorentzian to a Breit-Wigner-Fano (BWF) lineshape in SWNT bundles due to charge transfer or the interaction of Raman-active phonons with the energy continuum near the Fermi energy, E_F [104, 105]. The BWF lineshape is described as in (4.4.1). The factor $1/q$ in Eq. 4.4.1 is a measure of the departure from a symmetric Lorentzian lineshape due to electron-phonon interaction, and Γ is the peak width [104]. Small tube diameters and curved bundles present in our samples can lead to strong electron-phonon coupling due to the broadening of the vHS [106], and an increase in the allowed phonon spectrum due to symmetry lowering [107]. Thus, the G-band in Fig. 4.5.1c obtained using various excitation wavelengths is fit to Eq. 4.4.1 with $1/q$ as the only fitting parameter. As shown in Fig 4.5.2a, the obtained $1/q$ values clearly mimic the S-like dispersion of the G-band mentioned above. Furthermore, it is interesting to note that the observed frequency shifts in the RBM track the G-band frequency shifts, indicating that the observed G-band intensity is from different population of tubes with dissimilar internal strains and metallicity, excited at each wavelength in the sample.

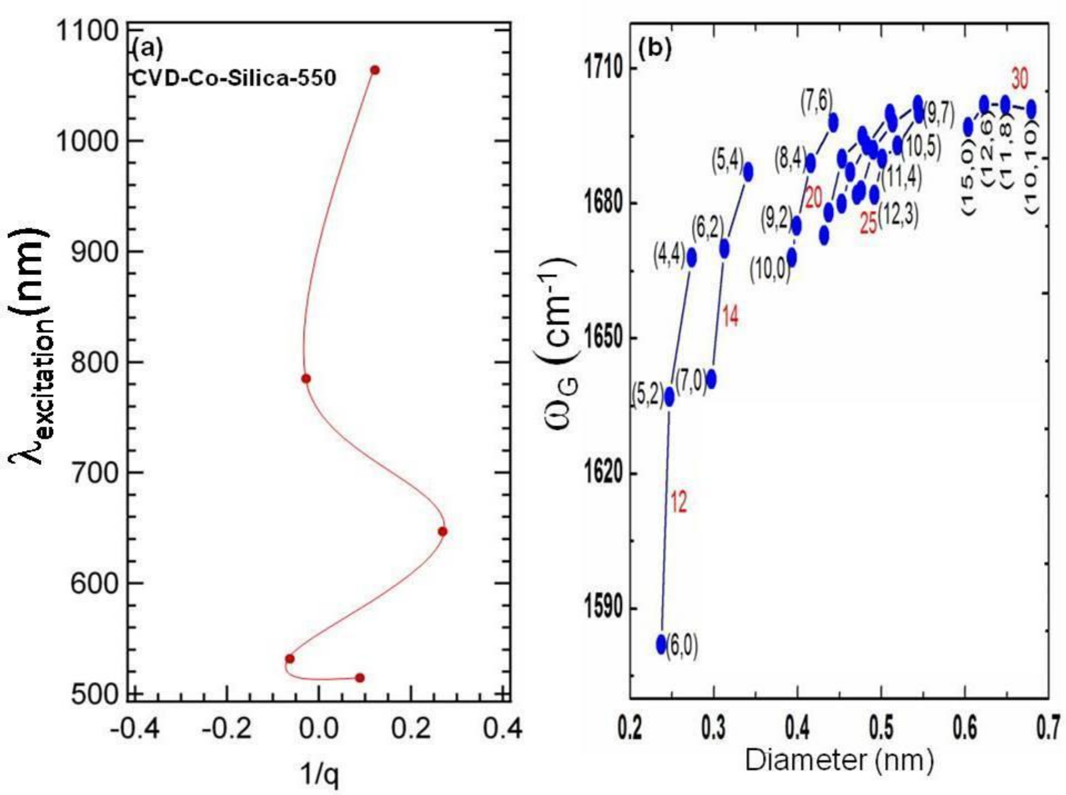

Figure 4.5.2: (a) Strength of el-ph interaction (*1/q* values) obtained from BWF fit (Eq. 4.4.1) to the G-band (Fig. 4.5.1c) show S-like dispersion. (b) Dispersion of G-band obtained from molecular dynamics simulation that employs a curvature-dependent force field exhibits *2n+ m* family lines.

Previously, shift in the G-band frequency (energy) due to high tube curvature has been explored by Sasaki *et al.* [103] using the second order perturbation theory (Eq. 4.5.1),

$$\hbar\omega_{\lambda}^{(2)} = 2\sum_{k}\frac{\left|\langle eh(k)\,|\,H_{\text{int}}\,|\,\omega_{\lambda}\rangle\right|^{2}}{\hbar\omega_{\lambda}^{(0)} - [E_e(k) - E_h(k)] + i\Gamma_{\lambda}} \times \left\{ f[E_h(k) - E_F] - f[E_e(k) - E_F] \right\} \quad (4.5.1).$$

In Eq. 4.5.1, $\hbar\omega_{\lambda}^{(2)}$ is the second order energy perturbation term, and $\langle eh(k)\,|\,H_{\text{int}}\,|\,\omega_{\lambda}\rangle$ is the matrix element for the creation of electron-hole pair at k by the el-ph interaction H_{int}

and λ ιs the polarization. Furthermore, Γ_{λ} is the decay width and the pre-factor 2 accounts for spin degeneracy in Eq. (4.5.1). In agreement with their diameter dependence of the TO and LO phonon frequencies [103], we concur that the hardening (or softening) of the optical phonon frequencies occurs due to nanotube curvature. Similar dispersions of the G-band have also been observed in other sub-nm SWNT samples used in this study (see Fig 4.4.4).

We further used molecular dynamics simulations on 30 different chiral and achiral tubes (Fig. 4.5.2b and 4.5.3a) with the well-known adaptive intermolecular reactive empirical bond order (AIREBO) potential [100], to confirm the dispersion of G-band due to high curvature. AIREBO is a reactive potential capable of treating variations in bond order and hybridization state. Although this semi-classical model contains no explicit treatment of electronic degrees of freedom, it does include the effects of SWNT curvature on bond order and force constants. It is worth noting that the interaction is included via an empirical approach to the analytical bond-order theory, which is equivalent to orthogonal tight-binding theory in the second-moments approximation [100]. Thus, SWNTs with small radii have reduced carbon-carbon bond angles which lead to decreased bond orders and more sp^3-like bonding character. Importantly, such molecular dynamics simulations allow the effects of dynamic variation in local curvature to be included in the simulated power spectra.

In Fig. 4.5.2b, we show the power spectra obtained via the Fourier transform of the velocity-velocity autocorrelation function,

$$C(\omega) = \int C_{vv}(t) e^{-i\omega t} dt \qquad \text{(4.5.2a),}$$

where,

$$C_{vv}(t) = \langle \mathbf{v}_i(t) \cdot \mathbf{v}_i(0) \rangle \qquad (4.5.2b)$$

.

After constructing the tubes with their equilibrium geometry using a tube generator, they were equilibrated at 300 K for 50 ps and then the $C_{vv}(t)$ was evaluated over 17 ps of microcanonical dynamics using a timestep of 0.1 fs. It is interesting to note that the dispersion of the G-band obtained from these simulations exhibits a $2n + m$ = constant family line behavior (Fig. 4.5.2b). As shown in Fig. 4.5.2b, the dispersion length of such family lines decreases as the value of $2n + m$ increases indicating that increase in the curvature can lead to a shift in the G-band as observed in Fig. 4.5.1c. In addition, as expected [95], the dispersion of the G-band is negligible for large diameter SWNTs (for $2n + m = 30$ as seen in Fig. 4.5.2b) and is maximum for sub-nm SWNTs ($2n + m = 12$ family). Previously, Jorio *et al*, showed that the G^+ feature is both diameter and chiral angle independent in case of SWNTs with $d > 1$ nm. However, the G^- features were found to be diameter dependent. As discussed above, in case of sub-nm SWNTs we observed that both these features exhibit dispersion with the incident laser energy due to high nanotube curvature (Fig. 4.5.1c).

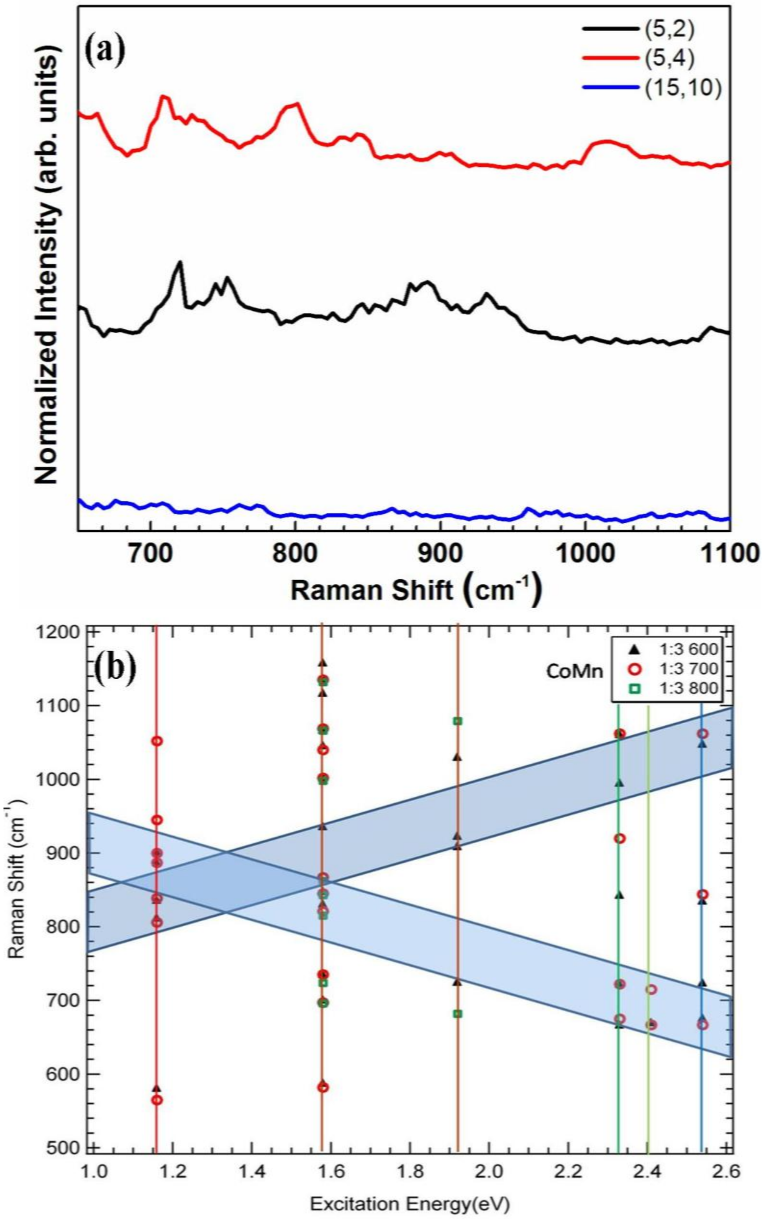

Figure 4.5.3: (a) Intermediate frequency modes obtained from the molecular dynamic simulations for different chiralities indicate that the IFMs are relatively weak at lower curvatures as in (15, 10) tube compared to (5, 2) or (5, 4) tubes. (b) IFMs observed at different excitations in sub-nm SWNTs samples synthesized using CoMn bimetallic

system at different temperatures. The shaded areas represent the regions where IFMs were previously reported [93-95].

Returning to Fig. 4.5.1b, we note that the IFMs of sub-nm SWNTs are as intense as the RBMs. Fantini *et al.* [93] suggested that the IFMs result from a simultaneous creation of an optical phonon and annihilation (or creation) of an acoustic phonon. Importantly, a step-like dispersion of the IFMs was observed for tube diameters in the range ~1-1.5 nm [3, 4]. Fantini and Alvarez *et al.* [93, 94] observed a linear dispersion of the IFMs with a positive (negative) slope when an acoustic phonon was created (annihilated) simultaneously with an optical phonon. Thus, in case of [93-97], a plot of IFM frequencies as a function of the laser energy exhibits a V-shape. The shaded areas in Fig. 3b represent this V-shape of the step-like dispersion for previously reported IFMs [93-96]. We find that in this study (i) several IFMs fall outside the proposed V shape area, and (ii) the intensity of the IFMs are enhanced only for certain $\lambda_{excitation}$. In particular, intense IFMs are observed with the 785 nm excitation from 0.61 nm sub-nm SWNTs (CVD-Co-Silica-550; ω_{RBM} ~ 374 cm^{-1}) which are not resonant with any other excitation wavelengths used in this study. In addition, as shown in Fig. (4.5.4), other excitations (for example the 1064 nm excitation) can also lead to the activation of a different set of IFMs in 0.81 nm sub-nm SWNTs.

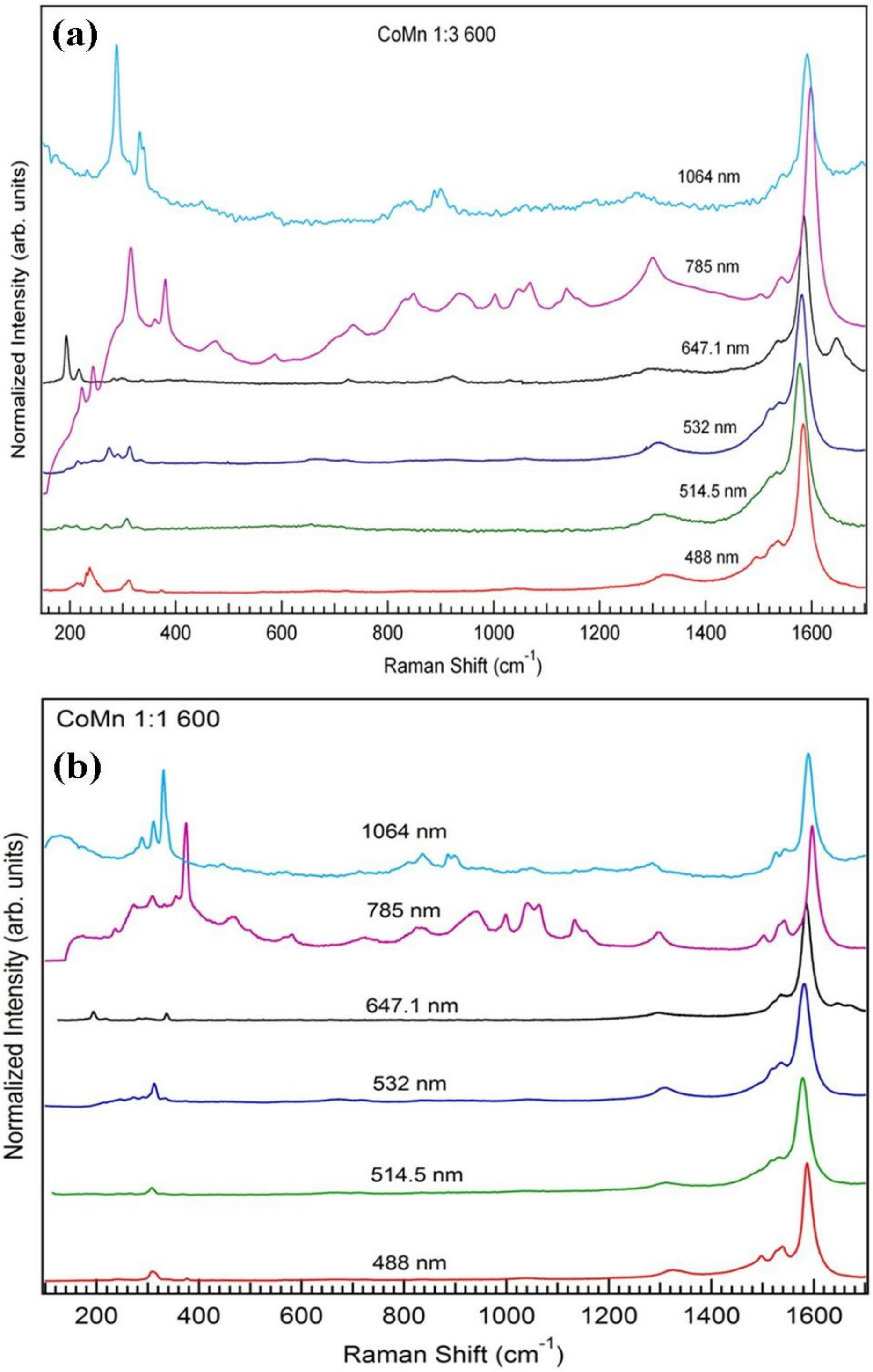

Figure 4.5.4: Raman spectra sub-nm SWNT samples grown using bi-metallic catalyst Co and Mn in (a) 1:3 and (b) 1:1 ratios at 600 °C. One can observe different sets of IFMs that are activated when different sub-nm SWNTs couple to 785 and 1064 nm excitations.

In agreement with the Raman spectra, our molecular dynamic simulations that include the effects of curvature in the force field also show an enhanced intensity for the IFM modes in SWNTs with higher curvature. For example, as shown in Fig. 4.5.3a, it is evident from the power spectrum of (15, 10) tubes that the IFMs are suppressed relative to those in (5, 2) and (5, 4) sub-nm SWNTs. These results indicate that the high curvature leads to activation of new phonon vibration in sub-nm SWNTs, which can also be inferred from the IR spectra discussed below. Previously, several reports have attributed activation of weak IFMs to symmetry lowering [107]. Based on our molecular dynamics simulations and resonant Raman spectra, we believe that the high curvature-induced strain in sub-nm SWNTs along with bending of nanotubes in the bundle can severely affect some of the symmetries such as the screw axis, mirror planes and hence lead to symmetry lowering [108].

Next, we focus our discussion on the RBMs in Fig. 4.5.1a. We find that the resonant behavior for most of the RBMs exhibited by the samples used in this study can be adequately described using a Kataura plot with γ_o=2.45 eV [109]. This value of γ_o is in agreement with the γ_o deduced from scanning tunneling spectroscopic (STS) studies on sub-nm SWNTs [110, 111]. For $\lambda_{excitation}$ = 785 nm, an intense RBM peak is present at 374 cm^{-1} (0.61 nm, Fig 4.5.1a). According to the original Kataura plot which uses γ_o = 2.75 eV, E_{11} for 0.61 nm diameter tubes is ~1.28 eV and will not bring the tubes into resonance with the 785 nm (1.58 eV) excitation. Other earlier reports on ultra-small SWNTs (d ~ 0.4 nm) synthesized in zeolite crystal have also shown such failure of zone folding approximation [112, 113], where the frequency of RBM mode varies inversely with the diameter [30]. It is also worth mentioning that Heinz and co-workers [114] have reported exciton binding energies of ~400 meV for *semiconducting* 0.8 nm diameter tubes, which could bring the 0.61 nm tubes into resonance.

Interestingly, independent of metallic or semiconducting nature of sub-SWNTs, we find that the resonance of 0.61 nm tubes with 785 nm excitation can be explained in terms of curvature dependent γ_0. Using π-electron tight binding model of SWNTs (π-TB) many authors [115, 116] showed that the effective overlap integral between two nearest-neighbor carbon atoms is sensitive to the tube curvature, and depends on the direction of the bond with respect to nanotube axis. As the curvature (κ) increases, the mixing between *s* and *p* orbitals becomes important, and therefore γ_0 can be Taylor expanded as a function of curvature around its value for graphite ($\gamma_0(0)$) as

$$\gamma_o\left(\kappa\right) = \gamma_0(0) + \left.\frac{d\gamma}{d\kappa}\right|_0 \kappa \qquad (4.5.3)$$

Furthermore, we also include the chiral angle (θ) dependent part of the E_{ii} to obtain an effective energy gap as in eqn. 4.5.4 [99]:

$$E^{eff}{}_{11} = \frac{2a_{cc}}{d}\left[\gamma_0 + \left.\frac{d\gamma}{d\kappa}\right|_0 \kappa\right]\left(1 + (-1)^{(n-2m)}\,\frac{a_{cc}\cos(3\theta)}{2.2d}\right) \qquad (4.5.4)$$

We deduced an empirical value of 0.28 eV-nm for $\left.\frac{d\gamma_0}{d\kappa}\right|_0$ using the values of γ_0 derived from previous STS measurements on individual SWNTs [110, 111] with different diameter distributions. As noted above, the excess energy required to bring the sub-nm

SWNTs into resonance can now be understood from Eq. 4.5.4. For example, we obtain an energy gap of E_{11} = 1.60 eV for a 0.61 nm tube and thus see a resonance enhancement of its RBM with a 785 nm (1.58 eV) laser excitation. Similarly using Eq. 4.5.4 we obtain a value of E_{22} = 2.44 eV in the case of a 0.95 nm tube (ω_{RBM} =247 cm^{-1}) and thus observe a resonant RBM with $\lambda_{excitation}$ =532 nm (2.33 eV). Thus, irrespective of the chirality of our sub-SWNTs, inclusion of curvature effects for γ_0 and E_{ii} (Eq. 4.5.4) account for the excess energy that is required to bring particular sub-nm SWNTs into resonance with specific excitations.

The conclusions drawn from the above Raman studies are also borne out from IR studies presented in Fig. 4.5.4. Group theory predicts three (2 E_{1u} and 1 A_{2u}) and six (5 E_{1u} and 1 A_{2u}) IR active modes for achiral and chiral SWNTs, respectively [117]. The lack of a static dipole moment makes it difficult to observe IR modes in SWNTs. Even in the presence of a dynamic dipole moment, only weak IR (high-frequency E_{1u} ~1590 cm^{-1} and A_{2u} ~ 860 cm^{-1}) activity has been reported in the electric arc and the laser ablated SWNTs [97, 98]. The IR spectra of purified SWNTs (d ~ 1.4±0.3 nm) prepared by the electric arc method (arc-SWNTs) are at least 4 times weaker compared to the CVD-Co-Silica-550 sub-nm SWNTs suggesting higher IR cross-section for sub-nm SWNTs (Fig. 4.5.4). In addition, the appearance of modes between 450-850 cm^{-1} in Fig. 4.5.4b (that are barely observed in both the arc-SWNTs and in the spectra reported in Ref. 7) vividly shows the effects of curvature-induced symmetry lowering in sub-nm SWNTs.

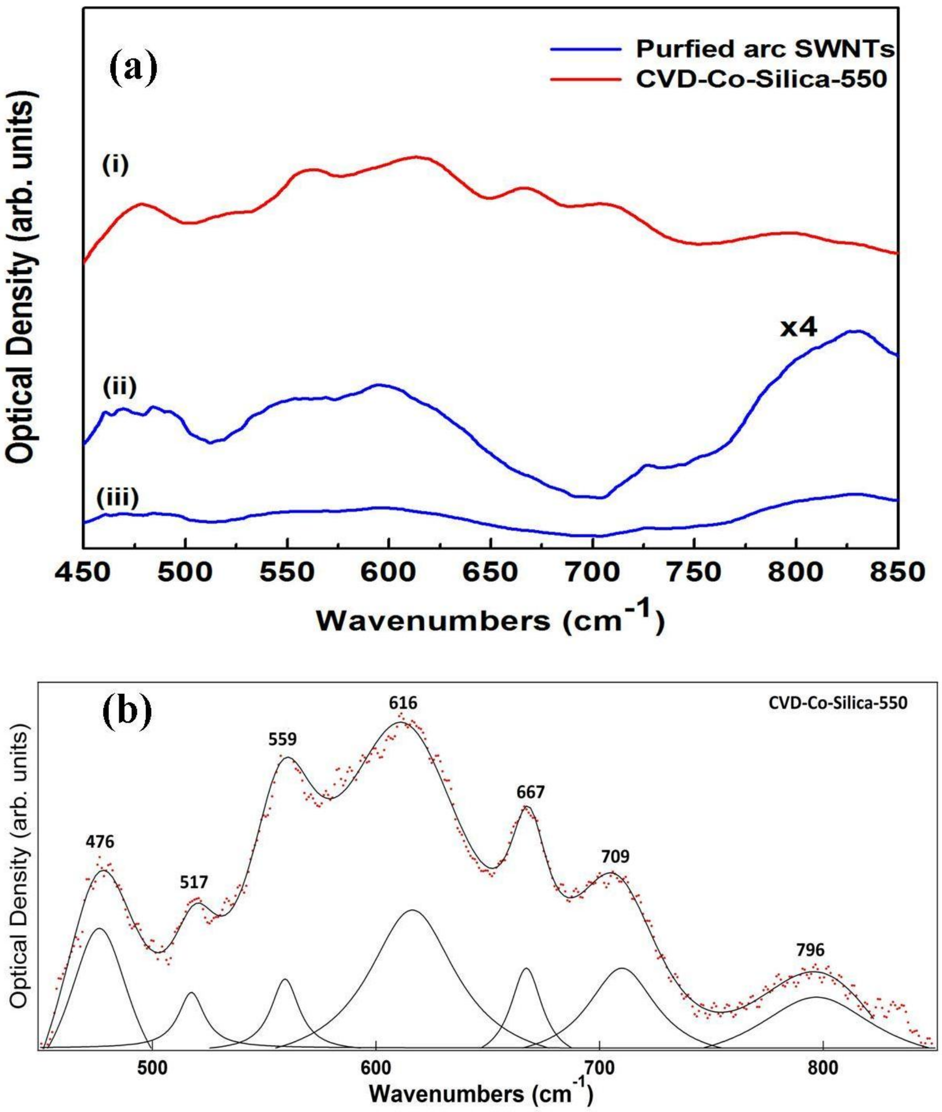

Figure 4.5.5: (a) IR spectra for CVD-Co-Silica-550 [(i)] and purified pristine SWNTs prepared by the electric arc method [(iii)]. The latter spectrum is shown on a magnified scale in [(ii)]. (b) The IR spectrum for CVD-Co-Silica-550 and its deconvolution.

In summary, For the G-band, we observe that the S-like dispersion with respect to E_{laser} in sub-nm SWNTs tracks the electron-phonon coupling strength (*1/q*), and our molecular dynamic simulations indicate that it consists of a family of lines with $2n + m$ = constant. In this context, we note that normalizing Raman spectra with respect to the intensity of the G-band (which is dispersionless in SWNTs with $d > 1$ nm) in sub-nm SWNTs is dependent on the tube diameter. Depending on the dominant sub-SWNT diameter present in the sample, the observed intermediate frequency modes resonantly couple to specific excitation energies. This resonance is understood in terms of curvature-induced effects in γ_0 (Eq. 4.5.4). Lastly, we show that the high curvarture lowers the symmetry of SWNTs and thus leads to the observation of relatively intense IR spectra.

Future Work

Understanding the nature of phonon decay and lifetimes in low-dimensional systems such as graphene and carbon nanotubes could have a big impact on their thermal conductance properties. Previously, anharmonicity was used to explain the phonon decay in carbon nanotubes. This led to the discovery of a phonon bottleneck mechanism, which explained the discrepancy in RBM lifetimes seen between the Raman spectroscopy and tunneling studies. Graphene nanoribbons will exhibit vHS in the energy density of states below the quantum confinement size. However, a periodic boundary condition (that leads to RBM in SWNTs) may not be applicable to such ribbons. Thus, the quantized momentum space of graphene nanoribbons may display different anharmonic decay than carbon nanotubes. A comparision of these bottlenecks between sp^2 and sp^x ($2<x<3$) hybridized systems can extend our understanding of low dimensional systems. In this work, we observed that the Fano interaction parameter changes as a function of L_a. Studying the change of *pi*-plasmon energy as a function of nanoribbon size can open doors for several new application such as coherent plasmon coupling etc.,.

Appendix

Glossary of acronyms used in this dissertation

BLG-Bi-layer graphene

BWF – Breit-Wigner-Fano

CVD- Chemical vapor deposition

DOS – Density of states

FLG-Few-layer graphene

FTIR – Fourier transform infrared

FWHM – Full-width half maximum

i-In-plane

IBLG-Incommensurate bilayer graphene

HRTEM – High resolution transmission electron microscope

LA – Longitudinal acoustic

LO- Longitudinal optical

NW- Nanowires

o- Out-of-plane

PA- Photon absorption

RBM – Radial breathing mode

SAED – Selected area electron diffraction

SEM – Scanning electron microscope

SLG-Single-layer graphene

STM – Scanning tunneling microscope

SWNT – Single-walled carbon nanotube

TA – Transverse acoustic

TO- Transverse optical

vHS – Van Hove singularities

References

1. C. H. Lui *et al.*, Imaging Stacking Order in Few-Layer Graphene. *Nano Letters* **11**, 164 (2011).
2. M. A. Pimenta *et al.*, Studying disorder in graphite-based systems by Raman spectroscopy. *Physical Chemistry Chemical Physics* **9**, 1276 (2007, 2007).
3. M. S. Dresselhaus, A. Jorio, A. G. Souza, R. Saito, Defect characterization in graphene and carbon nanotubes using Raman spectroscopy. *Philos. Trans. R. Soc. A-Math. Phys. Eng. Sci.* **368**, 5355 (Dec, 2010).
4. L. M. Malard, M. A. Pimenta, G. Dresselhaus, M. S. Dresselhaus, Raman spectroscopy in graphene. *Physics Reports-Review Section of Physics Letters* **473**, 51 (Apr, 2009).
5. C. Thomsen, Raman scattering in carbon nanotubes. *Proceedings of the SPIE - The International Society for Optical Engineering* **5219**, (17 Oct., 2003).
6. A. O. Barut, QUANTUM FIELD THEORY AND MANY-BODY PROBLEM. *Science* **147**, 1275 (1965, 1965).
7. S. Boffi, *QUANTUM FIELD THEORY AND MANY-BODY PROBLEM*. Nuovo Cimento (1965), vol. 36, pp. 306-&.
8. L. G. Cancado *et al.*, General equation for the determination of the crystallite size L-a of nanographite by Raman spectroscopy. *Appl. Phys. Lett.* **88**, (Apr, 2006).
9. A. C. Ferrari, Raman spectroscopy of graphene and graphite: Disorder, electron-phonon coupling, doping and nonadiabatic effects. *Solid State Communications* **143**, 47 (Jul, 2007).
10. S. Reich, C. Thomsen, Raman spectroscopy of graphite. *Philos. Trans. R. Soc. A-Math. Phys. Eng. Sci.* **362**, 2271 (Nov 15, 2004).
11. L. G. Cancado, M. A. Pimenta, B. R. A. Neves, M. S. S. Dantas, A. Jorio, Influence of the atomic structure on the Raman spectra of graphite edges. *Phys. Rev. Lett.* **93**, (Dec, 2004).
12. K. Vanheusden *et al.*, Mechanisms behind green photoluminescence in ZnO phosphor powders. *J. Appl. Phys.* **79**, 7983 (May 15, 1996).
13. T. Frank *et al.*, Energetically deep defect centers in vapor-phase grown zinc oxide. *Appl. Phys. A-Mater. Sci. Process.* **88**, 141 (Jul, 2007).
14. Y. W. Heo, D. P. Norton, S. J. Pearton, Origin of green luminescence in ZnO thin film grown by molecular-beam epitaxy. *J. Appl. Phys.* **98**, (Oct 1, 2005).
15. M. A. Reshchikov *et al.*, Luminescence properties of defects in ZnO. *Physica B* **401**, 358 (Dec, 2007).
16. L. S. Vlasenko, G. D. Watkins, Optical detection of electron paramagnetic resonance for intrinsic defects produced in ZnO by 2.5-MeV electron irradiation in situ at 4.2 K. *Phys. Rev. B* **72**, (Jul, 2005).
17. L. A. Kappers, O. R. Gilliam, S. M. Evans, L. E. Halliburton, N. C. Giles, EPR and optical study of oxygen and zinc vacancies in electron-irradiated ZnO. *Nuclear Instruments & Methods in Physics Research Section B-Beam Interactions with Materials and Atoms* **266**, 2953 (Jun, 2008).

18. S. M. Evans, N. C. Giles, L. E. Halliburton, L. A. Kappers, Further characterization of oxygen vacancies and zinc vacancies in electron-irradiated ZnO. *J. Appl. Phys.* **103**, (Feb 15, 2008).
19. M. D. McCluskey, S. J. Jokela, Defects in ZnO. *J. Appl. Phys.* **106**, (Oct 1, 2009).
20. G. A. Shi *et al.*, Hydrogen local modes and shallow donors in ZnO. *Phys. Rev. B* **72**, (Nov, 2005).
21. E. V. Lavrov, Hydrogen in ZnO. *Physica B* **404**, 5075 (Dec 15, 2009).
22. D. A. Long, Special Issue - Raman Spectroscopy of Proteins. *Journal of Raman Spectroscopy* **29**, 1 (Jan, 1998).
23. M. Sheik-Bahae, E. W. Van Stryland, Optical nonlinearities in the transparency region of bulk semiconductors. *Nonlinear Optics in Semiconductors I* **58**, 257 (1999, 1999).
24. E. W. Van Stryland, D. J. Hagan, in *Self-focusing: Past and Present*, R. W. L. S. G. S. Y. R. Boyd, Ed. (2009), vol. 114, pp. 573-591.
25. Y. R. Ryu *et al.*, Synthesis of p-type ZnO films. *J. Cryst. Growth* **216**, 330 (Jul, 2000).
26. S. R. Mishra *et al.*, Magnetic properties of mechanically milled nanosized cupric oxide. *J. Magn. Magn. Mater.* **279**, 111 (Aug, 2004).
27. J. Osorio-Guillen, S. Lany, S. V. Barabash, A. Zunger, Magnetism without magnetic ions: Percolation, exchange, and formation energies of magnetism-promoting intrinsic defects in CaO. *Phys. Rev. Lett.* **96**, (Mar, 2006).
28. A. Sundaresan, R. Bhargavi, N. Rangarajan, U. Siddesh, C. N. R. Rao, Ferromagnetism as a universal feature of nanoparticles of the otherwise nonmagnetic oxides. *Phys. Rev. B* **74**, (Oct, 2006).
29. Y. Belghazi, G. Schmerber, S. Colis, J. L. Rehspringer, A. Dinia, Extrinsic origin of ferromagnetism in ZnO and Zn0.9Co0.1O magnetic semiconductor films prepared by sol-gel technique. *Appl. Phys. Lett.* **89**, (Sep 18, 2006).
30. N. H. Hong, J. Sakai, V. Brize, Observation of ferromagnetism at room temperature in ZnO thin films. *J. Phys.-Condes. Matter* **19**, (Jan, 2007).
31. M. Gacic *et al.*, Magnetism of Co-doped ZnO thin films. *Phys. Rev. B* **75**, (May, 2007).
32. X. H. Wei *et al.*, Magnetism of TiO and TiO(2) nanoclusters. *J. Appl. Phys.* **105**, (Apr, 2009).
33. B. B. Straumal *et al.*, Magnetization study of nanograined pure and Mn-doped ZnO films: Formation of a ferromagnetic grain-boundary foam. *Phys. Rev. B* **79**, (May, 2009).
34. A. Sundaresan, C. N. R. Rao, Implications and consequences of ferromagnetism universally exhibited by inorganic nanoparticles. *Solid State Communications* **149**, 1197 (Aug, 2009).
35. M. Venkatesan, C. B. Fitzgerald, J. M. D. Coey, Unexpected magnetism in a dielectric oxide. *Nature* **430**, 630 (Aug 5, 2004).
36. K. R. Kittilstved, W. K. Liu, D. R. Gamelin, Electronic structure origins of polarity-dependent high-T-C ferromagnetismin oxide-diluted magnetic semiconductors. *Nature Materials* **5**, 291 (Apr, 2006).

37. U. Diebold, Structure and properties of TiO2 surfaces: a brief review. *Appl. Phys. A-Mater. Sci. Process.* **76**, 681 (Mar, 2003).
38. U. Ozgur *et al.*, A comprehensive review of ZnO materials and devices. *J. Appl. Phys.* **98**, (Aug 15, 2005).
39. S. Tanemura *et al.*, Synthesis, optical properties and functional applications of ZnO nano-materials: a review. *2008 2nd IEEE International Nanoelectronics Conference (NEC)*, (2008, 2008).
40. L. Schmidt-Mende, J. L. MacManus-Driscoll, ZnO - nanostructures, defects, and devices. *Materials Today* **10**, 40 (May, 2007).
41. Z. L. Wang, Zinc oxide nanostructures: growth, properties and applications. *J. Phys.-Condes. Matter* **16**, R829 (Jun 30, 2004).
42. S. Bandow *et al.*, Purification of single-wall carbon nanotubes by microfiltration. *Journal of Physical Chemistry B* **101**, 8839 (Oct, 1997).
43. S. Barth, F. Hernandez-Ramirez, J. D. Holmes, A. Romano-Rodriguez, Synthesis and applications of one-dimensional semiconductors. *Progress in Materials Science* **55**, 563 (Aug, 2010).
44. K. H. Tam *et al.*, Defects in ZnO nanorods prepared by a hydrothermal method. *Journal of Physical Chemistry B* **110**, 20865 (Oct 26, 2006).
45. Z. Y. Fan *et al.*, Photoluminescence and polarized photodetection of single ZnO nanowires. *Appl. Phys. Lett.* **85**, 6128 (Dec 20, 2004).
46. H. J. Lee, E. Helgren, F. Hellman, Gate-controlled magnetic properties of the magnetic semiconductor (Zn,Co)O. *Appl. Phys. Lett.* **94**, (May 25, 2009).
47. J. M. E. Harper, K. P. Rodbell, Microstructure control in semiconductor metallization. *Journal of Vacuum Science & Technology B* **15**, 763 (Jul-Aug, 1997).
48. B. J. Thompson, *Characterization techniques and tabulations for organic nonlinear optical materials - From the series editor*. M. G. D. C. W. Kuzyk, Ed., Characterization Techniques and Tabulations for Organic Nonlinear Optical Materials (1998), vol. 60, pp. III-IV.
49. Sutherland R. L, *Handbook of Nonlinear Optics*. S. R. L, Ed., (Dekker, Newyork, ed. 1) 1996.
50. E. B. Barros *et al.*, Raman spectroscopy of graphitic foams. *Phys. Rev. B* **71**, (Apr, 2005).
51. L. G. Cancado *et al.*, Anisotropy of the Raman spectra of nanographite ribbons. *Phys. Rev. Lett.* **93**, (Jul 23, 2004).
52. M. S. Dresselhaus, G. Dresselhaus, R. Saito, A. Jorio, Raman spectroscopy of carbon nanotubes. *Physics Reports-Review Section of Physics Letters* **409**, 47 (Mar, 2005).
53. M. S. Dresselhaus, P. C. Eklund, Phonons in carbon nanotubes. *Advances in Physics* **49**, 705 (Sep, 2000).
54. M. S. Dresselhaus, A. Jorio, M. Hofmann, G. Dresselhaus, R. Saito, Perspectives on Carbon Nanotubes and Graphene Raman Spectroscopy. *Nano Letters* **10**, 751 (Mar, 2010).
55. A. C. Ferrari, J. Robertson, Raman spectroscopy of amorphous, nanostructured, diamond-like carbon, and nanodiamond. *Philos. Trans. R. Soc. A-Math. Phys. Eng. Sci.* **362**, 2477 (Nov 15, 2004).

56. J. Klett, R. Hardy, E. Romine, C. Walls, T. Burchell, High-thermal-conductivity, mesophase-pitch-derived carbon foams: effect of precursor on structure and properties. *Carbon* **38**, 953 (2000, 2000).
57. M. W. Cole *et al.*, Structural, electronic, optical and vibrational properties of nanoscale carbons and nanowires: a colloquial review. *J. Phys.-Condes. Matter* **22**, (Aug, 2010).
58. K. S. Novoselov *et al.*, Two-dimensional atomic crystals. *Proceedings of the National Academy of Sciences of the United States of America* **102**, 10451 (Jul 26, 2005).
59. A. K. Geim, Graphene: Status and Prospects. *Science* **324**, 1530 (Jun 19, 2009).
60. A. K. Geim, K. S. Novoselov, The rise of graphene. *Nature Materials* **6**, 183 (Mar, 2007).
61. K. S. Novoselov *et al.*, Two-dimensional gas of massless Dirac fermions in graphene. *Nature* **438**, 197 (Nov 10, 2005).
62. Y. Zhang *et al.*, Direct observation of a widely tunable bandgap in bilayer graphene. *Nature* **459**, 820 (Jun 11, 2009).
63. S. Latil, V. Meunier, L. Henrard, Massless fermions in multilayer graphitic systems with misoriented layers: Ab initio calculations and experimental fingerprints. *Phys. Rev. B* **76**, (Nov, 2007).
64. Z. Ni, Y. Wang, T. Yu, Y. You, Z. Shen, Reduction of Fermi velocity in folded graphene observed by resonance Raman spectroscopy. *Phys. Rev. B* **77**, (Jun, 2008).
65. A. C. Ferrari *et al.*, Raman spectrum of graphene and graphene layers. *Phys. Rev. Lett.* **97**, (Nov 3, 2006).
66. R. Saito *et al.*, Probing phonon dispersion relations of graphite by double resonance Raman scattering. *Phys. Rev. Lett.* **88**, (Jan 14, 2002).
67. C. Casiraghi, S. Pisana, K. S. Novoselov, A. K. Geim, A. C. Ferrari, Raman fingerprint of charged impurities in graphene. *Appl. Phys. Lett.* **91**, (Dec 3, 2007).
68. A. Gupta, G. Chen, P. Joshi, S. Tadigadapa, P. C. Eklund, Raman scattering from high-frequency phonons in supported n-graphene layer films. *Nano Letters* **6**, 2667 (Dec 13, 2006).
69. L. G. Cancado, A. Reina, J. Kong, M. S. Dresselhaus, Geometrical approach for the study of G ' band in the Raman spectrum of monolayer graphene, bilayer graphene, and bulk graphite. *Phys. Rev. B* **77**, (Jun, 2008).
70. C. N. R. Rao, K. S. Subrahmanyam, H. S. S. R. Matte, A. Govindaraj, GRAPHENE: SYNTHESIS, FUNCTIONALIZATION AND PROPERTIES. *Modern Physics Letters B* **25**, 427 (Mar 20, 2011).
71. A. K. Gupta, Y. Tang, V. H. Crespi, P. C. Eklund, Nondispersive Raman D band activated by well-ordered interlayer interactions in rotationally stacked bilayer graphene. *Phys. Rev. B* **82**, (Dec 15, 2010).
72. P. Poncharal, A. Ayari, T. Michel, J. L. Sauvajol, Raman spectra of misoriented bilayer graphene. *Phys. Rev. B* **78**, (Sep, 2008).
73. R. Rao *et al.*, Effects of Layer Stacking on the Combination Raman Modes in Graphene. *Acs Nano* **5**, 1594 (Mar, 2011).
74. P. H. Tan, S. Dimovski, Y. Gogotsi, Raman scattering of non-planar graphite: arched edges, polyhedral crystals, whiskers and cones. *Philosophical*

Transactions of the Royal Society of London Series a-Mathematical Physical and Engineering Sciences **362**, 2289 (Nov 15, 2004).

75. V. W. Brar *et al.*, Second-order harmonic and combination modes in graphite, single-wall carbon nanotube bundles, and isolated single-wall carbon nanotubes. *Phys. Rev. B* **66**, (Oct 15, 2002).
76. A. V. Ellis, Second-order overtone and combination modes in the LOLA region of acid treated double-walled carbon nanotubes. *Journal of Chemical Physics* **125**, (Sep 28, 2006).
77. R. Rao *et al.*, Double resonance Raman study of disorder in CVD-grown single-walled carbon nanotubes. *Carbon* **49**, 1318 (Apr, 2011).
78. P. H. Tan *et al.*, Resonantly enhanced Raman scattering and high-order Raman spectra of single-walled carbon nanotubes. *Appl. Phys. Lett.* **75**, 1524 (Sep 13, 1999).
79. A. M. Rao *et al.*, Effect of van der Waals interactions on the Raman modes in single walled carbon nanotubes. *Phys. Rev. Lett.* **86**, 3895 (Apr 23, 2001).
80. C. Fantini, M. A. Pimenta, M. S. Strano, Two-phonon combination Raman modes in covalently functionalized single-wall carbon nanotubes. *Journal of Physical Chemistry C* **112**, 13150 (Aug 28, 2008).
81. J.-W. Jiang, H. Tang, B.-S. Wang, Z.-B. Su, Raman and infrared properties and layer dependence of the phonon dispersions in multilayered graphene. *Phys. Rev. B* **77**, (Jun, 2008).
82. R. Saito, Dispersive Raman spectra observed in graphite and single wall carbon nanotubes. *Physica B* **323**, 100 (Oct, 2002).
83. D. S. Knight, W. B. White, CHARACTERIZATION OF DIAMOND FILMS BY RAMAN-SPECTROSCOPY. *Journal of Materials Research* **4**, 385 (Mar-Apr, 1989).
84. H. Hashimoto *et al.*, Crystallite size dependence of plasmon energies in polycrystalline graphite observed by reflected electron energy loss spectroscopy. *Japanese Journal of Applied Physics Part 1-Regular Papers Short Notes & Review Papers* **38**, 4136 (Jul, 1999).
85. V. Y. Osipov *et al.*, Raman characterization and UV optical absorption studies of surface plasmon resonance in multishell nanographite. *Diamond and Related Materials* **20**, 205 (Feb, 2011).
86. J. M. Dawlaty, S. Shivaraman, M. Chandrashekhar, F. Rana, M. G. Spencer, Measurement of ultrafast carrier dynamics in epitaxial graphene. *Appl. Phys. Lett.* **92**, (Jan 28, 2008).
87. J. S. Park *et al.*, G ' band Raman spectra of single, double and triple layer graphene. *Carbon* **47**, 1303 (Apr, 2009).
88. P. Y. Huang *et al.*, Grains and grain boundaries in single-layer graphene atomic patchwork quilts. *Nature* **469**, 389 (Jan 20, 2011).
89. Q. Yu *et al.*, Control and characterization of individual grains and grain boundaries in graphene grown by chemical vapour deposition. *Nature Materials* **10**, 443 (Jun, 2011).
90. K. F. Mak, J. Shan, T. F. Heinz, Seeing Many-Body Effects in Single- and Few-Layer Graphene: Observation of Two-Dimensional Saddle-Point Excitons. *Phys. Rev. Lett.* **106**, (Jan 25, 2011).

91. D.-H. Chae *et al.*, Excitonic Fano Resonance in Free-Standing Graphene. *Nano Letters* **11**, 1379 (Mar, 2011).
92. G. Xing, H. Guo, X. Zhang, T. C. Sum, C. H. A. Huan, The Physics of ultrafast saturable absorption in graphene. *Optics Express* **18**, 4564 (Mar 1, 2010).
93. C. Fantini *et al.*, Steplike dispersion of the intermediate-frequency Raman modes in semiconducting and metallic carbon nanotubes. *Phys. Rev. B* **72**, (Aug, 2005).
94. L. Alvarez, A. Righi, S. Rols, E. Anglaret, J. L. Sauvajol, Excitation energy dependence of the Raman spectrum of single-walled carbon nanotubes. *Chemical Physics Letters* **320**, 441 (Apr 14, 2000).
95. A. M. Rao *et al.*, Diameter-selective Raman scattering from vibrational modes in carbon nanotubes. *Science* **275**, 187 (Jan 10, 1997).
96. G. Chen *et al.*, Raman-active modes of single-walled carbon nanotubes derived from the gas-phase decomposition of CO (HiPco process). *Journal of Nanoscience and Nanotechnology* **2**, 621 (Dec, 2002).
97. U. J. Kim *et al.*, Infrared-active vibrational modes of single-walled carbon nanotubes. *Phys. Rev. Lett.* **95**, (Oct 7, 2005).
98. J. L. Bantignies, J. L. Sauvajol, A. Rahmani, E. Flahaut, Infrared-active phonons in carbon nanotubes. *Phys. Rev. B* **74**, (Nov, 2006).
99. H. Yorikawa, S. Muramatsu, ENERGY GAPS OF SEMICONDUCTING NANOTUBULES. *Phys. Rev. B* **52**, 2723 (Jul 15, 1995).
100. S. J. Stuart, A. B. Tutein, J. A. Harrison, A reactive potential for hydrocarbons with intermolecular interactions. *Journal of Chemical Physics* **112**, 6472 (Apr 8, 2000).
101. N. Li, X. Wang, F. Ren, G. L. Haller, L. D. Pfefferle, Diameter Tuning of Single-Walled Carbon Nanotubes with Reaction Temperature Using a Co Monometallic Catalyst. *Journal of Physical Chemistry C* **113**, 10070 (Jun 11, 2009).
102. C. Z. Loebick *et al.*, Effect of Manganese Addition to the Co-MCM-41 Catalyst in the Selective Synthesis of Single Wall Carbon Nanotubes. *Journal of Physical Chemistry C* **113**, 21611 (Dec 31, 2009).
103. K.-i. Sasaki *et al.*, Curvature-induced optical phonon frequency shift in metallic carbon nanotubes. *Phys. Rev. B* **77**, (Jun, 2008).
104. A. M. Rao, P. C. Eklund, S. Bandow, A. Thess, R. E. Smalley, Evidence for charge transfer in doped carbon nanotube bundles from Raman scattering. *Nature* **388**, 257 (Jul 17, 1997).
105. S. D. M. Brown *et al.*, Origin of the Breit-Wigner-Fano lineshape of the tangential G-band feature of metallic carbon nanotubes. *Phys. Rev. B* **63**, (Apr 15, 2001).
106. Y. K. Kwon, S. Saito, D. Tomanek, Effect of intertube coupling on the electronic structure of carbon nanotube ropes. *Phys. Rev. B* **58**, 13314 (Nov 15, 1998).
107. R. Saito, T. Takeya, T. Kimura, G. Dresselhaus, M. S. Dresselhaus, Raman intensity of single-wall carbon nanotubes. *Phys. Rev. B* **57**, 4145 (Feb 15, 1998).
108. J. W. Ding *et al.*, Curvature and strain effects on electronic properties of single-wall carbon nanotubes. *J. Phys.-Condes. Matter* **15**, L439 (Jul 16, 2003).
109. H. Kataura *et al.*, Optical properties of single-wall carbon nanotubes. *Synthetic Metals* **103**, 2555 (Jun, 1999).
110. T. W. Odom, J. L. Huang, P. Kim, C. M. Lieber, Atomic structure and electronic properties of single-walled carbon nanotubes. *Nature* **391**, 62 (Jan 1, 1998).

111. J. W. G. Wildoer, L. C. Venema, A. G. Rinzler, R. E. Smalley, C. Dekker, Electronic structure of atomically resolved carbon nanotubes. *Nature* **391**, 59 (Jan 1, 1998).
112. J. Kurti, G. Kresse, H. Kuzmany, First-principles calculations of the radial breathing mode of single-wall carbon nanotubes. *Phys. Rev. B* **58**, R8869 (Oct 1, 1998).
113. Z. K. Tang *et al.*, Novel properties of 0.4 nm single-walled carbon nanotubes templated in the channels of AlPO4-5 single crystals. *New Journal of Physics* **5**, (Oct 27, 2003).
114. F. Wang, G. Dukovic, L. E. Brus, T. F. Heinz, The optical resonances in carbon nanotubes arise from excitons. *Science* **308**, 838 (May 6, 2005).
115. P. Lambin, V. Meunier, Structural and electronic properties of carbon nanotube junctions. *Carbon Filaments and Nanotubes: Common Origins, Differing Applications? Proceedings of the NATO Advanced Study Institute,* (2001, 2001).
116. A. Kleiner, S. Eggert, Curvature, hybridization, and STM images of carbon nanotubes. *Phys. Rev. B* **64**, (Sep 15, 2001).
117. J. Zhou, J. Dong, Infrared properties of single-walled carbon nanotubes calculated from first principles. *J. Appl. Phys.* **107**, (Jan 15, 2010).